University of Cincinnati

Date: 4/21/2020

I, Dong Han, hereby submit this original work as part of the requirements for the degree of Doctor of Philosophy in Engineering Mechanics.

It is entitled:

On Eulerian-Lagrangian-Lagrangian Method for Solving Fluid-Structure Interaction Problem

Student's name: **Dong Han**

This work and its defense approved by:

Committee chair: Gui-Rong Liu, Ph.D.

Committee member: Shaaban Abdallah, Ph.D.

Committee member: Prashant Khare, Ph.D.

UNIVERSITY OF Cincinnati

36867

On Eulerian-Lagrangian-Lagrangian Method for Solving Fluid-Structure Interaction Problem

A dissertation submitted to the
Graduate School
of the University of Cincinnati
in partial fulfillment of the
requirements for the degree of

DOCTORATE OF PHILOSOPHY

in the Department of Aerospace Engineering and Engineering Mechanics
of the College of Engineering and Applied Science

by

Dong Han

M.S. Nanjing University of Aeronautics and Astronautics
April 2013

Committee Chair: Gui-Rong Liu, Ph.D.

ABSTRACT

This dissertation proposed an Eulerian-Lagrangian-Lagrangian (ELL) method for solving fluid-structure interaction (FSI) problems with an improved solution. The structures in ELL can be rigid or flexible, static or moving. The ELL method improves the accuracy of the solution in comparison with the regular immersed finite element method (IFEM) with bulk solid. The ELL for the thin structure is validated by solving, when conventional IFEM fails, two-dimensional (2D) and three-dimensional (3D) FSI problems with both rigid and flexible thin solid structures. The studies of mesh refinement, spatial convergence, and influence of the Lagrangian fluid domain are conducted in 2D and 3D cases with rigid structures. In the 2D flexible numerical examples, the continuum based beam (CB beam) element is adopted to model the thin structure. In the 3D flexible cases, the degenerated continuum-based shell (CB shell) element is employed.

This dissertation is dedicated

to my father

– to whom I miss every day

after he left this world

ACKNOWLEDGEMENTS

Firstly, I would like to express my deepest gratitude to my advisor Prof. G.R. Liu for the continuous support of my graduate education and related research, for his patience, motivation, and immense knowledge. His guidance helped me getting through the time of my Ph.D. research and writing of this thesis in the University of Cincinnati.

Besides my advisor, I would like to thank the rest of my thesis committee: Prof. Shaaban Abdallah, and Prof. Prashant Khare, for their insightful comments and encouragement, but also for the discussions and questions which improved my thesis from various perspectives.

My appreciation also extends to Dr. Hua Hu in Procter & Gamble who provided me an opportunity to work with him in the UC Simulation Center, and funded me for the last year of my Ph.D. study.

I would like to thank all my labmates, Guangyu Wang, Yixin Lin, Tao Lin, Zirui Mao, Zimo Zhu, Qinan Li, Parikshit Boregowda, Mitra Lanka, Sauradeep Bhowmick and Balachander Gnanasekaran, for the stimulating discussions, and for all the fun we have had in the last five years.

Last but not the least, I would like to thank my parents, Xinguo Han and Yafeng Li, for their supporting me throughout my life. I am indebted to them.

TABLE OF CONTENTS

LIST OF TABLES

LIST OF FIGURES

LIST OF SYMBOLS AND ABBREVIATIONS

v	Velocity
u	Displacement
a	Acceleration
g	Gravity
$\boldsymbol{x}$	Spatial position
$\boldsymbol{X}$	Material position
i, j, k	Index of dimession
I, J, K	Nodal index of element
N	Shape function
t, T, τ	Time
ρ	Density
E	Young's modulus
ν	Passion's ratio
σ	Cauchy stress
Ω	Domain
Γ	The surface of a domain
m	Mass
p	Pressure
$f^{FSI,*}$	FSI force
ω	Angular velocity
θ	Angular displacement
μ	Dynamic viscosity

Δh	Element size
f	Vibration frequency
St	Strouhal number
Re	Reynolds number
Fr	Froude number

CHAPTER 1. INTRODUCTION

The fluid-structure interaction (FSI) problem, which depicts moving or deformable solids/structures interacting with an internal or surrounding fluid flow, is becoming one of the hottest topics in the scientific and engineering field in recent years. In an FSI problem, the movement of the immersed solid causes the change of the fluid's pressure and velocity fields; in return, the pressure distribution of the fluid forces the solid to move and deform [1, 2]. Such problems have gained substantial interests, and many studies have been investigated in the literature. For instance, insect/bird wings, fish fins, falling seeds and leaves, human heart valves and vocal folds, and blood flow [3-15]. The interaction effects between fluids and structures have instinct complexities that make it still significant challenges, both theoretically and empirically.

Though the theories for solid and fluid mechanics have been developed individually for hundreds of years, the comprehensive and systematic understanding of the FSI phenomena remains a challenge due to its strong nonlinearity and multidisciplinary nature. It is impossible, in general, to approach analytical solutions for most of the FSI problems. The experiments, on the other hand, are limited in scope due to their expensive setups and difficulties in measurement. For example, the measuring equipment might disturb the flow, or the flow may be inaccessible [16]. The numerical/computational method to model and analyze the FSI problems thus offers a compelling alternative and seems promising in the future.

The computational mechanics, especially after the massive adoption of the supercomputer, renders a powerful tool to help both mathematicians and engineers for a

better understanding of the fundamental mechanism of the FSI problems. In the past decades, computational methods have been widely used to solve various types of FSI problems. Accuracy and efficiency are the most important aspects to be considered in these algorithms, but usually, they are not both achievable. Hence, the long-term research goal of computational methods is to develop a more sophisticated algorithm that makes these two aspects compatible. Then an FSI simulation could be cheap and easy to achieve in the analysis, which would be beneficial to a wide range of engineering applications.

1.1 FSI algorithms review

The numerical method in solving the FSI problem can be dated back to the late 1970s, and numerous approaches have been proposed since then. Based on the treatment of meshes, these FSI computational methods can be broadly classified into two categories: the *conforming meshes methods* and the *non-conforming meshes methods* [17, 18]. The conforming meshes methods are also known as body-fitted methods or body-conforming methods; the non-conforming meshes methods are called non-conforming body methods. The distinction between the two methods is indeed the different treatments of the FSI interface, as shown in Figure 1.1. The conforming meshes methods always have the meshes that conform to the interface. This type of approach, such as the arbitrary Lagrangian-Eulerian (ALE) method [19-22] and space-time (ST) method [23-25], requires moving mesh techniques to track the sharp FSI interface. The re-meshing process can be time-consuming and computationally expensive.

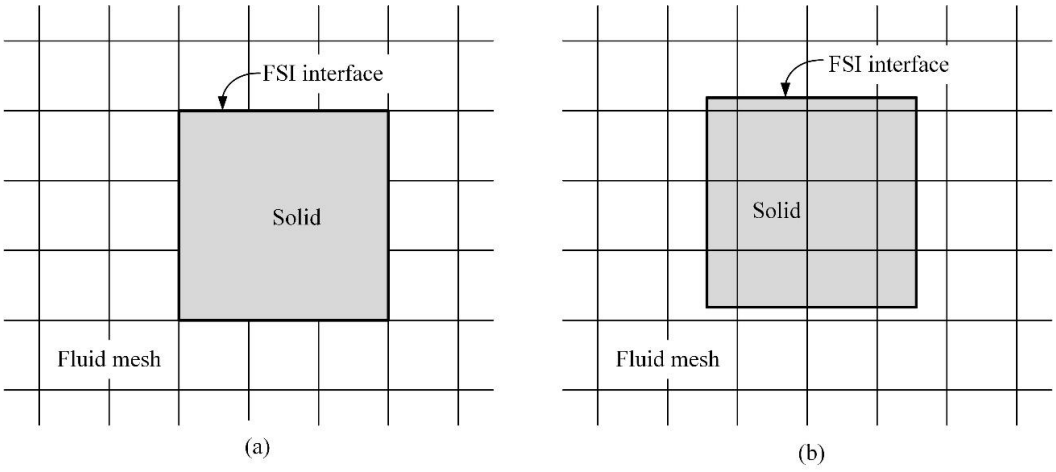

Figure 1.1: The conceptual illustration of the distinction between two types of FSI methods: (a) the conforming mesh method and (b) the nonconforming mesh method.

On the other hand, in the nonconforming techniques, the interface conditions are treated as constraints imposed between solid and fluid, therefore, avoiding re-meshing during computation. The immersed type method, such as immersed boundary method (IBM) [26, 27] and immersed finite element method (IFEM) [28], is among the most popular nonconforming mesh methods. The immersed type method uses a fixed Eulerian fluid domain, thus avoid re-meshing. Fluid and solid meshes can be generated independently.

Another classification groups the FSI algorithms, based on the solving procedure, into two categories: the *monolithic approach* and the *partitioned approach* [29-35]. In the monolithic approach, the fluid and solid are treated in the same mathematical framework, thus making the entire FSI problem a single system of governing equations that can be solved simultaneously by a unified algorithm. The advantage of the monolithic approach is the seamless coupling of the FSI interface and mathematical simplicity of the modeling, which can approach a more accurate and physically realistic solution. However, the

disadvantages of the monolithic approach usually require more substantially computational resources and expertise to develop and maintain the code.

The partitioned approach detaches the fluid and solid domain, and then separated solvers are applied. The approaching scheme of the partitioned procedure is more flexible and efficient, makes it the most heavily used method in real engineering applications. Nevertheless, the accuracy and stability of the solution might deteriorate due to the errors in the FSI coupling. This challenge arises from having an accurate and efficient FSI solution to coordinate the disciplinary algorithms. The automatically tracking of the interface can be cumbersome and easily error-prone.

1.2 The immersed boundary method

The immersed boundary method (IBM) is perhaps the most popular FSI method that is the non-conforming meshes method and partitioned approach. IBM was first proposed by Peskin in the 1970s to study the blood flow patterns around heart valves [36, 37]. The most significant advantage of IBM is the structure meshes move on the top of the fixed fluid grids. Therefore, the Eulerian described fluid, and the solid of the Lagrangian described solid are solved separately. No re-meshing is needed. FSI force is first evaluated in the assumed fiber-like dimensionless structure, then transferred to the nearby fluid grids through a discretized Dirac delta function; the nodal velocity of the structure is summed from neighboring fluid grids by a reversed process, as illustrated in Figure 1.2 (a). The employment of such discretized Dirac delta function usually requires a uniform meshing scheme of fluid, thus limits the functionality of IBM when dealing with the complex

geometry of the fluid domain. The fiber-like framework of the solid, in IBM, also prevents it from adopting a wide range of physically-based solid modeling.

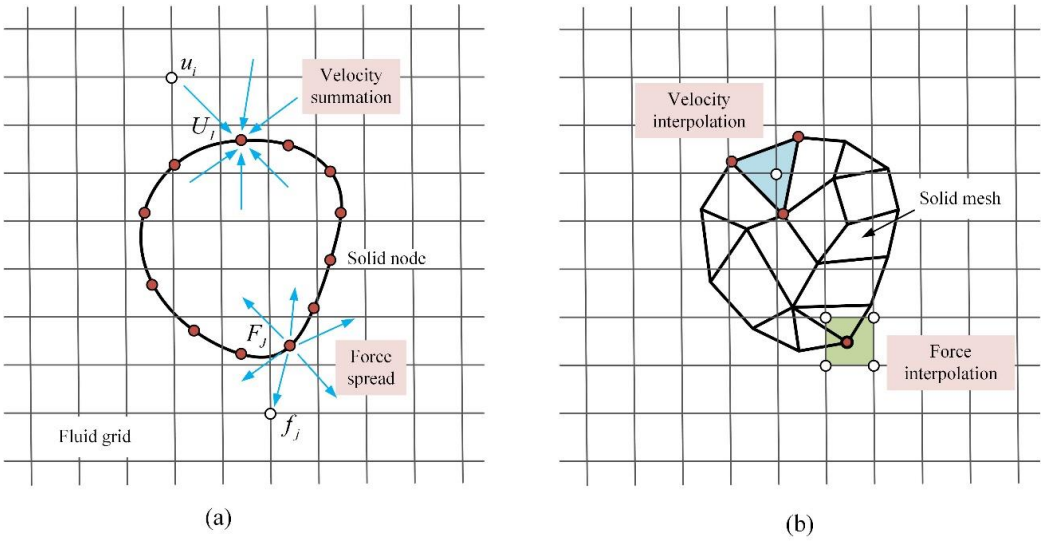

Figure 1.2: Conceptual schemes of (a) IBM and (b) IFEM

Despite its inaccuracy, the automatic tracking of the FSI interface, in IBM, circumvents the cumbersome re-meshing or adaptive mesh process in the conforming meshes methods. This most significant advantage makes it an efficient approach in analyzing complicated FSI problems. Many researchers have made efforts to enhance its accuracy and efficiency further [38-44]. For example, LeVeque and Li proposed the immersed interface method in [45]. Instead of using the Dirac delta function, a second-order solution for Stokes fluid at the FSI interface based on the finite difference method (FDM) with uniform grids is imposed to have a second-order accuracy in Peskin's IBM. The sharp-interface IBM proposed by Mitta et al. [46] employs the ghost-cell technique to precisely satisfy the boundary conditions in IBM. It can also handle complex FSI problems with unstructured fluid grids. Based on the fictitious domain methods, Glowinski et al. [47-50] developed the distributed Lagrange multiplier (DLM) methods for simulation of a large

number of rigid particles in the fluid. Turek et al. [51-54] proposed the multigrid fictitious boundary method (FBM) and combined it with the deformable background meshes, which improves the solution accuracy with small computational effort. In these methods, the finite element meshes (FEM) are available for the background Eulerian fluid domain.

Inspired by the fictitious domain method, the immersed domain method (IDM), such as the immersed finite element method (IFEM) [55-59], the immersed smoothed finite element method (IS-FEM) [60-63], and the immersed continuum method [64-66], was proposed to extend IBM for solving FSI problems with bulk solids. Like other immersed type methods, IDM has fixed background fluid grids by introducing a fictitious fluid domain to compensate for the area occupied by the solid. The Lagrangian described solid, and Eulerian described fluid domains are constructed independently, thus allowing the solid and fluid to be solved separately. The solid body with a finite volume is modeled using more realistic material constitutive laws. Also, the reproducing kernel particles method (RKPM) replaces the Dirac delta function in conventional IBM. Moreover, non-uniform Eulerian fluid meshes can be adopted for the fluid solver.

The critical issue of the immersed type method is to have a smooth function, such as Dirac delta function in the IBM or RKPM in the IFEM, to interpolate the FSI conditions from one domain to another near the interface. However, the accuracy of the solution largely depends on the quality of the grid. A high-resolution meshing scheme is usually required to guarantee good results, which leads to expensive computations. For the coarser grids, the interpolated solution near the interface would be smeared and typically thicken the fluid-structure interface. To alleviate this issue, Wang et al. used the direct finite element method (FEM) interpolation to track the FSI interface implicitly [67]. Such

interpolation is also more physically realistic and only requires one element layer instead of several smearing grids, as illustrated in Figure 1.2 (b).

1.3 Finite Element Method

The finite element method (FEM) has become an essential and vital tool for solving partial differential equations (PDEs) since the late 1950s [68, 69]. The fundamental idea of FEM is to address the PDFs in a continuous domain into a finite number of small discretized domains. These small domains are known as “elements”, and Clough named it with the terminology finite element method [70, 71]. Figure 1.3 shows the FEM discretization. These “elements” are usually some polygons, and in many different references, they are also named as “meshes” or “grids”. The vertexes of the elements are known as “nodes” or “points”, on which the unknown variables are prescribed. The values of any location within the element can be evaluated using interpolation by constructing a shape function.

FEM is a powerful tool for solving solid and fluid mechanics. The original governing PDFs in these problems are called the *strong form* for the higher requirement of a strong continuity on the field variables (e.g., displacements, velocities, et al.). The strong form of the PDFs is usually analytically unsolvable. The equivalent integration form of the PDFs can be obtained by using the principle of minimum potential energy, virtual work principle, or Galerkin approach, et al. Such an integration form is called the *weak form*. The weak form reduces the order of the differentiation on trial function, which, in general, offers a more flexible way to get stable and convergent solutions.

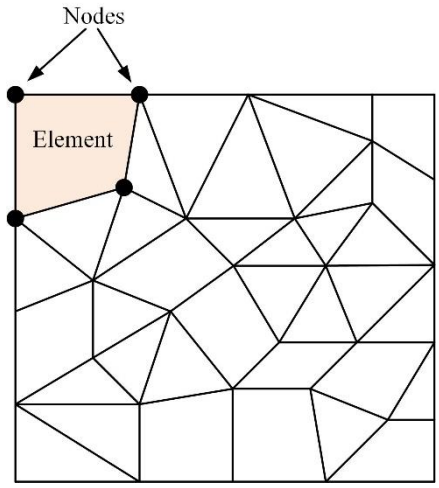

Figure 1.3: An illustration of the FEM discretization

A general FEM procedure usually contains the following main steps: Step (1) the establishment of the weak form; Step (2) domain dissertation; Step (3) shape function construction; Step (4) matrices and vectors formulation in elements. Step (5) global matrices/vectors assembly; Step (6) solution for assumed unknowns.

1.4 Motivation

Despite the advantage of IFEM in solving FSI problems with a solid of finite volume immersed in. The assumption of a fictitious fluid domain, having the same domain of the immersed solid, could be problematic, because, in situations when the solid is assumed as zero volume structures, the fictitious fluid domain also shrinks to occupy no volume. The coupling process of identifying the fictitious fluid particles in the solid meshes fails. Thus the IFEM is unsuitable for analyzing the FSI problems when the structures are modeled as reduced models such as a beam, plate, shell, and others. Although different approaches for accurate modeling of thin structures in solid mechanics have been

developed for decades, only a few of them have been adopted in IBM due to its complicated employment of FSI algorithms for more general cases.

The element-based FEM interpolation, in the IFEM and immersed smoothed FEM (IS-FEM), also makes the influence domain of the solid smaller than the real solid [72]. For an FSI problem with a bulk solid, the problematic interpretation of the FSI interface in IFEM will lead to an undesirable solution even with an excellent meshing scheme. The inaccurate numerical interface is always changing during the calculation, which results in spurious forces oscillations and jeopardizes the convergence performance. The inaccurate interface is indeed the most substantial disadvantage in the immersed type methods that have been criticized for the most.

In this dissertation, a novel Eulerian-Lagrangian-Lagrangian (ELL) method is proposed for solving FSI problems [73-75]. It alleviates the immersed-type methods of having an inaccurate interface and IFEM/IS-FEM trouble coping with thin structures. The key idea is to use a small portion of the fluid to wrap the solid. This "wrapping" fluid is described in the Lagrangian frame, in the same way as the solid, and they are treated as one enlarged "composite solid". Then the conventional immersed domain methods can be implemented. The moving FSI conditions are explicitly and accurately imposed since the conforming meshes can always be achieved in the "composite solid" domain. The primary fluid is refilled by the fictitious fluid domain so that a fixed Eulerian fluid domain in the background is formed. In essence, this method uses Eulerian grids for the fluid, Lagrangian grids for the wrapping fluid, and Lagrangian grids for the immersed solid, and hence it is termed as ELL method for convenience. ELL combines the advantages of the conforming

meshes method that has an accurate FSI interface and the immersed method that has a fixed Eulerian fluid domain.

CHAPTER 2. THE EULERIAN-LAGRANGIAN-LAGRANGIAN FORMULATION

In this chapter, the immersed finite element method (IFEM) is reviewed before the detailed derivation of the ELL method. Based on the fictitious fluid domain method, IFEM was proposed by Zhang et al. in 2004 for solving FSI problems with a flexible solid or soft material occupying a finite volume in the fluid domain [28]. The reproducing kernel particles method (RKPM) replaces the Dirac delta function in conventional; thus, non-uniform Eulerian fluid meshes can be adopted for the fluid solver. Wang et al. used the direct finite element method (FEM) interpolation to track the FSI interface implicitly [67]. However, this approach also has limitations of the inaccurate interpretation of the solid boundary in the fluid domain. It underestimates the influence domain of the solid and also fails when the solid domain shrinks to reduced models, such as beam and shell. Inspired by the IFEM theory, the ELL formulation is derived in detail in this chapter.

2.1 Immersed FEM

2.1.1 Fictitious fluid domain method

Let us consider a typical FSI problem, an incompressible flexible solid with finite volume Ω^s is immersed completely and moving in the fluid domain Ω^f, as shown in Figure 2.1 (a). The solid domain and fluid domain together occupy an entire computational domain $\Omega=\Omega^f \cup \Omega^s$ and intersect at the enclosed surface of the solid $\Gamma^s=\Omega^f \cap \Omega^s$. The motion of a solid particle is defined by $\mathbf{x}^s=\mathbf{x}^s\left(\mathbf{X}^s,t\right)$, and its displacement is $\mathbf{u}^s=\mathbf{x}^s-\mathbf{X}^s$. The spatial and material coordinate of a particle is denoted by **x** and **X,** respectively. The material derivative of displacement obtains the velocity of the solid, i.e., $\mathbf{v}^s = D\mathbf{u}^s/Dt$. The

superscripts '*f*' and '*s*' represent fluid and solid, respectively. The existence of the solid causes the fluid only to occupy the real fluid domain Ω^f; no fluid exists in the space occupied by the solid. The interaction conditions between the fluid and solid should be satisfied only on the intersection surface Γ^s. The solid and fluid domains are indeed time-dependent due to the motion of the solid. Nonslip condition on the FSI interface Γ^s is assumed. The governing equations for this FSI problem are,

$$\rho^f \frac{Dv_i^f}{Dt} = \sigma_{ij,j}^f + \rho^f g_i, \ \mathbf{x}^f \in \Omega^f \tag{2.1a}$$

$$\rho^s \frac{Dv_i^s}{Dt} = \sigma_{ij,j}^s + \rho^s g_i, \ \mathbf{x}^s \in \Omega^s \tag{2.1b}$$

FSI conditions on the fluid-solid interface:

$$\text{Velocity condition: } v_i^f = v_i^s, \text{ on } \Gamma^s \tag{2.1c}$$

$$\text{Forcing condition: } f_i^{FSI,f} = -f_i^{FSI,s}, \text{ on } \Gamma^s \tag{2.1d}$$

where ρ is the density, v_i is velocity and σ_{ij} is Cauchy stress. $f_i^{FSI,f}$ and $f_i^{FSI,s}$ are a pair of the interaction forces between the fluid and solid that exists at the interface. The forcing condition can also be expressed as

$$\sigma_{ij}^f n_j^f = -\sigma_{ij}^s n_j^s \tag{2.2}$$

where n_i^f and n_i^s are the normal outward vectors on the interface from the fluid and solid sides, respectively. For the sake of simplicity, the external force and boundary conditions unrelated to FSI are not considered.

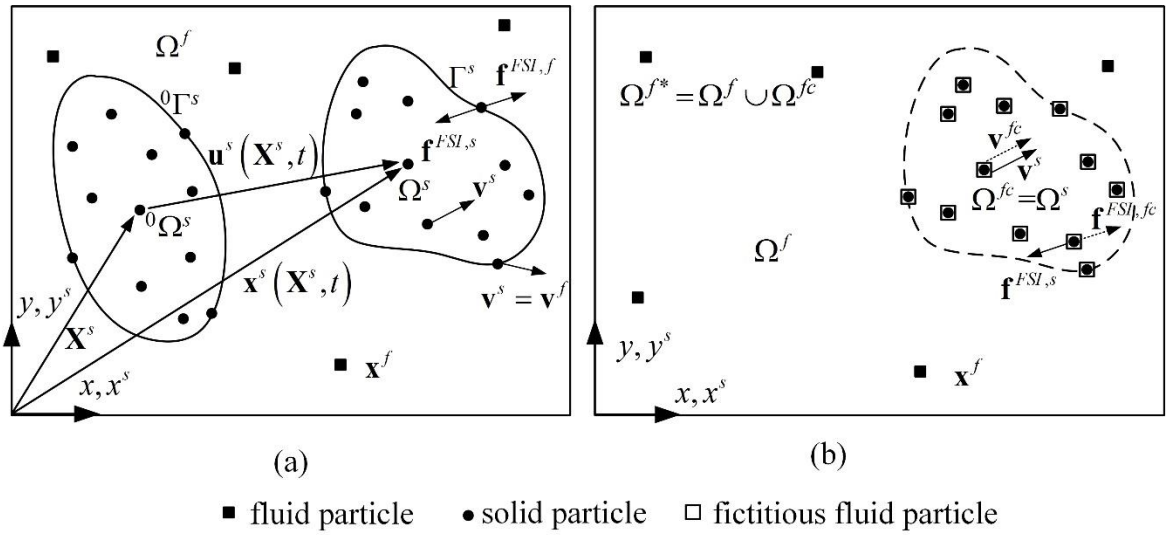

Figure 2.1: (a) Configuration of solid and fluid particles of an FSI system. (b) The fictitious fluid particles in the fictitious fluid domain. The left superscript '*0*' represents the initial configuration of the solid.

The fluid domain is changing with the movement of the solid. To form a time-independent Eulerian fluid domain, we introduce a so-called *fictitious fluid* domain, as illustrated in Figure 2.1 (b). This fictitious fluid occupies the same position of the solid domain, that is $\Omega^{fc}=\Omega^s$ (the superscript '*fc*' denotes for fictitious fluid). Two assumptions are prescribed for the fictitious fluid. (1) The fictitious fluid is the same as real fluid. Therefore its material parameters are the same as the real fluid, i.e., density $\rho^{fc}=\rho^f$ and dynamic viscosity $\mu^{fc}=\mu^f$. (2) The fictitious fluid particles are bounded to and move with solid particles. The first assumption lets the fictitious fluid Ω^{fc} fill in the solid domain Ω^s. Thus, with the original fluid Ω^f, it forms a time-independent fluid domain, which denotes $\Omega^{f*}=\Omega^f\cup\Omega^{fc}$. The second assumption ensures the fictitious fluid has the same velocity of the solid, i.e., $v_i^{f*}=v_i^s$ in Ω^{fc}. In computational practice, it is treated as velocity conditions for the fixed fluid domain. Also, the interaction forces on the FSI interface penetrate the entire fictitious fluid domain to take care of FSI forcing conditions, i.e.,

$f_i^{FSI,fc} = -f_i^{FSI,s}$ in Ω^{fc}. The following equation can evaluate the FSI force in the fictitious fluid domain,

$$f_i^{FSI,fc} = \rho^{fc} \frac{Dv_i^{fc}}{Dt} - \sigma_{ij,j}^{fc} - \rho^{fc} g_i, \ \mathbf{x}^{fc} \in \Omega^{fc} \left(\Omega^{fc} = \Omega^s \right) \tag{2.3}$$

where σ_{ij}^{fc} is the Cauchy stress of the fictitious fluid calculated by using velocity gradient and pressure. The next step is to sum the governing equations in the fictitious fluid domain and the real fluid domain. For the solid part, an additional external force term is added that accounts for FSI forcing interaction. Also, the FSI conditions on the interface now merge into the fictitious fluid domain. The final governing equations of the FSI problem of an immersed moving solid are summarized,

$$\rho^f \frac{Dv_i^{f^*}}{Dt} = \sigma_{ij,j}^{f^*} + \rho^f g_i, \ \mathbf{x}^{f^*} \in \Omega^{f^*} \tag{2.4a}$$

$$\rho^s \frac{Dv_i^s}{Dt} = \sigma_{ij,j}^s + \rho^s g_i, \ \mathbf{x}^s \in \Omega^s \tag{2.4b}$$

The FSI conditions on the fluid-solid are,

$$\text{Velocity condition: } v_i^{f^*} = v_i^s \text{ in } \Omega^s \left(\Omega^s = \Omega^{fc} \right) \tag{2.4c}$$

$$\text{Forcing condition: } f_i^{FSI,s} = -f_i^{FSI,fc} \text{ in } \Omega^s \left(\Omega^s = \Omega^{fc} \right) \tag{2.4d}$$

Note that, in the real physical problem, there is no such fictitious fluid. It is introduced for the easy understanding of the formulation. One can derive the same equations without introducing the concept of fictitious fluid if the same assumptions are imposed when evaluating the FSI forcing term in Equation (2.3). Also, one can regard the integral of external force $f_i^{FSI,s}$ applied on the solid as the drag and lift forces often used

in the computational fluid dynamics (CFD) simulation [40, 41]. A time-independent fluid domain Ω^{f^*} is constructed by introducing a fictitious fluid domain and thus enabling the employment of a fluid solver based on the Eulerian coordinate. Figure 2.2 illustrates the schematic of the IFEM. The solid is moving over the independent Eulerian fluid grids with a fictitious fluid filling in the overlapped domain of solid.

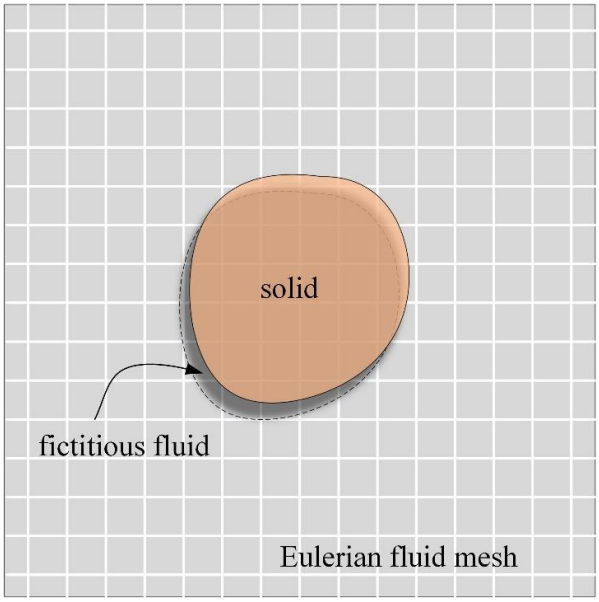

Figure 2.2: Schematic of the IFEM

2.1.2 IFEM algorithm

The solution scheme of the IFEM in Equation (2.4), in principle, is composed of three modules: (1) solving for solid with FSI force condition; (2) solving for fluid with FSI velocity condition; and (3) identifying the FSI conditions. A four-step explicit FEM algorithm for solving immersed solid body FSI problems is given as follows, advancing from time step τ to $\tau+1$.

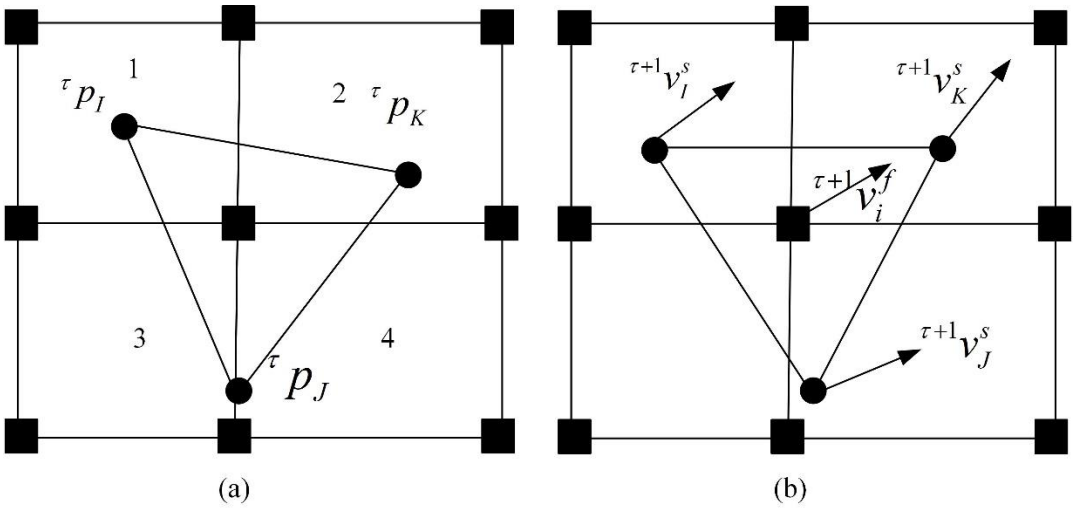

Figure 2.3: The procedure of identifying and interpolating FSI conditions. (a) Searching for solid nodes (fictitious fluid nodes) resides in fluid elements. The nodal pressure of *I* and *K* can be calculated by FEM interpolation in fluid element 1 and 2, respectively, the pressure of node *J* can be interpolated either in fluid element 3 or 4. (b) Searching for fluid nodes reside in the solid elements. The nodal velocity of fluid node *i* is interpolated using solid nodes *I*, *J,* and *K*. (The quadrangular elements are fluid elements, and triangular represents a solid element. Small squares are fluid nodes, and small solid circles are solid nodes.)

Firstly, the solid nodes residing in the fluid elements are searched for, and pressure is interpolated at identified nodes, as shown in Figure 2.3 (a). Secondly, FSI forcing term $^{\tau}f_i^{FSI,s}$ at the time step τ is computed using Equation (2.3) and prescribed onto the solid nodes using Equation (2.4d). With FSI force $^{\tau}f_i^{FSI,s}$ and other external forces applied, the solid velocity $^{\tau+1}v_i^s$ at the time step $\tau+1$ is obtained by solving the solid part in Equation (2.4b). Thirdly, the fluid nodes residing in the solid elements are searched for, and their velocities $^{\tau+1}v_i^{f*}$ in $\Omega^{fc}\left(\Omega^{fc}=\Omega^s\right)$ are calculated by FEM interpolation within the solid meshes, as shown in Figure 2.3 (b). Fourthly, the Eulerian fluid domain Ω^{f*} in Equation (2.4a) is solved for the time step $\tau+1$ concerns the fictitious fluid velocity as velocity constraints.

2.1.3 Drawbacks in IFEM

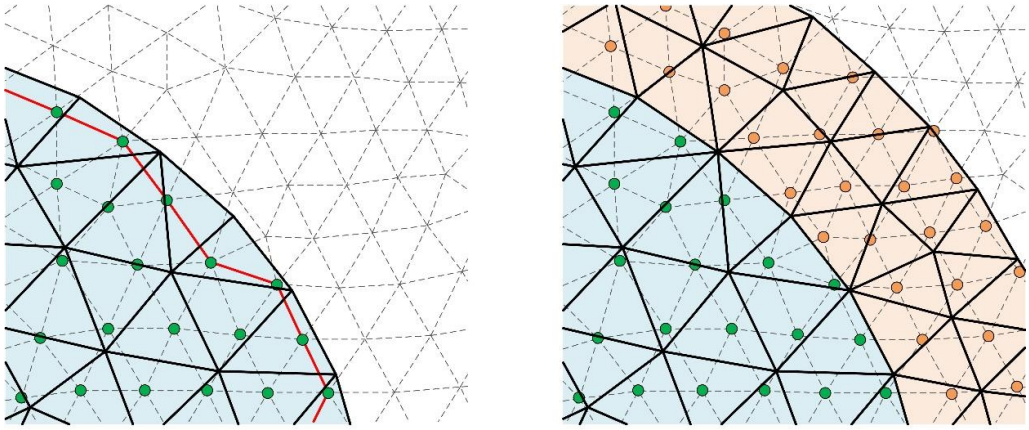

(a) (b)

Figure 2.4: (a) Inaccurate numerical FSI interface in the IFEM method. (b) The smoothed coupling of the velocity boundary condition from solid to fluid in the ELL.

The couplings of the velocity from solid to fluid and the FSI force from fluid to solid are the crucial part of the IFEM approach. Figure 2.4 (a) illustrates the velocity transfer scheme in IFEM. To interpolate the velocity of a fluid node, a solid element to host the fluid node needs to be determined. Then a direct FEM interpolation is used to calculate the velocity of this fluid node within the solid element. The velocity boundary condition only applies to the fluid nodes covered by the solid elements. The computational interface in IFEM is represented by a set of segments connecting the fluid nodes close to the interface inside the solid body, as illustrated by the red lines. This interpretation of interface in the fluid is always smaller than the real interface. The accuracy of the IFEM largely depends on the quality of the fluid grids. The denser the fluid grids are, the more accurate the numerical interface is. The numerical error would be relatively large, especially for a coarse fluid meshing scheme in the FSI zone. Besides, the moving interface causes a

discontinuous change of the computational interface that causes oscillation of the pressure, leading to the spurious force oscillation.

The IFEM method is also not suitable for solving FSI problems when structures are modeled with reduced models such as a beam, plate, and shell. In such cases, the solid meshes can no longer host the fluid nodes; thus, the process of finding fluid (factitious fluid) nodes residing in the solid elements fails (see Figure 2.5), IFEM fails.

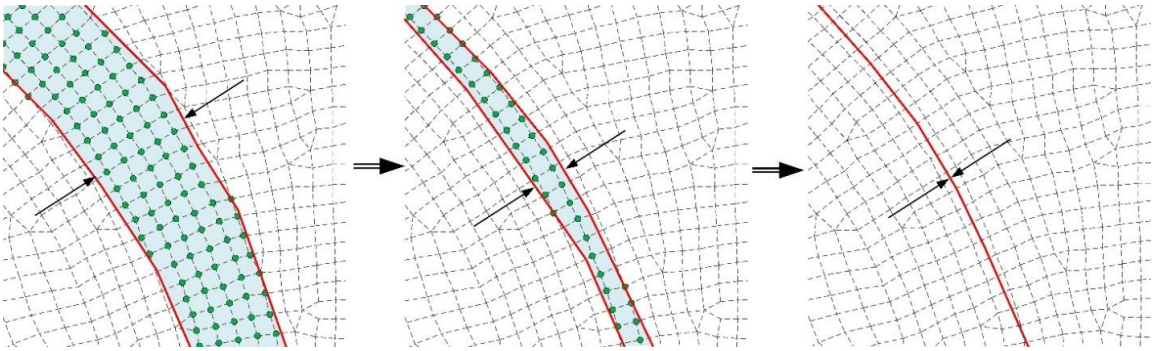

Figure 2.5: The failure of IFEM in identifying fluid nodes residing in the solid domain when the solid shrinks to have no volume.

2.2 ELL method

2.2.1 ELL for bulk solid

Let us go back to the original FSI problem with a bulk solid Ω^s immersed in a fluid domain Ω^f, as shown in Figure 2.1 (a). Now, we separate a small portion of the fluid Ω^{Lf} from the original fluid domain Ω^f to wrap the solid domain, as illustrated in Figure 2.6 (a). The equation for the fluid is divided into two parts, i.e.

$$\rho^f \frac{Dv_i^f}{Dt} = \sigma_{ij,j}^f + \rho^f g_i, \mathbf{x}^f \in \Omega^{Lf} \tag{2.5a}$$

$$\rho^f \frac{Dv_i^f}{Dt} = \sigma_{ij,j}^f + \rho^f g_i, \mathbf{x}^f \in \Omega^f / \Omega^{Lf} \tag{2.5b}$$

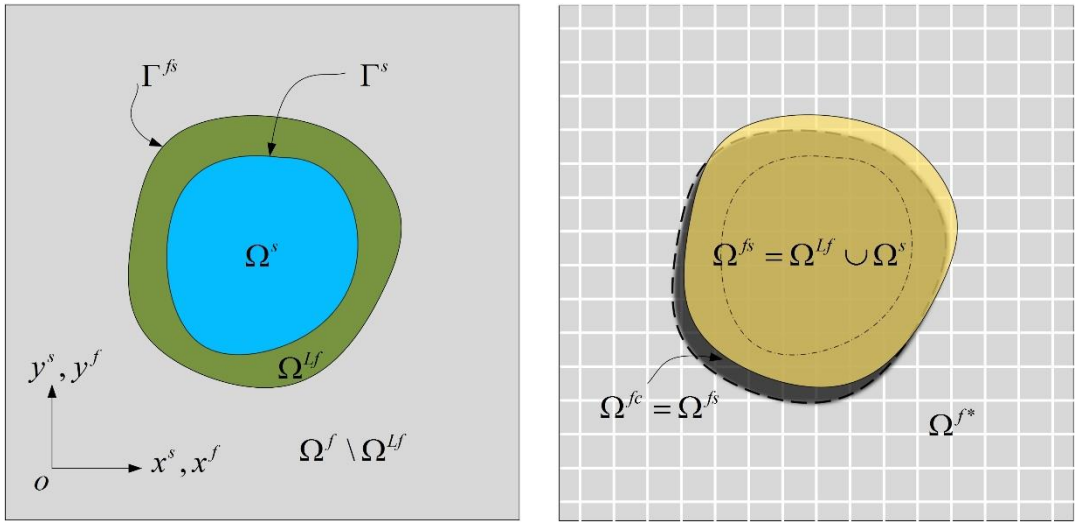

(a) (b)

Figure 2.6: The ELL approach of (a) separation of the wrapping fluid and (b) construction of the "composite solid".

We regroup the wrapping fluid with the solid and regrade them as one enlarged "composite solid" domain, i.e. $\Omega^{fs} = \Omega^{Lf} \cup \Omega^s$. The governing equations of this new FSI system become,

$$\rho^f \frac{Dv_i^f}{Dt} = \sigma_{ij,j}^f + \rho^f g_i, \mathbf{x}^f \in \Omega^f / \Omega^{Lf} \tag{2.6a}$$

$$\rho^{fs} \frac{Dv_i^{fs}}{Dt} = \sigma_{ij,j}^{fs} + \rho^{fs} g_i, \mathbf{x}^{fs} \in \Omega^{fs} \tag{2.6b}$$

FSI conditions on the fluid-solid interface Γ^{fs} are,

Velocity condition: $v_i^f = v_i^{fs}$ on Γ^{fs} (2.6c)

Forcing condition: $f_i^{FSI,f} = -f_i^{FSI,fs}$ on Γ^{fs} (2.6d)

The new FSI interface Γ^{fs} is the enclosed surface of the composite solid, i.e. $\Gamma^{fs} = \partial\Omega^{fs}$. The density, velocity and Cauchy stress of the composite solid are assembled as,

$$\rho^{fs} = \rho^{Lf} + \delta\left(\mathbf{x} - \mathbf{x}^s\right)\left(\rho^s - \rho^{Lf}\right), \quad \mathbf{x} \in \Omega^{fs} \tag{2.7a}$$

$$\mathbf{v}^{fs} = \mathbf{v}^{Lf} + \delta\left(\mathbf{x} - \mathbf{x}^s\right)\left(\mathbf{v}^s - \mathbf{v}^{Lf}\right), \quad \mathbf{x} \in \Omega^{fs} \tag{2.7b}$$

$$\boldsymbol{\sigma}^{fs} = \boldsymbol{\sigma}^{Lf} + \delta\left(\mathbf{x} - \mathbf{x}^s\right)\left(\boldsymbol{\sigma}^s - \boldsymbol{\sigma}^{Lf}\right), \quad \mathbf{x} \in \Omega^{fs} \tag{2.7c}$$

where δ is the Dirac delta function. In practice, this can be done merely by generating sheared nodes at the interface between the solid and the Lagrangian fluid, and a system of matrixes can discretize the dynamics of this composite solid.

Notice that Equation (2.6) has a similar form as Equation (2.1). The difference is that the enlarged composite solid replaces the solid in the original FSI system. Implementing the IFEM approach in Equation (2.4), we have

$$\rho^f \frac{Dv_i^f}{Dt} = \sigma_{ij,j}^f + \rho^f g_i, \mathbf{x}^{f^*} \in \Omega^{f^*} \tag{2.8a}$$

$$\rho^{fs} \frac{Dv_i^{fs}}{Dt} = \sigma_{ij,j}^{fs} + \rho^{fs} g_i, \mathbf{x}^{fs} \in \Omega^{fs} \tag{2.8b}$$

FSI conditions on the fluid-solid domain,

$$\text{Velocity condition:} \quad v_i^f = v_i^{fs} \text{ in } \Omega^{fs} \left(\Omega^{fs} = \Omega^{fc}\right) \tag{2.8c}$$

$$\text{Forcing condition:} \quad f_i^{FSI,fs} = -f_i^{FSI,fc} \text{ in } \Omega^{fs} \left(\Omega^{fs} = \Omega^{fc}\right) \tag{2.8d}$$

The fixed Eulerian domain Ω^{f^*} in the ELL approach should have the same domain as in the original IFEM. The FSI force is evaluated in the new fictitious fluid domain.

The discrepancy of the FSI interface is from the inadequate number of fluid nodes used near the interface to transfer the velocity from solid to fluid, as discussed in the previous section. With the adoption of the ELL approach, this issue is resolved. Figure 2.4(b) shows the meshing scheme of the ELL approach near the FSI interface. The solid domain is enlarged with the Lagrangian fluid. Now, the Eulerian fluid nodes outside the solid domain are also searched for to transfer the velocity coupling. The velocity at the interface is smoothly transferred to the fluid nodes nearby the sharp interface.

Since the wrapped solid and the wrapping Lagrangian fluid are now regarded as one composite solid, shared nodes are always available to generate at the interface in this composite solid domain. If the Lagrangian fluid shrinks to zero, then the ELL degenerates to the regular IFEM with the solid meshes moving on the fixed Eulerian fluid grids. If the Lagrangian fluid domain stretches to have the same domain as the bulk fluid, there is no need to updated the fluid field through the background Eulerian fluid grids, and thus it becomes a body-fitted method. In essence, the ELL approach unifies the body-fitted method and immersed type method.

2.2.2 ELL for thin solid

Consider the situation when the immersed solid shrinks to a thin structure, thus occupying no volume; that is, the thickness of the solid can be ignored, as illustrated in Figure 2.7 (a). In this problem, the fluid domain is represented by Ω^f, and the thin structure domain is Γ^s. The governing equations for solid and fluid are then,

$$\rho^f \frac{Dv_i^f}{Dt} = \sigma_{ij,j}^f + \rho^f g_i, \ \mathbf{x}^f \in \Omega^f \tag{2.9a}$$

$$\rho^s \frac{Dv_i^s}{Dt} = \sigma_{ij,j}^s + \rho^s g_i, \ \mathbf{x}^s \in \Gamma^s \tag{2.9b}$$

FSI conditions on the fluid-solid interface Γ^s,

$$\text{Velocity condition: } v_i^f = v_i^s \text{ on } \Gamma^s \tag{2.9c}$$

$$\text{Forcing condition: } f_i^{FSI,s} = -f_i^{FSI,f} \text{ on } \Gamma^s \tag{2.9d}$$

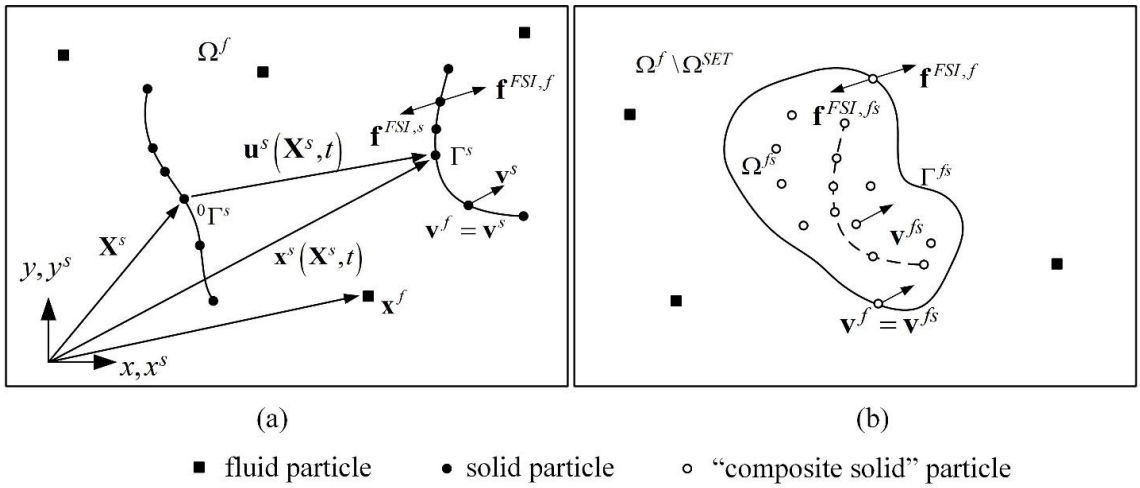

Figure 2.7: Illustrations of (a) the solid configuration and fluid configuration in an FSI system when the solid shrinks to zero thickness, (b) the wrapping fluid to implement the ELL method.

Same as in the ELL for the bulk solid, let us use a small portion of the fluid Ω^{SET} that enwraps the thin structure, as illustrated in Figure 2.7 (b). Combine the fluid in the domain Ω^{SET} with the solid Γ^s and regard them as one mixture composite solid, i.e., $\Omega^{fs} = \Omega^{SET} \cup \Gamma^s$. The governing equation is rewritten as,

$$\rho^f \frac{Dv_i^f}{Dt} = \sigma_{ij,j}^f + \rho^f g_i, \ \mathbf{x}^f \in \Omega^f / \Omega^{fs} \tag{2.10a}$$

$$\rho^{fs} \frac{Dv_i^{fs}}{Dt} = \sigma_{ij,j}^{fs} + \rho^{fs} g_i, \ \mathbf{x}^{fs} \in \Omega^{fs} \tag{2.10b}$$

FSI conditions on the fluid-solid interface,

$$\text{Velocity condition: } v_i^f = v_i^{fs} \text{ on } \Gamma^{fs} \tag{2.10c}$$

$$\text{Forcing condition: } f_i^{FSI,f} = -f_i^{FSI,fs} \text{ on } \Gamma^{fs} \tag{2.10d}$$

where Γ^{fs} is the enclosed surface of the composite solid. Again, the above equations are similar to the original governing equations in deriving the IFEM method. Substituting Equation (2.10) into Equation (2.4) gives

$$\rho^f \frac{Dv_i^f}{Dt} = \sigma_{ij,j}^f + \rho^f g_i, \ \mathbf{x}^f \in \Omega^f \tag{2.11a}$$

$$\rho^{fs} \frac{Dv_i^{fs}}{Dt} = \sigma_{ij,j}^{fs} + \rho^{fs} g_i, \ \mathbf{x}^{fs} \in \Omega^{fs} \tag{2.11b}$$

FSI condition:

$$\text{Velocity condition: } v_i^f = v_i^{fs} \text{ in } \Omega^{fs} \tag{2.11c}$$

$$\text{Forcing condition: } f_i^{FSI,fs} = -f_i^{FSI,fc} \text{ in } \Omega^{fs} \tag{2.11d}$$

where $f_i^{FSI,fc}$ is obtained by substituting the density, velocity and Cauchy stress variables of the assumed fictitious fluid for this case into Equation (2.3), that is

$$f_i^{FSI,fc} = \rho^f \frac{Dv_i^{fs}}{Dt} - \sigma_{ij,j}^{fs} - \rho^f g_i, \ \mathbf{x}^{fc} \in \Omega^{fc} \left(\Omega^{fc} = \Omega^{fs}\right) \tag{2.12}$$

Figure 2.8 shows the scheme of the ELL approach for a thin solid. By enlarging the thin solid to a finite composite solid, ELL effectively overcomes the issue in the conventional IFEM when the immersed solid shrinks to occupy zero volume.

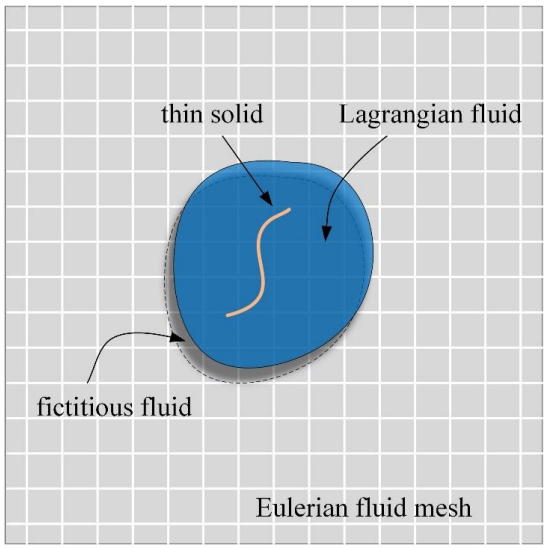

Figure 2.8: Schematic of the ELL approach with a thin solid body

2.3 A physical interpretation of ELL

Although the combination of a Lagrangian fluid and Eulerian fluid in one method is unusual, the mechanism behind it is simple and fundamental. Here, we address this idea with the emphasis on the two fluid parts. Figure 2.9 shows the illustration of the ELL method for thin structure within one algorithm loop from time steps τ to $\tau+1$. The wrapping fluid is described by the Lagrangian frame and background fluid by the Eulerian frame. Since there is only one real fluid particle in a particular position. The field variables, such as velocities and pressure of this particle, should be the same despite what coordinate systems are used to observe. For example, point *i* in Lagrangian fluid should have the same field value to its corresponding point *I* in the Eulerian fluid. From the physical aspect of view, they are the same material particle at this transient time step τ. The external forces at this pair of points should be equal. Now, we can calculate the Lagrangian fluid with the consideration of the external force in the new time step $\tau+1$; it deforms to an updated

domain ${}^{\tau+1}\Omega^{Lf}$ (together with the solid). The Lagrangian fluid point i moves to a new spatial position i' and in Eulerian position, J. (i and i' are the same material fluid point, the i' means the material point at the new time step.) At the updated time step $\tau+1$, the fluid material point i' in the Lagrangian fluid is the same as its corresponding material point J in the Eulerian coordinate. Thus the velocity at point J must be the same as the point i' at the time step $\tau+1$, which is then treated as the velocity boundary conditions for calculating field variables in the Eulerian fluid domain.

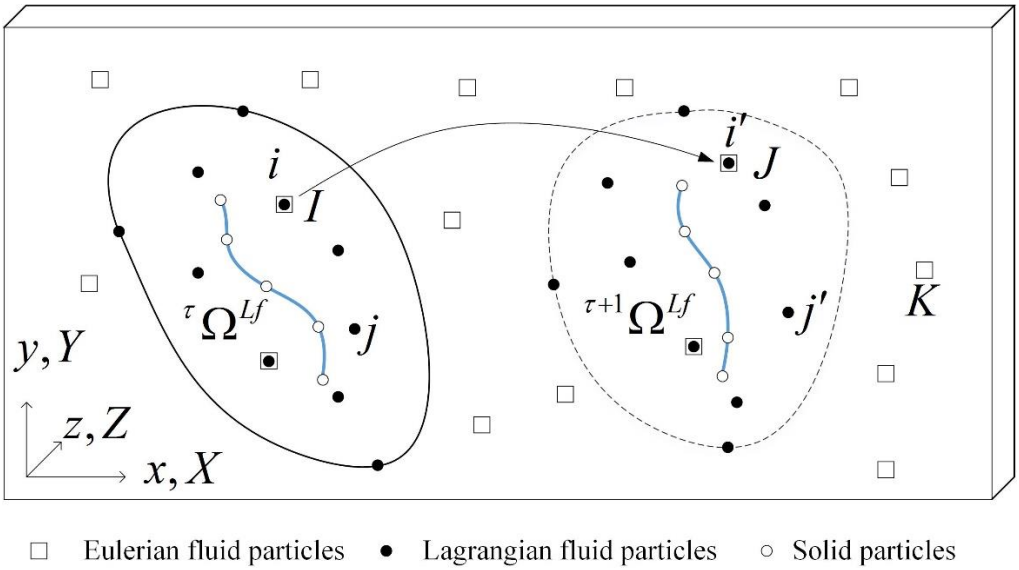

Figure 2.9: Illustration of the Lagrangian fluid configuration and Eulerian fluid configuration in the ELL method. Solid circles are Lagrangian fluid particles; hollow squares are Eulerian fluid particles, and empty circles are solid particles.

CHAPTER 3. ALGORITHMS

The ELL method includes three fundamental components, as discussed previously, they are Eulerian fluid, a small portion of the Lagrangian fluid, and solid in the Lagrangian frame. The algorithms, based on the FEM discretization, accounting for all these three modules, will be illustrated in this chapter. For the thin structure, the CB beam is for the 2D and CB shell for the 3D. Since the Cauchy stress is the stress measure for the fluid, the updated Lagrangian scheme is a natural choice for the Lagrangian fluid part. The Eulerian fluid is solved by a characteristic-based split (CBS) algorithm. The ELL algorithm assembles these modules are given at the end of this chapter.

3.1 Updated Lagrangian FEM for fluid dynamics

In a CFD simulation, Eulerian mesh, where the fluid domain and grids stay unchanged during the calculation, is usually the first choice. However, in many other cases, for example, the wave propagates to the shore, free-surface flow, and so on, a Lagrangian mesh for fluid flows can be more suitable [76, 77]. When a fluid is described under a Lagrangian frame, the general governing equation is written as,

$$\rho^f \frac{\partial v_i^f}{\partial t} = \sigma_{ij,j}^f + \rho^f b_i, \mathbf{x}^f \in \Omega^f \tag{3.1a}$$

$$n_j \sigma_{ij}^f = \overline{t}_i \text{ on } \Gamma^f \tag{3.1b}$$

The fluid domain Ω^f in this subchapter represents the general fluid domain under the Lagrangian frame. b_i is the generalized body force, n_i and $\overline{t}_i$ are the normal vector and

traction on the boundary. Cauchy stress σ_{ij}^{f} in the fluid (Newtonian) is computed using the following constitutive equation,

$$\sigma_{ij}^{f} = -p\delta_{ij} + 2\mu d_{ij} \tag{3.2}$$

where μ is the dynamic viscosity, and p is the pressure. d_{ij} is the rate of deformation tensor

$$d_{ij} = \frac{1}{2}\left(v_{i,j} + v_{j,i}\right) \tag{3.3}$$

One significant difficulty in dealing with the incompressible fluid using a Lagrangian description is the pressure term in Equation (3.2). An artificial compressibility method or a penalty method is widely used to handle this difficulty [78 - 82]. In the artificial compressibility method, the relation between pressure and velocity is connected using the following equation,

$$-\frac{1}{c^2}\frac{\partial p}{\partial t} = v_{i,i} \tag{3.4}$$

where c is the speed of the sound, and in practice, we usually choose a sufficiently large number. The relation above is used to update the pressure term when a central difference based time discretized explicit method is employed to solve the nonlinear equation. Knowing the pressure at time step τ and velocity field in time step $\tau + 1/2$, we can calculate the pressure in time step $\tau + 1$,

$$-\frac{1}{c^2}\frac{{}^{\tau+1}p - {}^{\tau}p}{\Delta t} = {}^{\tau+1/2}v_{i,i} \tag{3.5}$$

If one defines $\kappa = c^2 \Delta t$, the artificial compressibility method becomes a penalty method, the equivalence of the two methods has been discussed in [80], and one physical interpretation of constant κ is the bulk modulus of the fluid.

To render the governing equations in finite element form, we should recast Equation (3.1) in the weak form [83],

$$\int_{\Omega^f} \frac{\partial(\delta v_i)}{\partial x_j} \sigma_{ij}^f d\Omega - \int_{\Omega^f} \delta v_i \rho^f b_i d\Omega - \int_{\Gamma^f} \delta v_i t_i d\Gamma + \int_{\Omega^f} \delta v_i \rho^f \dot{v}_i d\Omega = 0 \tag{3.6}$$

The discretization of Equation (3.6) is achieved by introducing the finite element interpolation of the test and trial function,

$$v_i^f = N_I v_{Ii}^f \tag{3.7a}$$

$$\delta v_i^f = N_I \delta v_{Ii}^f \tag{3.7b}$$

where N_I is the so-called shape function, and v_{Ii}^f is nodal velocity, δv_{Ii}^f is the virtual velocity at the node. *I* is the nodal number. By substituting the interpolation function into Equation (3.6), we can obtain the discretized form,

$$\begin{aligned} \delta v_{iI} \int_{\Omega^f} \frac{\partial N_I}{\partial x_j} \sigma_{ij}^f d\Omega - \delta v_{iI} \int_{\Omega^f} N_I \rho^f b_i d\Omega - \delta v_{iI} \int_{\Gamma^f} N_I t_i d\Gamma \\ + \delta v_{iI} \int_{\Omega^f} N_I N_J \rho^f \dot{v}_{Ji} d\Omega = 0 \end{aligned} \tag{3.8}$$

Using the arbitrariness of the δv_{iI}^f, we arrive at,

$$\int_{\Omega^f} \frac{\partial N_I}{\partial x_j} \sigma_{ij}^f d\Omega - \int_{\Omega^f} N_I \rho^f b_i d\Omega - \int_{\Gamma^f} N_I t_i d\Gamma + \int_{\Omega^f} N_I N_J \rho^f \dot{v}_{Ji} d\Omega = 0 \tag{3.9}$$

A well-known concise discretization formulation for the nonlinear finite element is given as follows,

$$M_{IJ}^{f} a_{Ji}^{f} = f_{Ii}^{ext,f} - f_{Ii}^{int,f} \tag{3.10}$$

where f^{ext} is the external force vector accounts for the body force and the traction, and f^{int} is the internal force vector from the Cauchy stress. M_{IJ} is the mass matrix and $a_{Ji} = \dot{v}_{Ji}$ is the nodal acceleration vector.

3.2 Continuum-based (CB) beam element

Reduced elements in FEM, such as beam and shell elements, are invaluable in the modeling of thin and slender engineered components and natural structures, for example, turbine blades, flapping flags, and falling leaves. A large number of elements are required to model these types of structures using continuum elements, thus leading to costly computations. The continuum-based (CB) beam element is among the widely used method to model thin beams due to its simple and straightforward theory [83-85,]. Figure 3.1 shows a CB element and its parent continuum element. The *master nodes* are the nodes of common beam element where the unknowns or degrees of freedom are assumed and prescribed. The *slave nodes* are located on the top and bottom of the element and generated through master nodes to form a standard continuum element, i.e., the strain, stress, and the internal force of the beam are computed using slave nodes. Each of the master nodes has a couple of slave nodes.

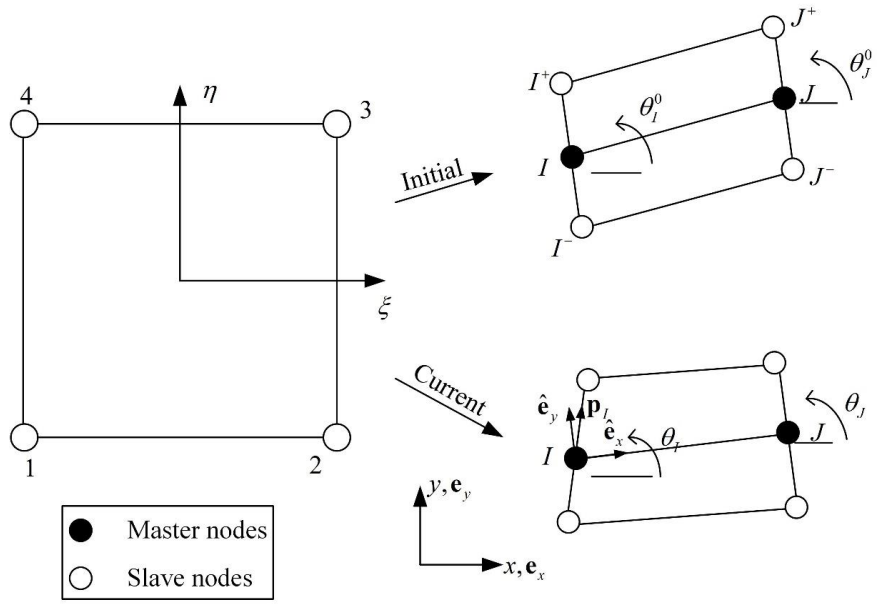

Figure 3.1: A two-node CB beam element and its underlying parent 4-node (Q4) continuum element.

The lines linking the adjacent master nodes or adjacent slave nodes are called *laminae*. *Fibers* are lines that span from the bottom slave node to the top slave node. The unit vector **p** along the fiber is named *the director*. The corotational basis $\{\hat{\mathbf{e}}_x, \hat{\mathbf{e}}_y\}$ at any point in the element. Where $\hat{\mathbf{e}}_x$ is defined as being always tangent to the laminae, and $\hat{\mathbf{e}}_y$ being normal to the laminae. Notice that $\hat{\mathbf{e}}_y$ is not necessarily in the same direction as the director. The corotational basis $\{\hat{\mathbf{e}}_x, \hat{\mathbf{e}}_y\}$ can be expressed in terms of the Euclidean base vectors $\{\mathbf{e}_x, \mathbf{e}_y\}$ as follows,

$$\begin{bmatrix} \hat{\mathbf{e}}_x \\ \hat{\mathbf{e}}_y \end{bmatrix} = \begin{bmatrix} \dfrac{x_{,\xi}}{\sqrt{x_{,\xi}^2 + y_{,\xi}^2}} & \dfrac{y_{,\xi}}{\sqrt{x_{,\xi}^2 + y_{,\xi}^2}} \\ \dfrac{-y_{,\xi}}{\sqrt{x_{,\xi}^2 + y_{,\xi}^2}} & \dfrac{x_{,\xi}}{\sqrt{x_{,\xi}^2 + y_{,\xi}^2}} \end{bmatrix} \begin{bmatrix} \mathbf{e}_x \\ \mathbf{e}_y \end{bmatrix} \tag{3.11}$$

where $x_{,\xi}$ and $y_{,\xi}$ represent the derivatives of the current coordinates x and y of the considered point to the corresponding parent coordinate ξ.

Three assumptions should be imposed for the CB beam theory to represent the behavior of a standard beam element feasibly. (1) The fibers remain straight; (2) the fibers are inextensible; (3) the transverse normal stress is negligible, i.e. $\hat{\sigma}_{yy} = 0$. The unknown displacement vector and position vector at master node I are

$$\mathbf{d}_I = \begin{bmatrix} u_{xI} & u_{yI} & \delta\theta_I \end{bmatrix}^T \tag{3.12a}$$

$$\mathbf{x}_I = \begin{bmatrix} x_I & y_I & \theta_I \end{bmatrix}^T \tag{3.12b}$$

where u_x and u_y are displacement at x and y-direction, respectively. $\delta\theta$ is angular displacement. Other variables, if necessary, such as velocity and acceleration, could be obtained by calculating the time derivatives of either the displacement or position vector. By imposing the straight and inextensible fiber assumption, the coordinates of a couple of slave nodes thus can be calculated readily as,

$$\mathbf{x}_I^+ = \mathbf{x}_I + \frac{1}{2} h_I \mathbf{p}_I(t) \tag{3.13a}$$

$$\mathbf{x}_I^- = \mathbf{x}_I - \frac{1}{2} h_I \mathbf{p}_I(t) \tag{3.13b}$$

where $\mathbf{p}_I(t)$ is the director at master node I, and h_I is the thickness of the beam. The standard isoparametric Q4 element based on the continuum theory could be adopted in terms of the slave node motions,

$$\mathbf{x} = \sum_{I=1}^{2n_N} \mathbf{x}_{I^*} N_{I^*}(\xi, \eta) \tag{3.14}$$

$N_{I^*}(\xi, \eta)$ is the standard shape function for continua. The superscript asterisks represent all slave nodes within a CB element for the sake of convenience. n_N is the total number of the master nodes of an element, which is two in this thesis. Other variables, if necessary, such as displacement, velocity, and acceleration in an element, could also be calculated via the same interpolation.

Cauchy stress σ_{ij} can be calculated by constitutive equation either using Green strain E_{ij} in large strain case or Almansi strain ε_{ij} in small strain case [86]. Alternatively, in many more general cases, Cauchy stress is obtained by using the rate of deformation tensor $D_{ij} = \frac{1}{2}\left(v_{i,j} + v_{j,i}\right)$. The corotational Cauchy stress should be calculated on a corotational basis to impose the third assumption, and given by,

$$\hat{\boldsymbol{\sigma}} = \mathbf{R}^T \boldsymbol{\sigma} \mathbf{R} \tag{3.15}$$

R_{ij} is the orthogonal transformation tensor representing the rotation between the Euclidean basis $\{\mathbf{e}_x, \mathbf{e}_y\}$ and the corotational basis $\{\hat{\mathbf{e}}_x, \hat{\mathbf{e}}_y\}$, that is defined as,

$$\mathbf{R} = \begin{bmatrix} \mathbf{e}_x \cdot \hat{\mathbf{e}}_x & \mathbf{e}_x \cdot \hat{\mathbf{e}}_y \\ \mathbf{e}_y \cdot \hat{\mathbf{e}}_x & \mathbf{e}_y \cdot \hat{\mathbf{e}}_y \end{bmatrix} \tag{3.16}$$

The internal force at a slave node I^* can be obtained by integration over the corresponding structural volume,

$$f_{I^*_i}^{int} = \int_\Omega N_{I^*_i,j} \sigma_{ij} d\Omega \tag{3.17}$$

Neither full quadrature nor the selective-reduced quadrature used in the standard continuum element would result in shear locking. A single stack of quadrature points at $\xi = 0$ is performed to circumvent shear locking. This quadrature scheme is also called selective-reduced quadrature. The trapezoidal rule is often considered because of its effectiveness for less smooth functions. Once the internal force of the slave node is obtained, the internal force at the corresponding master node *I* can then be calculated by a transformation formulation, such that,

$$f_{Ii}^{int} = T_{ij} f_{I^* j}^{int} \tag{3.18}$$

where f_{Ii}^{int} represents the internal force at the master node *I* and is composed of three components. The vector form of the internal force is

$$\mathbf{f}_I^{int} = \begin{bmatrix} f_{Ix}^{int} & f_{Iy}^{int} & m_I^{int} \end{bmatrix}^T \tag{3.19}$$

f_{Ix}^{int} and f_{Iy}^{int} are the internal force at *x* and *y*-direction, respectively, and m_I^{int} denotes the corresponding bending moment. **T** is the transformation matrix, and the expanded form of the Equation (3.19) that calculates internal force at master node *I* in terms of its corresponding slave nodes is,

$$\begin{bmatrix} f_{Ix}^{int} \\ f_{Iy}^{int} \\ m_I^{int} \end{bmatrix} = \begin{bmatrix} 1 & 0 & 1 & 0 \\ 0 & 1 & 0 & 1 \\ y_I - y_{I^-} & x_I - x_{I^-} & y_I - y_{I^+} & x_I - x_{I^+} \end{bmatrix} \begin{bmatrix} f_{I^- j}^{int} \\ f_{I^- j}^{int} \\ f_{I^+ j}^{int} \\ f_{I^+ j}^{int} \end{bmatrix} \tag{3.20}$$

After the spatial discretization of the CB beam system, the equations of the motion at a master node are given by,

$$M_{IJ}^{s} a_{Ji}^{s} = f_{Ii}^{ext,s} - f_{Ii}^{int,s} \tag{3.21}$$

The superscript '*s*' denotes the CB beam here, to distinguish the discretized system of Lagrangian fluid. M_{IJ} is the mass matrix. A lump mass matrix is required when adopting an explicit algorithm to achieve the transient solution of Equation (3.21). For the CB beam, two techniques are often used to obtain diagonal mass matrices that are, (1) the row sum technique, and (2) physical lumping. (See detail in [83]). The external force vector is first evaluated at the slave nodes and then deduced at the master nodes in the same manner of calculating internal force at master nodes in Equation (3.20).

3.3 Continuum-based (CB) shell element

This subchapter discusses the continuum-based (CB) shell element to model the thin structure in the 3D FSI problem. The mixed interpolation of the tensorial component is adopted to remedy the shear locking in the element.

3.3.1 The fundamental idea and FEM formulation

The analysis of shell is one of the most challenging problems in structural mechanics. Developing a general FEM shell element has been a very active research topic for many years. The continuum-based (CB) shell element has gained the hottest interest since Ahamd et al. first proposed its formulation [**87**]. In CB shell, the strain and stress conditions degenerate from a standard three-dimensional solid element. Based on this idea, Dvorkin and Bathe developed a mixed interpolation of the tensorial component, well

known as the MITC element, to remedy the shear locking in the CB shell element [88-90]. This MICT element can be effectively applied to geometric nonlinear problems with conditions of massive displacement and rotation but small strain, as well as material nonlinear analysis. Hughes and Liu further showed its extensive application in the general nonlinear analysis [91].

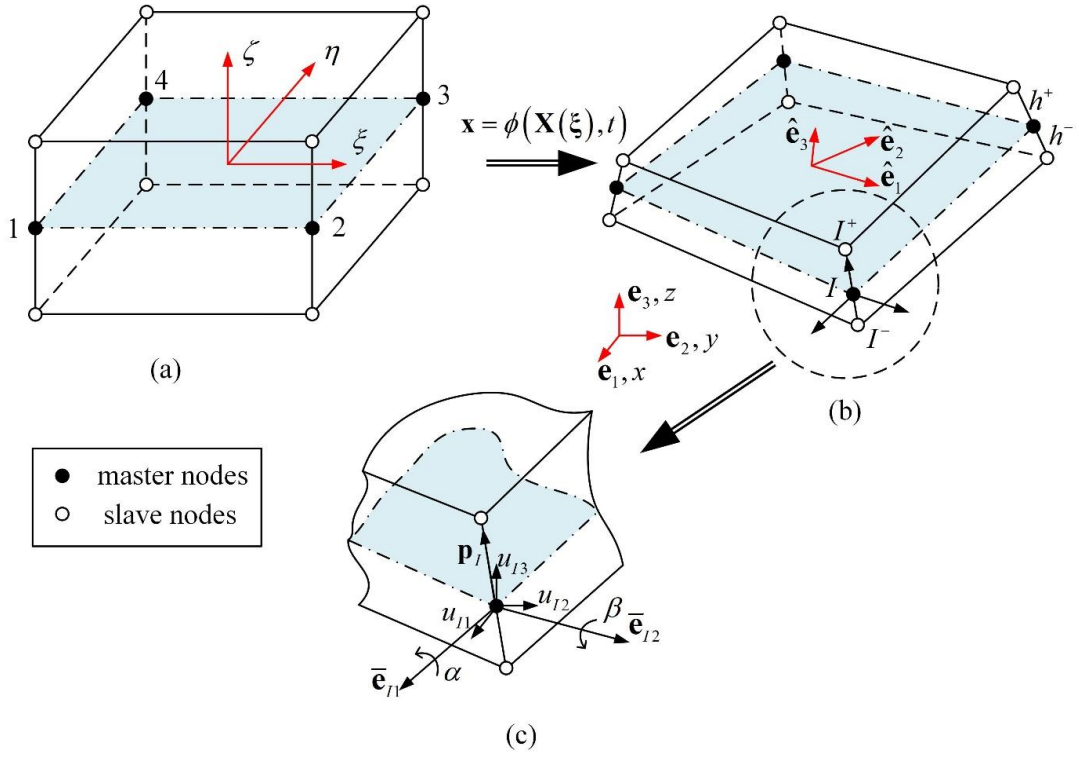

Figure 3.2: A four-node CB shell element and its underlying parent 8-node (H8) continuum element.

The kinematical formulation of the shell element is established on a three-dimensional solid element. Figure 3.2 shows a CB element with four master nodes with eight slave nodes connecting to form a three-dimensional solid element. The nodes on the mid-surface are called master nodes illustrated in solid circles. Each master node has a pair of slave nodes shown in the hollow spheres located on the vertexes of the hexahedron.

Lines that connect master and slave nodes are directors. The underlying assumptions for the CB shell element are:

(1) The director remains a straight line.

(2) The stress along the shell thickness is zero.

(3) The balance of the momentum along the director is ignored.

The first assumption is also known as the revised Mindlin-Reissner assumption, and the second one is the plane stress assumption. The lengths of directors are conventionally defined as the thickness of the shell and usually assumed to remain constant. Each of the slave nodes has three degrees of freedom in general global coordinate. However, for the master nodes, it contains an additional two rotational degrees of freedom (α and β) about basis vectors $\bar{\mathbf{e}}_1$ and $\bar{\mathbf{e}}_2$. The director **p** and these two base vectors are a set of orthogonal base vectors at master nodes. They have the arbitrary choice and are usually predefined before simulation and updated during the simulation (see [83] for detailed definition and updating formulation). The coordinate of slave nodes pair can be translated in the coordinate of the master nodes using,

$$\mathbf{x}_{I^-} = \mathbf{x}_I - h_I^- \mathbf{p}_I \tag{3.22a}$$

$$\mathbf{x}_{I^+} = \mathbf{x}_I + h_I^+ \mathbf{p}_I \tag{3.22b}$$

where h^+ and h^- are the upper and lower thickness of the director. They are not necessarily to be identical, but in most applications, it is a convenience to assume they are equal and remain constant during computation. Knowing the coordinate of the slave nodes, a standard isoparametric finite element approach can then be established on these nodes, i.e.,

$$\mathbf{x}(\xi,t)=\sum_{I^-=1}^{n_N}\mathbf{x}_{I^-}(t)N_{I^-}(\xi)+\sum_{I^+=1}^{n_N}\mathbf{x}_{I^+}(t)N_{I^+}(\xi)=\sum_{I^*=1}^{2n_N}\mathbf{x}_{I^*}(t)N_{I^*}(\xi) \tag{3.23}$$

The superscript asterisks represent all slave nodes in a CB shell element for the sake of convenience. *N* is the shape function for the solid element. n_N is the total number of the master nodes. In this thesis, we use four master nodes with eight slave nodes that form a standard H8 (the hexahedral element with eight nodes) element. Other variables, such as displacement, velocity, and acceleration, could also be evaluated using similar interpolation.

3.3.2 Local coordinate system and constitutive law

To impose the zero stress assumption, a local coordinate system with base vectors ($\hat{\mathbf{e}}_x$, $\hat{\mathbf{e}}_y$ and $\hat{\mathbf{e}}_z$) is established at each integral point. There are several different ways to build this local coordinate system, e.g., Dvorkin in [90] and Hughes in [91]. Hughes' method is adopted; the objective is to find a set of orthonormal base vectors $\hat{\mathbf{e}}_i$ as close as possible to the covariant base vectors $\mathbf{g}_\alpha$. Where the base vectors $\mathbf{g}_\alpha$ define a plane tangent to the lamina that is,

$$\mathbf{g}_\alpha=\frac{\partial\mathbf{x}}{\partial\xi^\alpha} \tag{3.24}$$

The local base vector normal to this plane is defined by,

$$\hat{\mathbf{e}}_z=\frac{\mathbf{g}_1\times\mathbf{g}_2}{\|\mathbf{g}_1\times\mathbf{g}_2\|} \tag{3.25}$$

The other two new base vectors are constructed by,

$$\hat{\mathbf{e}}_x = \frac{\mathbf{a}-\mathbf{b}}{\|\mathbf{a}-\mathbf{b}\|}, \quad \hat{\mathbf{e}}_y = \frac{\mathbf{a}+\mathbf{b}}{\|\mathbf{a}+\mathbf{b}\|} \tag{3.26}$$

where **a** and **b** are auxiliary vectors and defined as,

$$\mathbf{a} = \frac{\mathbf{g}_1}{\mathbf{g}_1} + \frac{\mathbf{g}_2}{\|\mathbf{g}_2\|}, \ \mathbf{b} = \hat{\mathbf{e}}_z \times \mathbf{a} \tag{3.27}$$

The strain is then transformed to the local coordinate system after this setup,

$$\hat{\boldsymbol{\varepsilon}} = \mathbf{R}^T \boldsymbol{\varepsilon} \mathbf{R} \tag{3.28}$$

where **R** is the transformation matrix defined as $R_{ij} = e_i \bullet \hat{e}_j$. The CB shell element can adopt all forms of general material constitutive law used for 3D solid materials. A general 3D elastic constitutive law in the Voigt form is

$$\begin{Bmatrix} \hat{\sigma}_{xx} \\ \hat{\sigma}_{yy} \\ \hat{\tau}_{xy} \\ \hat{\tau}_{xz} \\ \hat{\tau}_{yz} \\ \hat{\sigma}_{zz} \end{Bmatrix} = \begin{bmatrix} \hat{\mathbf{C}}_{aa} & \hat{\mathbf{C}}_{ab} \\ \hat{\mathbf{C}}_{ab}^T & \hat{\mathbf{C}}_{bb} \end{bmatrix} \begin{Bmatrix} \hat{\varepsilon}_{xx} \\ \hat{\varepsilon}_{yy} \\ 2\hat{\gamma}_{xy} \\ 2\hat{\gamma}_{xz} \\ 2\hat{\gamma}_{yz} \\ \hat{\varepsilon}_{zz} \end{Bmatrix} \tag{3.29}$$

The stress and strain components along the thickness are re-ordered to stay in the last row. The matrices $\hat{\mathbf{C}}_{aa}$ (5×5) and $\hat{\mathbf{C}}_{ab}$ (5×1) are submatrices of the tangent modulus matrix. Introducing the plane stress condition $\hat{\sigma}_{zz} = 0$ in the above equation, the nonzero stress can be obtained by eliminating the sixth equation, and giving a 5×5 modified modulus matrix,

$$\tilde{\mathbf{C}}^P = \hat{\mathbf{C}}_{aa} - \hat{\mathbf{C}}_{ab}\hat{\mathbf{C}}_{bb}^{-1}\hat{\mathbf{C}}_{ab}^T \tag{3.30}$$

The constitutive law is then changed as,

$$\begin{Bmatrix} \hat{\sigma}_{xx} \\ \hat{\sigma}_{yy} \\ \hat{\tau}_{xy} \\ \hat{\tau}_{xz} \\ \hat{\tau}_{yz} \end{Bmatrix} = \tilde{\mathbf{C}}^{P} \begin{Bmatrix} \hat{\varepsilon}_{xx} \\ \hat{\varepsilon}_{yy} \\ 2\hat{\gamma}_{xy} \\ 2\hat{\gamma}_{xz} \\ 2\hat{\gamma}_{yz} \end{Bmatrix} \tag{3.31}$$

3.3.3 Shear locking and assumed natural strain

The CB shell element suffers a fundamental problem inherent in its use of FEM interpolation of displacement, and calculation of strain using derivative of displacement. More precisely, this is because the transverse shear strains are not able to vanish at all points of the lower order element, thus makes the element stiffer and 'lock' when the shell becomes thin.

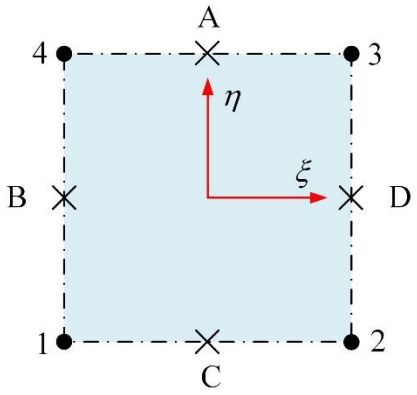

Figure 3.3: Tying positions A, B, C and D for the assumed transverse shear strain field of the MITC4 shell element. The constant transverse shear strain conditions are imposed along its edges.

To circumvent this problem, instead of calculating transverse shear strain via strain-displacement strain relation, Dvorkin and Bathe invented the mixed interpolation of tensorial component (MITC) element by interpolating the transverse shear strain using

strain value in a specific location [88-90]. This interpolation is also known as assumed natural strain (ANS) or assumed strain element [92]. The assumed transverse shear strains ($\bar{\gamma}_{\xi\zeta}$ and $\bar{\gamma}_{\eta\zeta}$) within an element is interpolated by,

$$\bar{\gamma}_{\xi\zeta} = \frac{1}{2}(1+\eta)\gamma^A_{\xi\zeta} + \frac{1}{2}(1-\eta)\gamma^C_{\xi\zeta} \tag{3.32a}$$

$$\bar{\gamma}_{\eta\zeta} = \frac{1}{2}(1+\xi)\gamma^B_{\eta\zeta} + \frac{1}{2}(1-\xi)\gamma^D_{\eta\zeta} \tag{3.32b}$$

The transverse shear strains in typing points A, B, C, D, as shown in Figure 3.3, are calculated by the regular strain-displacement relation.

3.3.4 The discrete equation of motion

The external and internal force vectors are first evaluated on the slave nodes and then translated on the master nodes. A transformation matrix $\mathbf{T}_I$ is used to correlate forces on the master node I and its corresponding pair slave nodes,

$$\mathbf{f}_I = \mathbf{T}_I^T \begin{Bmatrix} \mathbf{f}_{I^-} \\ \mathbf{f}_{I^+} \end{Bmatrix} \tag{3.33}$$

where $\mathbf{T}$ is a 6×5 matrix. Assuming the different value for the upper and lower thickness of the director, the transformation matrix has the following expression,

$$\mathbf{T}_I = \begin{bmatrix} \mathbf{I}_{3\times3} & -h_I^- \mathbf{\Lambda} \\ \mathbf{I}_{3\times3} & h_I^+ \mathbf{\Lambda} \end{bmatrix}, \quad \mathbf{I}_{3\times3} = \begin{bmatrix} 1 & 0 & 0 \\ 0 & 1 & 0 \\ 0 & 0 & 1 \end{bmatrix},$$
$$\mathbf{\Lambda} = \begin{bmatrix} \cos(\bar{\mathbf{e}}_{I1}, \mathbf{e}_1) & \cos(\bar{\mathbf{e}}_{I2}, \mathbf{e}_1) \\ \cos(\bar{\mathbf{e}}_{I1}, \mathbf{e}_2) & \cos(\bar{\mathbf{e}}_{I2}, \mathbf{e}_2) \\ \cos(\bar{\mathbf{e}}_{I1}, \mathbf{e}_3) & \cos(\bar{\mathbf{e}}_{I2}, \mathbf{e}_3) \end{bmatrix} \tag{3.34}$$

Then, the discrete equations of the motion are built at master nodes,

$$M_{IJ}^{s} a_{Ji}^{s} = f_{Ii}^{ext,s} - f_{Ii}^{int,s} \tag{3.35}$$

The superscript '*s*' here represents the CB shell. A lump mass matrix is always required. The lump mass matrix can be obtained either by (1) the row sum technique or (2) physical lumping.

3.4 Matrices Assembly and Explicit algorithm

The discretized formulation of the CB beam, CB shell, and Lagrangian fluid are discussed in sections 3.1, 3.2, and 3.3. Since the thin structure and the Lagrangian fluid are viewed as one composite solid, it is necessary to assemble them in one unified discretized system. In mathematical practice, this is available by joining the individual matrices and rewriting them as a so-called global matrix. The assembly of the discretized system for the "composite solid" can then be expressed as,

$$M_{IJ}^{fs} a_{Ji}^{fs} = f_{Ii}^{ext,fs} - f_{Ii}^{int,fs} \tag{3.36}$$

An explicit time integration based on the central difference algorithm is employed to solve the transient dynamics of this nonlinear system from time step τ to $\tau+1$. Because the Cauchy stress is the primary stress measure that used for both CB beam and Lagrangian fluid, an updated Lagrangian frame is thus a natural and straightforward choice for solving this composite solid. Note that, when the internal nodal forces are determined by sequentially evaluating the strain-displacement equations, the Cauchy stress is calculated by the constitutive equations that are usually expressed in the form of ${}^{\tau}\mathbf{E}$ (or ${}^{\tau}\boldsymbol{\varepsilon}$) for the

CB beam and shell, and ${}^{\tau-1/2}\mathbf{D}$ for the Lagrangian fluid. The detailed algorithm is shown in Algorithm 1.

Algorithm 1: updL_ExDyna_Solver: Explicit dynamics analysis for updated composite solid.

---

(1) Getforce ${}^{\tau}f_{Ii} = {}^{\tau}f_{Ii}^{ext} - {}^{\tau}f_{Ii}^{int}$ at step τ

(2) Compute accelerations ${}^{\tau}a_{Ji} = M_{IJ}^{-1}\left({}^{\tau}f_{Ii} - C^{damp}\,{}^{\tau-1/2}v_{Ii}\right)$, C^{damp} is damping constant

(3) Time update: ${}^{\tau+1}t = {}^{\tau}t + {}^{\tau+1/2}\Delta t$, ${}^{\tau+1/2}t = \left({}^{\tau}t + {}^{\tau+1}t\right)/2$

(4) First partial update nodal velocities: ${}^{\tau+1/2}v_{Ii} = {}^{\tau}v_{Ii} + \left({}^{\tau+1/2}t - {}^{\tau}t\right){}^{\tau}a_{Ii}$

(5) Enforce velocity boundary conditions

(6) Update nodal displacements: ${}^{\tau+1}u_{Ii} = {}^{\tau+1}u_{Ii} + {}^{\tau+1/2}\Delta t\,{}^{\tau+1/2}v_{Ii}$

(7) Getforce ${}^{\tau+1}f_{Ii} = {}^{\tau+1}f_{Ii}^{ext} - {}^{\tau+1}f_{Ii}^{int}$ at step $\tau+1$

(8) Compute ${}^{\tau+1}a_{Ii}$

(9) Second partial update nodal velocities: ${}^{\tau+1}v_{Ii} = {}^{\tau+1/2}v_{Ii} + \left({}^{\tau+1}t - {}^{\tau+1/2}t\right){}^{\tau+1}a_{Ii}$, go back to step 1

The superscript '*fs*' is omitted for simplicity.

3.5 CBS method for Eulerian flows

For solving the Eulerian description of incompressible viscous fluid flow, i.e., solving the famous Navier-Stokes (N-S) equation, the Galerkin procedure based on the semi-implicit form of characteristic-based split (CBS) method is employed in this research [93, 94]. The conventional N-S equation in the Eulerian coordinate,

$$\frac{\partial V_i^f}{\partial t} + \frac{\partial}{\partial x_j^f}\left(v_i^f V_j^f\right) = -\frac{\partial p^f}{\partial x_i^f} + \frac{\partial \tau_{ij}{}^f}{\partial x_j^f} + \rho^f g_i \tag{3.37a}$$

$$\frac{\partial V_i^f}{\partial x_i^f} = -\frac{\partial \rho^f}{\partial t} \tag{3.37b}$$

where $V_i^f = \rho^f v_i^f$, $\tau_{ij}{}^f$ is the deviatoric stress $\tau_{ij}{}^f = 2\mu d_{ij}^{dev}$. In a standard FEM approach, the Eulerian fluid domain is discretized by a set of Eulerian meshes. The elemental fields of the fluid velocity and pressure are interpolated by the fluid nodes,

$$^{\tau}v_i^f = N_I \, ^{\tau}v_{Ii}^f \tag{3.38a}$$

$$^{\tau}p^f = N_I \, ^{\tau}p_I^f \tag{3.38b}$$

After spatial discretization of the N-S equation, a three steps scheme base on CBS time discretization can be adopted to compute the fluid velocity and pressure from time step τ to $\tau+1$.

Step 1: On the intermediate momentum calculation

$$\begin{aligned} M_{IJ}^f \frac{^{*}v_{Ji}^f - {}^{\tau}v_{Ji}^f}{\Delta t} &= -{}^{\tau}C_{IJ}^f \, {}^{\tau}v_{Ji}^f - {}^{\tau}F_{Ii}^f - \frac{\Delta t}{2} {}^{\tau}K_{IJ}^f \, {}^{\tau}v_{Ji}^f + {}^{\tau}f_{Ii}^{f,t} + {}^{\tau}f_{Ii}^{f,g} \\ &= {}^{*}RHS_{Ii}^f + {}^{\tau}f_{Ii}^{f,g} \end{aligned} \tag{3.39}$$

Step 2: On the pressure calculation

$$H_{IJ}^f \, ^{\tau+1}p_J^f = \frac{1}{\Delta t} Q_{IJi}^f \, ^{*}v_{Ji}^f \tag{3.40}$$

Step 3: On the momentum correction

$$M_{IJ}^f \frac{^{\tau+1}v_{Ji}^f - {}^{\tau}v_{Ji}^f}{\Delta t} = {}^{\tau+1}RHS_{Ii}^f = M_{IJ}^f \frac{^{*}v_{Ji}^f - {}^{\tau}v_{Ji}^f}{\Delta t} - G_{IJi}^f \, {}^{\tau}p_J^f \tag{3.41}$$

where

$$M_{IJ}^f = \int_{\Omega^f} \rho^f N_I^f N_J^f d\Omega, \qquad {}^{\tau}C_{IJ}^f = \int_{\Omega^f} \rho^f N_I^f \frac{\partial\left({}^{\tau}v_j^f N_J^f\right)}{\partial x_j^f} d\Omega$$

$${}^{\tau}F_{Ii}^f = \int_{\Omega^f} \rho^f \frac{\partial N_I^f}{\partial x_j^f} {}^{\tau}\tau_{ij}{}^f d\Omega, \quad {}^{\tau}K_{IJ}^f = \int_{\Omega^f} \rho^f \frac{\partial\left({}^{\tau}v_k^f N_I^f\right)}{\partial x_k^f} \frac{\partial\left({}^{\tau}v_j^f N_J^f\right)}{\partial x_j^f} d\Omega$$

$${}^{\tau}f_{Ii}^{f,t} = \int_{\Gamma^f} N_I^f {}^{\tau}\tau_{ij}{}^f n_j^f d\Gamma, \qquad {}^{\tau}f_{Ii}^{f,g} = \int_{\Omega^f} \rho^f N_I^f g_i d\Omega \tag{3.42}$$

$$H_{IJ}^f = \int_{\Omega^f} \rho^f \frac{\partial N_I^f}{\partial x_i^f} \frac{\partial N_J^f}{\partial x_i^f} d\Omega, \qquad Q_{IJi}^f = \int_{\Omega^f} \rho^f N_I^f \frac{\partial N_J^f}{\partial x_i^f} d\Omega$$

$$G_{IJi}^f = \int_{\Omega^f} N_I^f \frac{\partial N_J^f}{\partial x_i^f} d\Omega$$

The mass matrix M_{IJ}^f can be replaced by the lumped mass matrix for simplicity. The preconditioned conjugate gradient (PCG) scheme is employed to solve the Equation (3.30) in Step 2. The above semi-implicit CBS algorithm is conditionally stable, and the critical time step Δt is determined accordingly. The flowchart to calculate the incompressible viscous fluid flow from step τ to $\tau+1$ is given in Algorithm 2.

Algorithm 2. Fuild_CBS_solver: CBS for incompressible viscous fluid

---

(1) Given fluid velocity ${}^{\tau}v_{Ii}^f$, pressure ${}^{\tau}p_I^f$ and time step τ
(2) Compute immediate fluid velocity ${}^{*}v_{Ji}^f$ in Equation (3.29)
(3) Apply pressure boundary condition and solve for ${}^{\tau+1}p_I^f$ in Equation (3.30)
(4) Apply velocity boundary condition and compute fluid velocity ${}^{\tau+1}v_{Ji}^f$ in Equation (3.31)
(5) Update ${}^{\tau}v_{Ii}^f = {}^{\tau+1}v_{Ji}^f$, ${}^{\tau}p_I^f = {}^{\tau+1}p_I^f$, $\tau = \tau+1$; go back to step (2)

3.6 ELL Computational Algorithm

The governing equations of the proposed ELL method for FSI problems with bulk and thin solids are present in subchapter 2.2. The discretization and implementation of FEM for solving thin structures using the CB beam, CB shell theories, Lagrangian, and Eulerian fluid flow are given in the previous sections. The outline of the ELL algorithm is summarized and illustrated in Algorithm 3.

Algorithm 3: ELL algorithm for FSI problem

---

(1) Given the Eulerian fluid velocity ${}^{\tau}v_{Ii}^{f}$ and pressure ${}^{\tau}p_{I}^{f}$ at step τ; given Lagrangian mesh configuration (i.e. composite solid), ${}^{\tau}x_{Ii}^{fs}$ and velocity ${}^{\tau}v_{Ii}^{fs}$

(2) Verify whether the original wrapping Lagrangian fluid mesh distorts or not, if not distort; go to (a) else go to (b)

  (a) If not distort

    (2.a.1) Find composite solid nodes in the fluid elements to interpolate pressure, and compute FSI force ${}^{\tau}F_{Ii}^{FSI,s}$.

    (2.a.2) Impose velocity condition of moving boundary and call for **updL_ExDyna_Solver**

    (2.a.3) Update Lagrangian mesh position ${}^{\tau+1}x_{Ii}^{fs}$, and nodal velocity ${}^{\tau+1}v_{Ii}^{fs}$

  (b) If distort

    (2.b.1) Abandon the original Lagrangian fluid and include a new portion of the fluid; generate new Lagrangian fluid meshes and assemble the structure to form ${}^{\tau}x_{Ii}^{fs}$

    (2.b.2) Find Lagrangian nodes reside in Eulerian elements

    (2.b.3) Calculate Lagrangian nodal velocity and pressure from background Eulerian mesh, go to (2.a)

(3) Find Eulerian fluid nodes reside in Lagrangian elements; interpolate the velocities ${}^{\tau+1}\tilde{v}_{Ii}^{f}$ to the fictitious fluid nodes.

(4) Impose velocity condition computed in step (3) and Call for **Fluid_CBS_solver**; solve for the Eulerian fluid velocity ${}^{\tau+1}v_{Ii}^{f}$ and pressure ${}^{\tau+1}p_{I}^{f}$, go back to step (2) and continue the calculation

---

3.7 Re-meshing of the Lagrangian fluid

Since the constitutive law governs the warping Lagrangian fluid, it would undergo real deformation during the simulation. Therefore, this Lagrangian meshes of the fluid

would distort after several iterative steps, as discussed in the ELL algorithm. To suppress this problem, we can merely abandon the wrapping fluid at the previous time step and include another fluid portion that wraps the structure instantaneously. Nodal velocity and pressure value of the new portion can be easily achieved from the Eulerian background grids by FEM interpolation. An element can be determined as distorted if it meets some criteria; for example, the Jacobian J of the element is less than 0.2. Various re-meshing algorithms used in other CFD techniques, e.g., ALE and overset grid methods, can be adopted [95-98]. Re-meshing of the ELL is much easier due to the flexibility of the wrapping fluid.

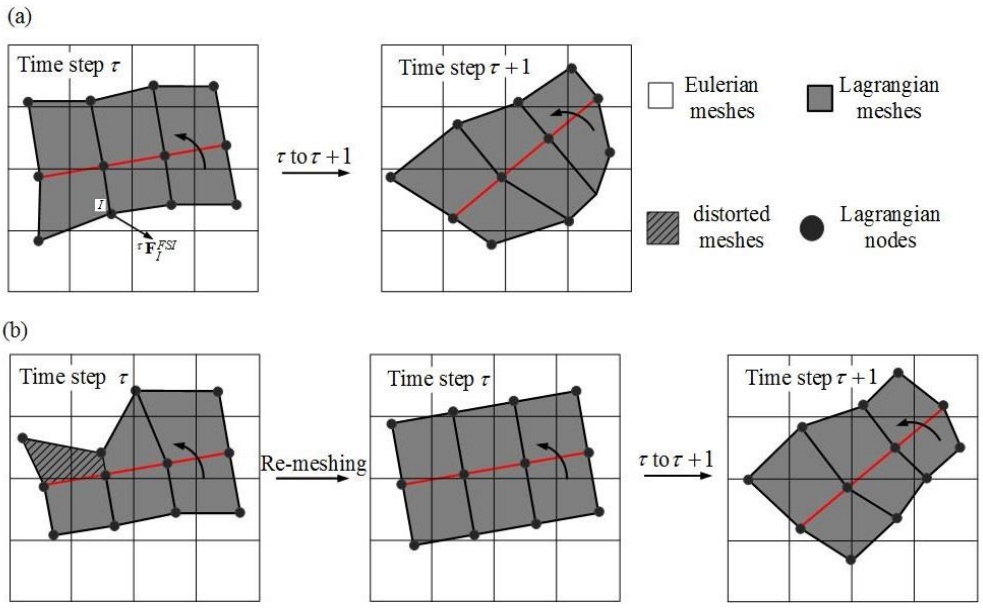

Figure 3.4: Illustrations of step (2) of ELL algorithm, calculation of Lagrangian fluid from time step τ to time step $\tau+1$ in case of (a) Lagrangian meshes do not distort; (b) Lagrangian meshes distort. The red line represents the moving body, for example, rotating counterclockwise.

For ELL with a rigid thin body, Figure 3.4 shows an easy way to generate the Lagrangian fluid meshes at the beginning and move them the same way as the rigid body

motion when the re-meshing process is needed. In our code implementation, it can be achieved by multiplying the coordinates of initial Lagrangian meshes by a set of translation and rotation matrices when re-meshing or reconstruction are needed.

For ELL with a flexible thin body, it can also achieve the new Lagrangian fluid meshes by constructing the elements with the help of the directors at nodes of the CB beam and CB shell, as illustrated in Figure 3.5 and Figure 3.6. Then the computation is continued.

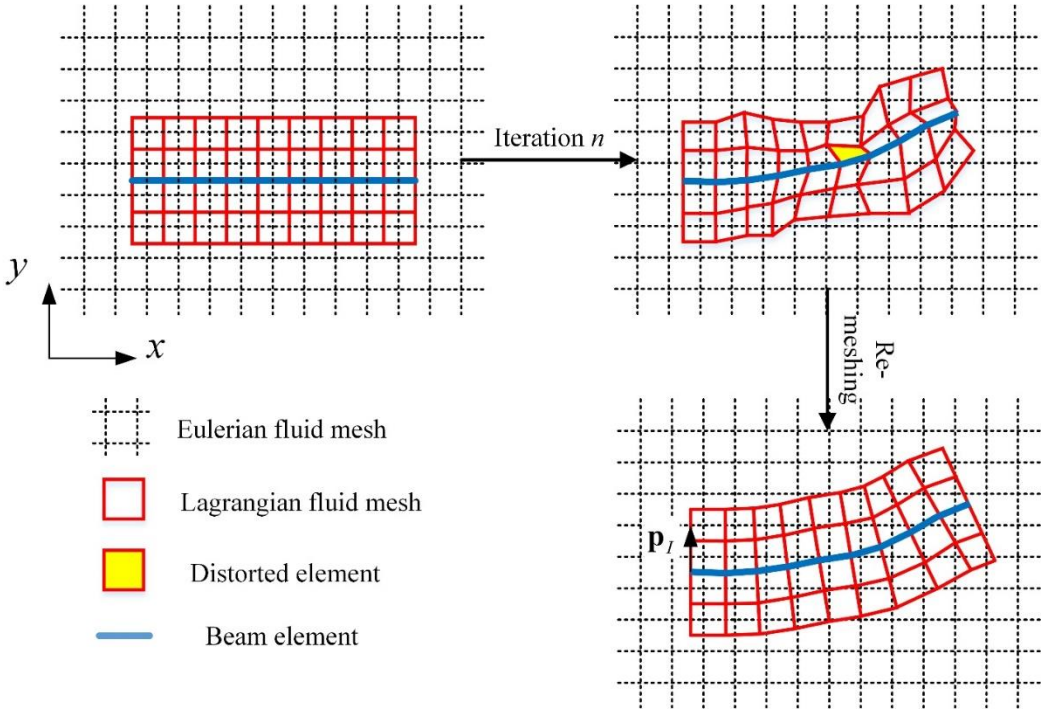

Figure 3.5: The illustration of the re-meshing scheme of ELL method with CB beam element

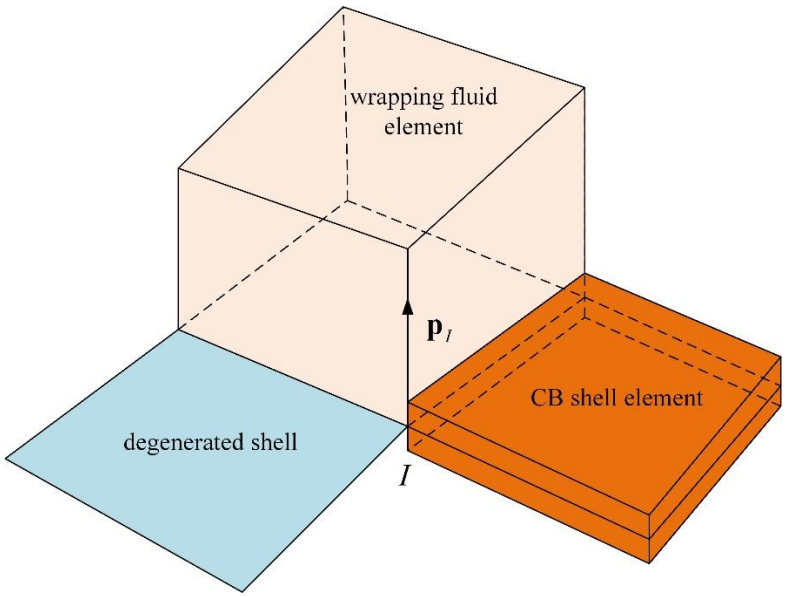

Figure 3.6: The re-meshing of the wrapping fluid element in ELL with CB shell element

CHAPTER 4. NUMERICAL EXAMPLES FOR ELL WITH BULK SOLIDS

In this chapter, three numerical examples with bulk solids immersed in the fluid are calculated to show the superiority of the proposed ELL method in comparison to the conventional IFEM. ELL improves the accuracy of the solution and has excellent performance even in a coarse mesh planning.

4.1 Rotating ring in the square fluid

This numerical example studies a 2D FSI problem of a rotating solid ring immersed in a square fluid domain. Figure 4.1 shows the geometry of the problem. The interior and exterior radii of the ring are $r = 25$ cm and $R = 30$ cm, respectively. The length of the fluid domain is $L = 1$ m. The center of the ring coincides with the center of the fluid field. The ring is considered as a rigid body rotating with a constant angular velocity $\omega^s = 2\,\mathrm{rad/s}$. The density of the fluid is $\rho^f = 1\,\mathrm{kg/m}$, and the dynamic viscosity of the fluid is $\mu^f = 10\,\mathrm{kg/(m\cdot s)}$. Nonslip boundary conditions are imposed on the interior, and exterior surfaces of the ring and nonslip boundary conditions are also assumed at the four edges of the fluid domain. The zero pressure boundary condition is at the center of the circle. No gravity effect is considered. The fluid and solid are initially assumed to be at rest; the ring begins to rotate when the simulation starts. The rotation of the ring induces the fluid flow in the square fluid domain. The simulation is determined to reach a steady-state when $ef \le 1e-6$, where velocity residual ef is defined as

$$ef = \left\| v^{\tau+1} - v^{\tau} \right\| / \left\| v^{\tau} \right\| \tag{4.1}$$

where $\|\bullet\|$ is L2-norm.

At steady state, the fluid inside the ring would rotate with an angular velocity $\omega^f = 2$ rad/s about the center of the ring as the flow remains laminar. The flow outside the ring should achieve a maximum speed at the exterior surface of the ring and decrease to zero on the wall boundaries, as reported in [61].

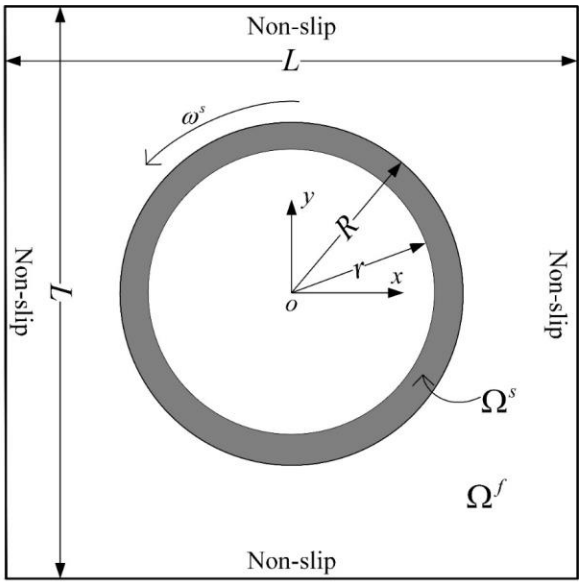

Figure 4.1: The geometry of a rotating ring in the square fluid domain.

Both the IFEM and ELL methods are used to calculate this example. Figure 4.2 shows the meshing plans for IFEM and ELL. Different from IFEM, one layer of the Lagrangian fluid wrap the ring to implement the ELL method. In both approaches, the Eulerian fluid domain is discretized by 20×20 uniform Q4 (quadrilateral with four nodes) elements with size $h^{Ef} = 1/20$ m. The element sizes of the solid and the composite solid

are the same as the Eulerian fluid $h^s \cong h^{cs} \cong h^{Ef}$. Theoretically, the velocity of the fluid node 'A', attached to the top of the exterior surface of the ring, should have the same as the solid point at that location, which is a constant velocity, e.g., $\left|v_A^f\right| = \left|v_A^s\right| = 0.6$ m/s. However, the arbitrary discretization of the fluid and solid domain cannot guarantee a shared node at this point.

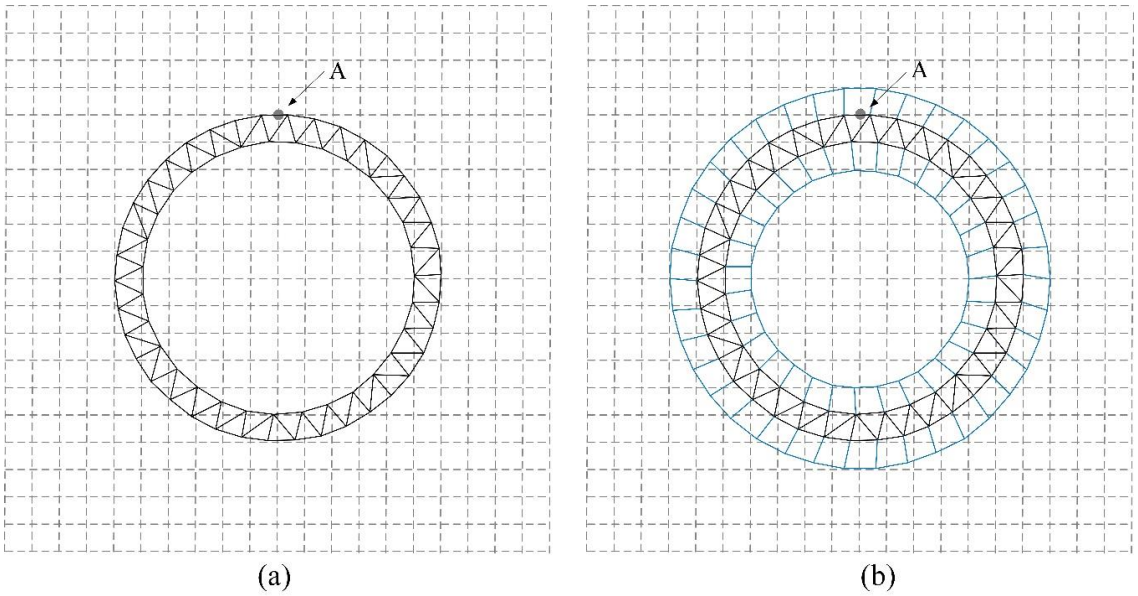

Figure 4.2: The meshing schemes of a rotating ring in the square fluid based on (a) the IFEM method and (b) the ELL method. The uniform squares at the background are Eulerian fluid meshes, the solid triangles are solid meshes, and the blue quadrangles are the wrapping Lagrangian fluid meshes.

The fluid node 'A' is outside of the solid domain; therefore, the velocity condition on the solid boundary cannot be smoothly transferred to the fluid nodes nearby when using the IFEM approach. The velocity contour of the fluid at the steady-state solved by the IFEM is shown in Figure 4.3 (a). Although the solution converges, the inaccurate solid boundary shape results in an erroneous fluid pattern. The velocity at fluid node 'A' is 0.44 m/s, which has a relative error of 26.67%. For the ELL method, point 'A' is covered by the

composite solid mesh. The velocity field is now smoothly transferred from solid to fluid. The velocity contour of the fluid solved by the ELL method is shown in Figure 4.3 (b). The results are improved even with such a coarse mesh scheme. The velocity at fluid node 'A' is 0.59 m/s, which is 98.33% accurate.

To investigate the spatial convergence property of the ELL method, we use four meshing sets for the Eulerian fluid. MS (1), $h^{Ef} = 1/20\,\mathrm{m}$; MS (2), $h^{Ef} = 1/40\,\mathrm{m}$; MS (3), $h^{Ef} = 1/80\,\mathrm{m}$ and MS (4) $h^{Ef} = 1/160\,\mathrm{m}$. For each set, the element size of the solid ring is the same as the Eulerian fluid, and one layer of the Lagrangian fluid meshes attaches to the interior and exterior surfaces of the ring. The streamlines of the fluid flow for MS (3) at the steady-state is shown in Figure 4.4, which is the same as in [61]. In the plot, the fluid inside the ring has a laminar fluid flow and rotates like a solid body. Thus it is ideal for measuring the relative fluid velocity error, i.e. $e_v^f = \left\| \mathbf{v}^f - \mathbf{v}_r^f \right\|_{L2} \Big/ \left\| \mathbf{v}_r^f \right\|_{L2}$, where $\mathbf{v}_r^f$ is the reference nodal fluid velocity inside the ring. The spatial convergence rates of the ELL and IFEM methods are illustrated in Figure 4.5. The theoretical convergence rate of the second order is also plotted for reference. Both methods have a second-order convergence rate. The relative error given by the ELL method based on the MS(2) meshing is smaller than the IFEM method based on the MS(4). The efficiency and accuracy of the numerical solutions of the rotating ring are largely improved by the ELL method.

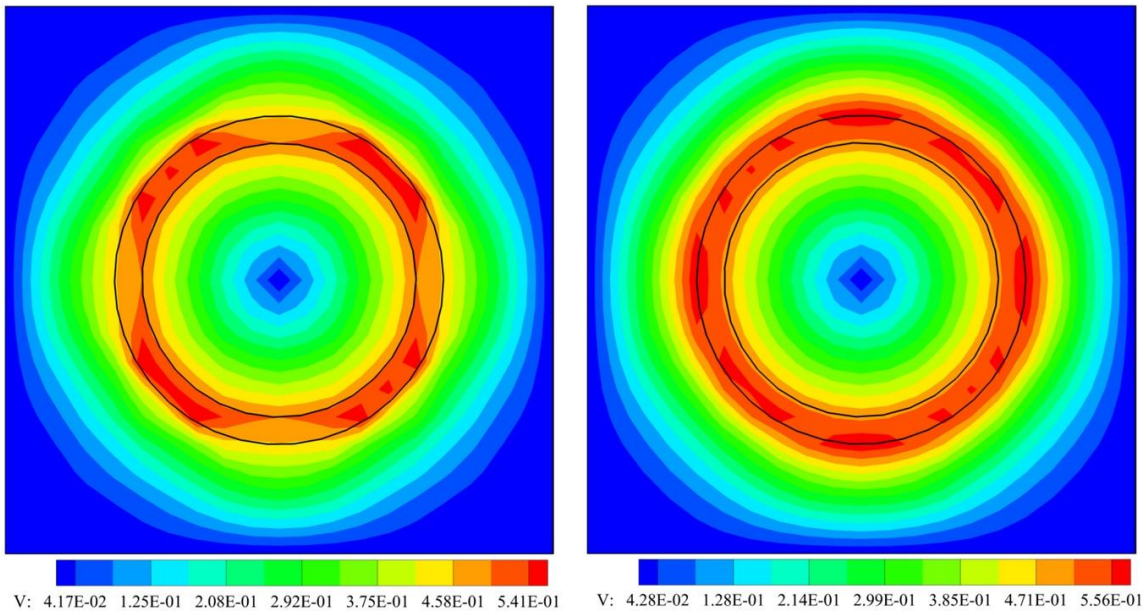

Figure 4.3: Contours of fluid velocity solved by (a) IFEM, (b) ELL using element size of 1/20 m.

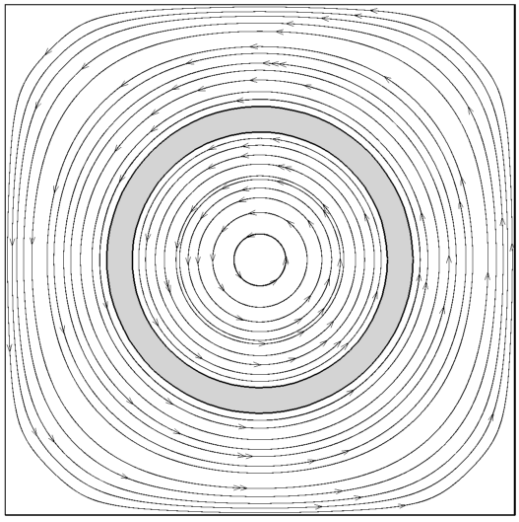

Figure 4.4: Streamlines of the solid ring rotating in a square fluid solved by MS(3).

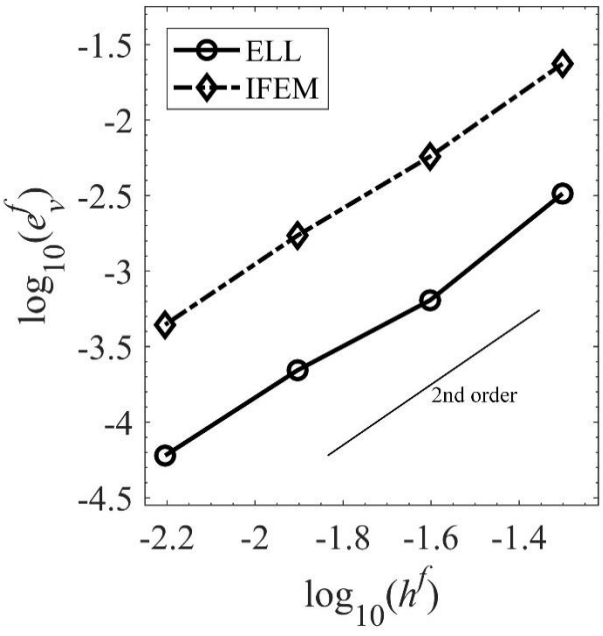

Figure 4.5: Spatial convergence rates of the ELL and IFEM methods.

4.2 2D flapping wing

A more complex FSI problem of a flapping wing interacting with the fluid is calculated. This example has been reported using IBM and its variants, such as in references [99-101]. The cross-section of this 2D flapping wing is modeled as an ellipse with a large aspect ratio of 10, as shown in Figure 4.6 (a). The length of the elliptical wing is c, and the computational fluid domain is $20c \times 20c$. The wing is translating in a sinusoidal movement in the horizontal direction and rotating about the centroid simultaneously. The prescribed sinusoidal translation and rotational motions are given by,

$$x(t) = \frac{A_m}{2}\cos(2\pi ft), \quad y(t) = 0 \tag{4.2a}$$

$$\theta(t) = \frac{\pi}{4}\sin(2\pi ft) + \theta_0 \tag{4.2b}$$

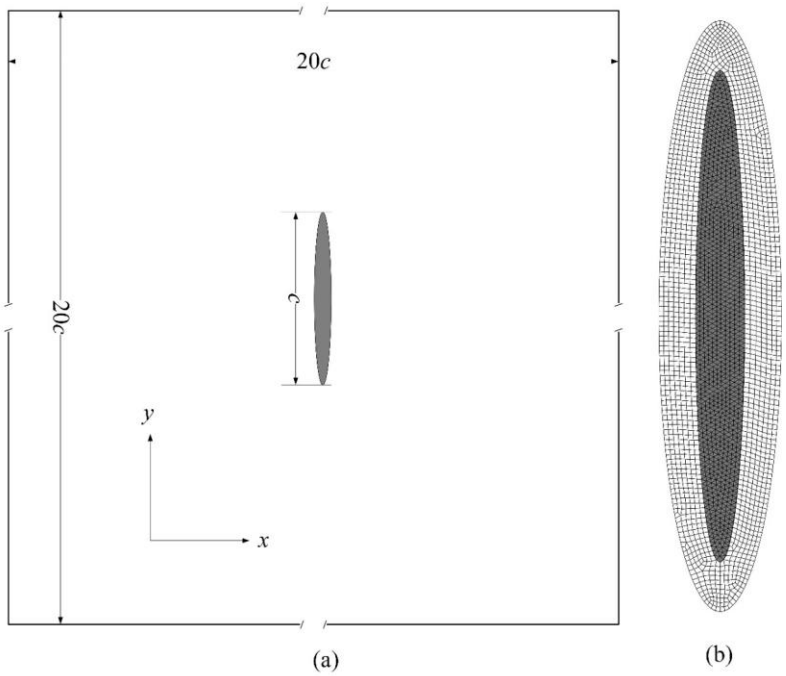

Figure 4.6: (a) The geometry of the 2D flapping wing model. (b) The meshes for the elliptical wing and the wrapping fluid around the wing.

The rotating angle θ is measured counterclockwise relative to the positive x-axis. The corresponding constants for this numerical example are $A_m = 2.8c$, $f = 0.25$ Hz and $\theta_0 = \pi/2$ to replicate the results in [100]. The Reynolds number is defined as $\mathrm{Re} = \rho^f U_\infty c/\mu^f$ and is set to 75, where U_∞ is the maximum translation velocity of the wing centroid, that is $\pi f A_m$. Both the IFEM and ELL calculate the example. For the ELL method, an additional small portion of the fluid is included to transfer the velocity from the solid to the fluid smoothly. Figure 4.6 (b) shows the discretized model of the wrapping fluid and solid with the element size of $0.01c$. The total number of the 1,800 T3 (triangle with three nodes) elements are used for the 2D elliptical wing and 1654 Q4 elements for the wrapping fluid. For the background Eulerian domain, two meshing sets are used with

the total number of MS (1) 52,908 and MS (2) 144,048 Q4 elements. The refined element sizes in the FSI zone are $h^{Ef} = c/40$ for MS (1) and $h^{Ef} = c/80$ MS (2). Pressure outlet boundary conditions are specified for all outer boundaries.

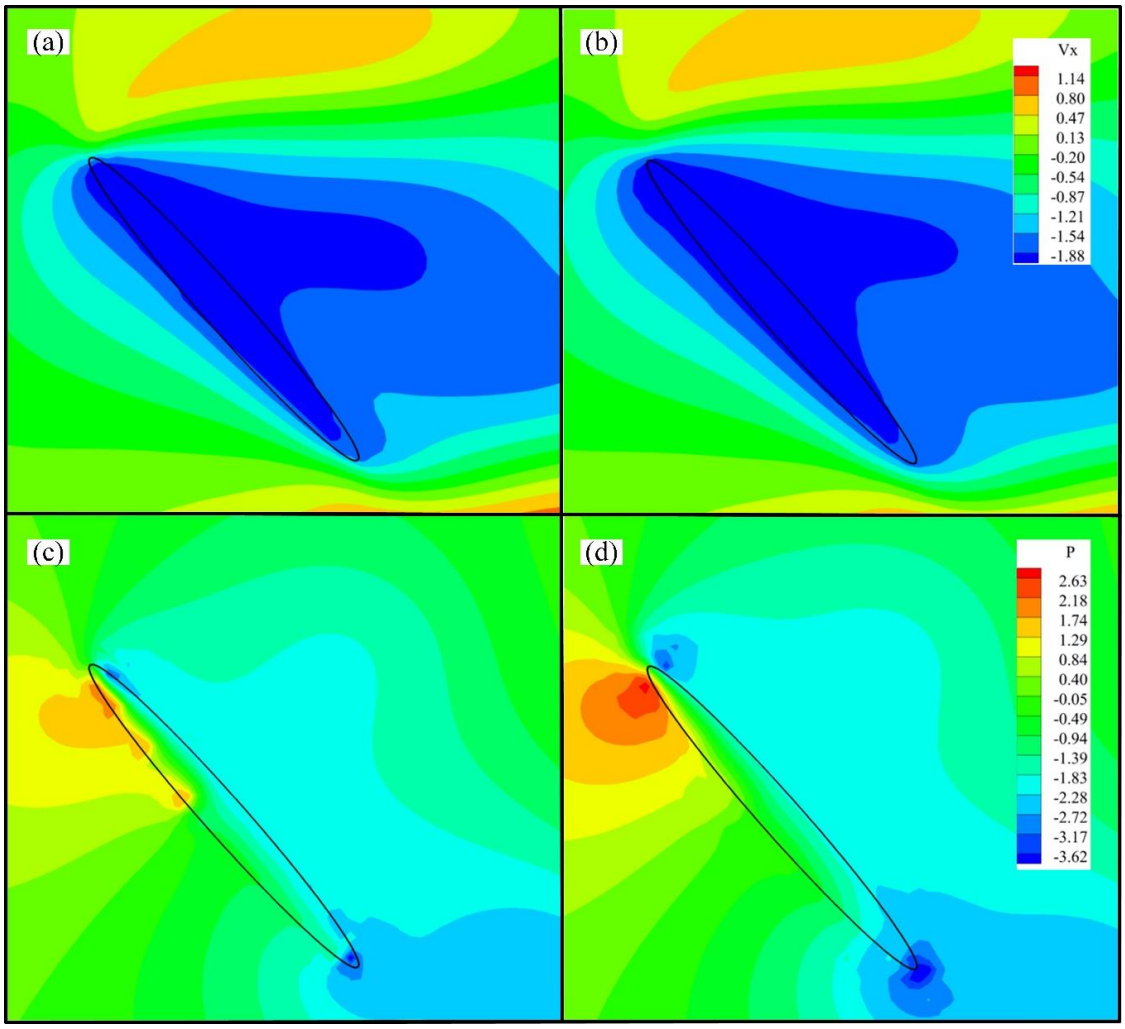

Figure 4.7: (a) The contour plots of the horizontal velocity solved by (a) the IFEM method and (b) the ELL method. The contour plots of the pressure solved by (c) the IFEM and (d) The ELL method. All the cases are resolved using Eulerian mesh MS(1) and at the instance of 1.1875*T*.

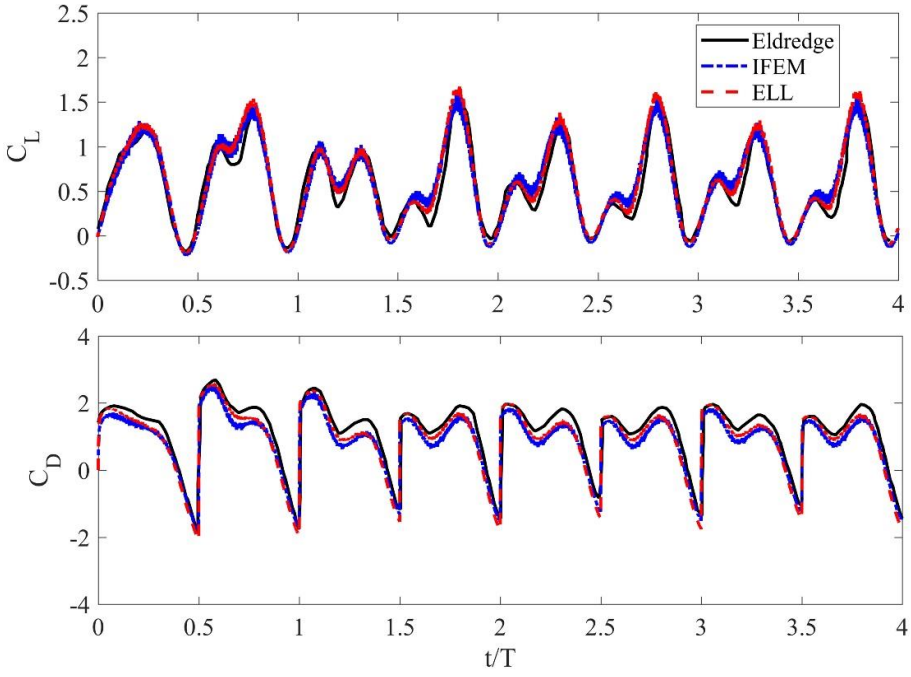

Figure 4.8: The lift/drag coefficients of the 2D flapping wing in four complete cycles using the Eulerian meshing scheme MS(2).

Since the coarser Eulerian fluid meshes are used in MS (1), the effect of the inaccurate interface in the fluid using IFEM would be more notable. Figure 4.7 shows the comparison of the horizontal velocity and pressure of the fluid using the IFEM method and the ELL method based on the MS (1). The time instance is $1.1875T$, where T is the time of one period. The wing is translating towards negative x-axis while rotating counterclockwise. Thus the tip at the leading edge of the wing would have the minimum horizontal velocity. The fluid attached to the tip should also have the same horizontal velocity. However, as shown in Figure 4.7 (a), the fluid field in the vicinity of the tip has a more significant horizontal velocity as if fluid penetrates the solid. Such penetration is due to the inaccurate description of the solid shape that makes the real solid domain smaller, thus reducing its impact on the fluid. The ELL approach can effectively remedy the discrepancy of the FSI interface in the fluid grids. As shown in Figure 4.7 (b), the velocity

at the FSI interface is now smoothly transferred to the fluid. No fluid particles penetrate the solid body. The inaccurate description of the solid shape also causes the undesirable pressure distribution of the IFEM, as shown in Figure 4.7 (c). Furthermore, this undesirable pressure distribution is improved by the ELL method, as shown in Figure 4.7 (d).

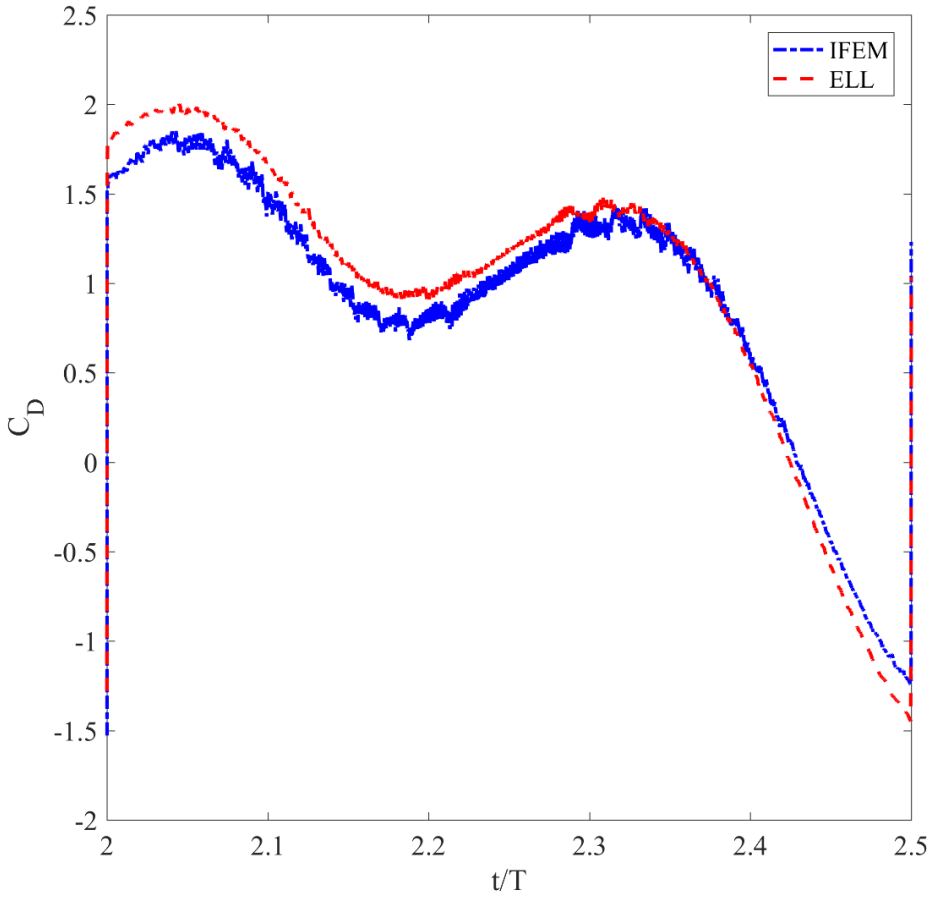

Figure 4.9: The zoom-in plot of the drag coefficients from 2*T* to 2.5*T*

Figure 4.8 shows the comparison between the lift/drag force coefficients obtained by the IFEM and ELL methods using MS (2) within four complete cycles, the results in [100] is also presented. The lift force is defined as the vertical component of the resultant force applied on the wing, i.e. $F_L = F_y$. The drag force is established as the horizontal force opposing the translation movement, that is $F_D = -sign(U)F_x$, where U is the horizontal

velocity at the centroid of the elliptical wing. The lift/drag coefficients are given by $C_L = 2F_L / \rho^f U_\infty^2 c$ and $C_D = 2F_D / \rho^f U_\infty^2 c$ respectively. The results from both methods have good agreements compared with the reference shown in Figure 4.8. The curves of the drag coefficient from $2T$ and $2.5T$ are amplified and plotted in Figure 4.9. The IFEM method provides a more wavy result of the force over time due to the blurred boundary of the solid body, while the ELL method has a more smooth drag coefficient curve. The vorticity contours at different time instants from the second cycle to the fourth cycle are shown in Figure 4.10. The flapping wing induces the vortices at the leading and trailing edges. A sequence of the vortex pairs is formed due to the detaching and shedding of the vortices at the trailing edge. These flow structures are quite identical to the results in [100].

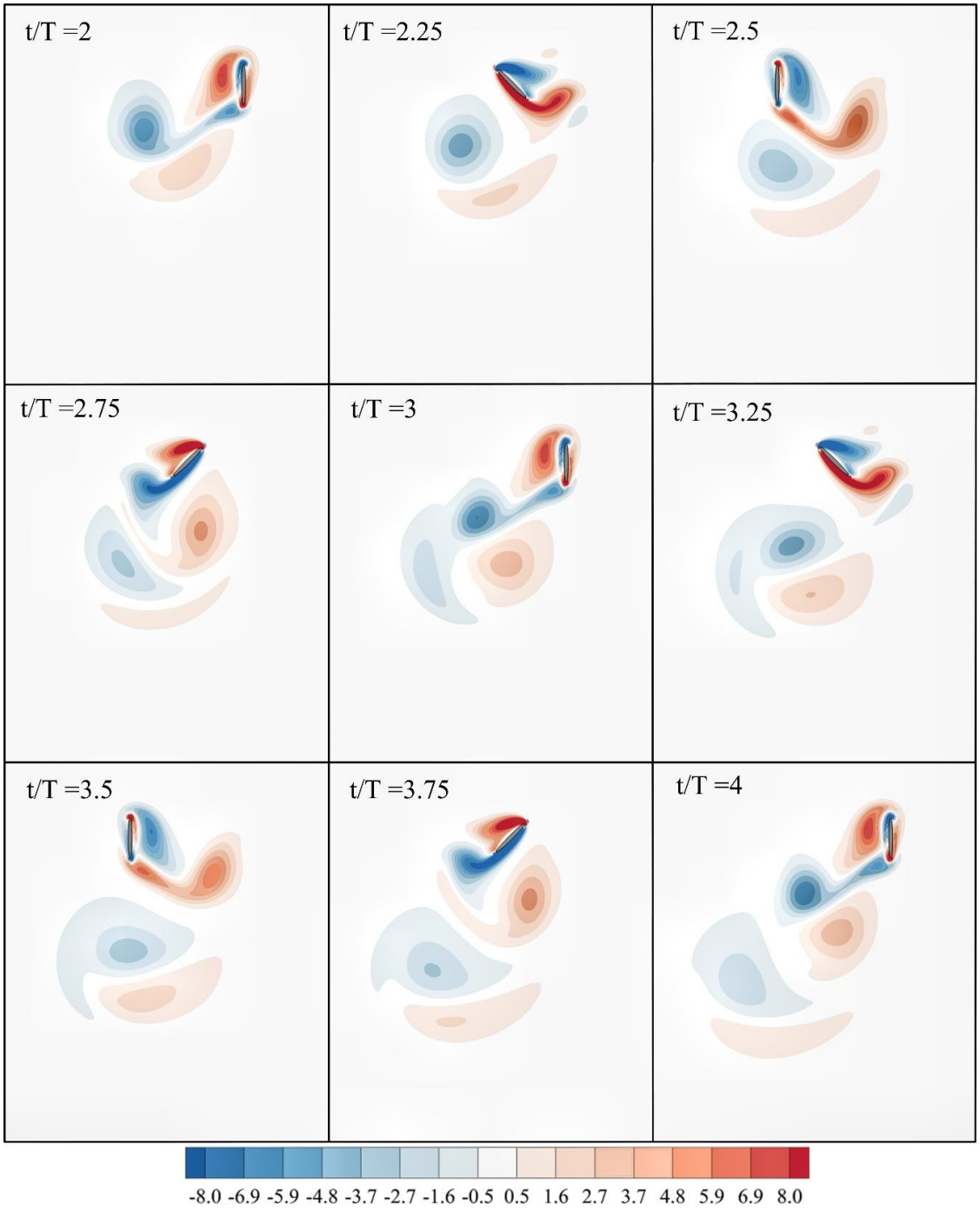

Figure 4.10: Vorticity field contours for different instants for the 2D flapping wing movement.

4.3 Vertical beam in the fluid tunnel

In this example, we studied the bending of a flexible beam in the fluid tunnel. Figure 4.11 illustrates the schematic of the problem; the beam is standing vertically with the incoming flow from the horizontal direction. The width of the beam is a = 0.04 cm, and the height is b = 0.8 cm. The Saint Venant–Kirchhoff material is considered for the beam, and it is fixed at the bottom. The density of the beam is ρ^s=7.8 g / cm^3, Young's modulus $E = 10^5\ \mathrm{g}/\left(\mathrm{cm}\cdot\mathrm{s}^2\right)$ and Poisson's ratio $\upsilon = 0.3$. Gravity and damping are not considered in this case. The length of the tunnel is L = 4 cm, and the height H = 1 cm. The bottom edge of the fluid domain is applied with nonslip boundary conditions v_x^f, $v_y^f = 0$. The symmetric condition is assumed, i.e. $v_y^f = 0$, at the top edge. The left edge defines the velocity inlet with a parabolic velocity profile $v_x^f = 1.5\left(-y^2 + 2y\right)\mathrm{cm/s}$ and $v_y^f = 0$. The pressure outlet is at the right edge, with the reference pressure set as p = 0. The fluid density is $\rho^f = 1.0\ \mathrm{g/cm}^3$, and the dynamic viscosity is $\mu = 0.1\ \mathrm{g}/\left(\mathrm{cm}\cdot\mathrm{s}\right)$. The system stays at rest in the initial state.

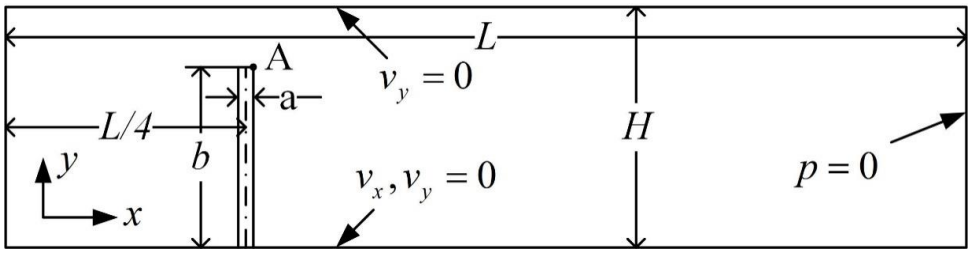

Figure 4.11: The problem geometry of the flow passing a vertical beam.

We use 4,894 nodes for the Eulerian fluid, 124 nodes for the beam in MS (1), with element sizes in FSI zone $\Delta h^{Ef} = \Delta h^{s} = a/2$; 16,354 nodes for the Eulerian fluid, 407 nodes for the beam in MS (2), with element sizes in FSI zone $\Delta h^{Ef} = \Delta h^{s} = a/4$; 38,596 nodes for the Eulerian fluid, 1,453 nodes for the beam in MS(3), with element sizes in FSI zone $\Delta h^{Ef} = \Delta h^{s} = a/8$. In each scenario, two lawyers of the Lagrangian fluid are used for implementing the ELL approach.

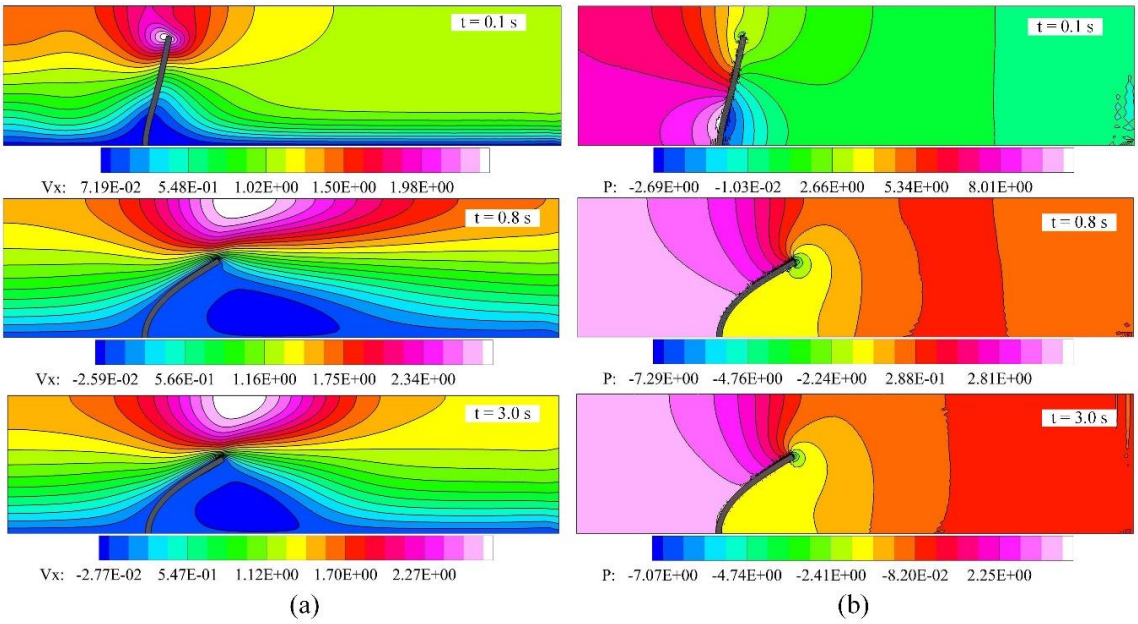

Figure 4.12: (a) The horizontal velocity contour (b) the pressure contour of the flow passing a vertical beam in three different time instances; solved by MS(2).

With the inlet flow coming in, the beam would eventually bend with significant deformation. A nozzle is formed between the top of the beam and the top edge of the tunnel that the liquid passes through with increasing speed. Figure 4.12 shows the contour plots of the horizontal velocity and pressure at different time instances. These results are the same as provided in [61]. The histories of the velocity component and the displacement

measured at the tip 'A' of the beam are plotted in Figure 4.13. The results solved by IFEM based on the MS (3) are also plotted. Theoretically, the FSI interface in IFEM is only implicitly represented by the fluid nodes close to and inside the solid surface. Therefore, the impact of the solid domain on the fluid would be weakened. As indicated by the streamlines in Figure 4.14, the beam completely blocks the fluid in the ELL solution. Whereas, in the IFEM solution, the liquids near the interface would penetrate through the solid. Thus only requiring a smaller opening of the nozzle, and resulting in smaller bending magnitude.

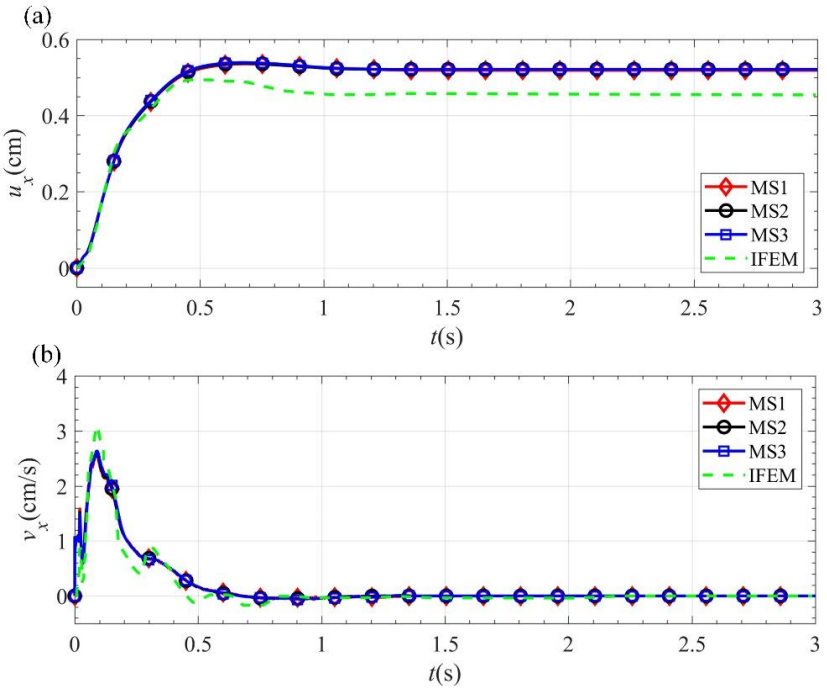

Figure 4.13: Time history of the (a) horizontal displacement and (b) horizontal velocity of the flow passing a vertical beam in three seconds.

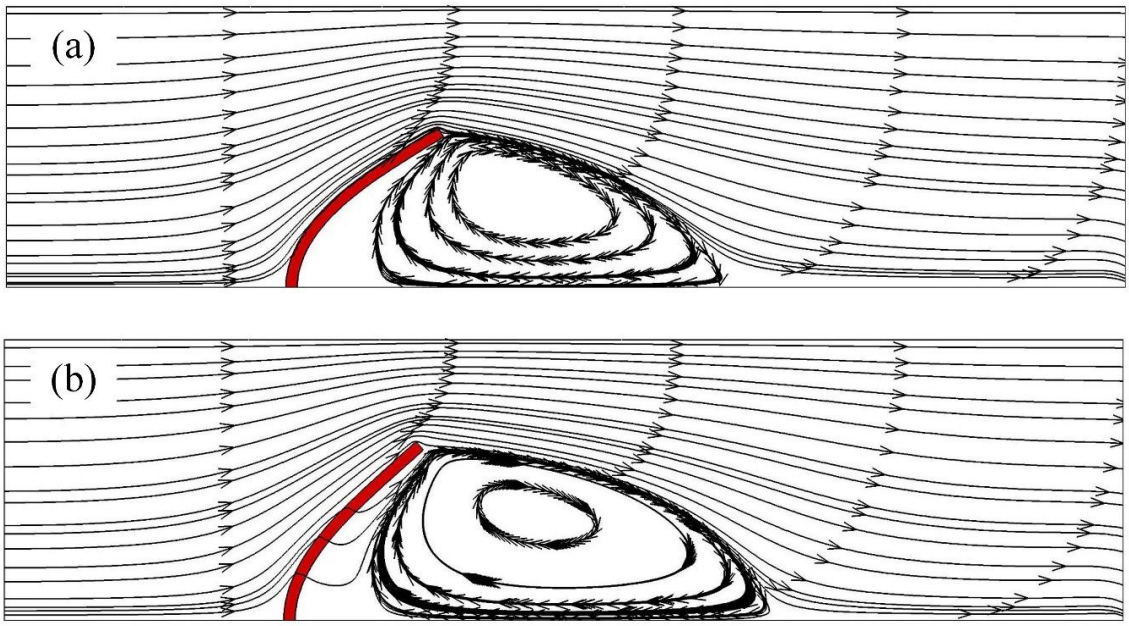

Figure 4.14: The streamlines at the final times step solved by (a) the ELL method and (b) the IFEM method using MS (3).

In contrast, the FSI interface, in the ELL approach, can be accurately described at the composite solid domain, and then smoothly spread onto the fluid nodes nearby. For both methods, the finer grid provides larger deformation. Table 4.1 presents the comparison of the horizontal displacement after three seconds using both methods. The beam deforms more significantly even when using a coarse meshing scenario in ELL than the most excellent meshing in the IFEM. Reference [61] reported that the system tends to have a steady-state, which is determined as ef < 1e-8, after three seconds using IS-FEM solver. The convergence time for IFEM and ELL are recorded in Table 4.1. For the coarse meshing sets, such as MS (1) and MS (2), the simulations cannot converge even after 10 s using IFEM. The beam is oscillating due to the inadequate interpretation of the FSI interface. A small location change of the solid meshes would lead to a re-evaluation of the FSI interface

in implementing the Eulerian fluid solver. ELL method can always obtain convergent solutions with different meshing sets.

Table 4.1. The comparison of the horizontal displacement at three seconds and convergence time of IFEM and ELL for solving example 4.3.

Meshing Scheme	Horizontal displacement (cm)		Convergence time (s)	
	IFEM	ELL	IFEM	ELL
MS(1)	0.4452	0.5186	-	2.9
MS(2)	0.4592	0.5213	-	2.7
MS(3)	0.4648	0.5225	3.1	2.7

CHAPTER 5. 2D NUMERICAL EXAMPLES FOR ELL WITH THIN STRUCTURES

In this chapter, numerical examples of ELL for solving 2D FSI problems with thin solid bodies are calculated. We first study the FSI problems with rigid bodies moving in the fluid. The method is well validated. Then, the CB beam element is adopted for implementing ELL for solving 2D FSI problems with thin flexible structures.

5.1 2D rigid

5.1.1 Rotating thin ring in a square fluid domain

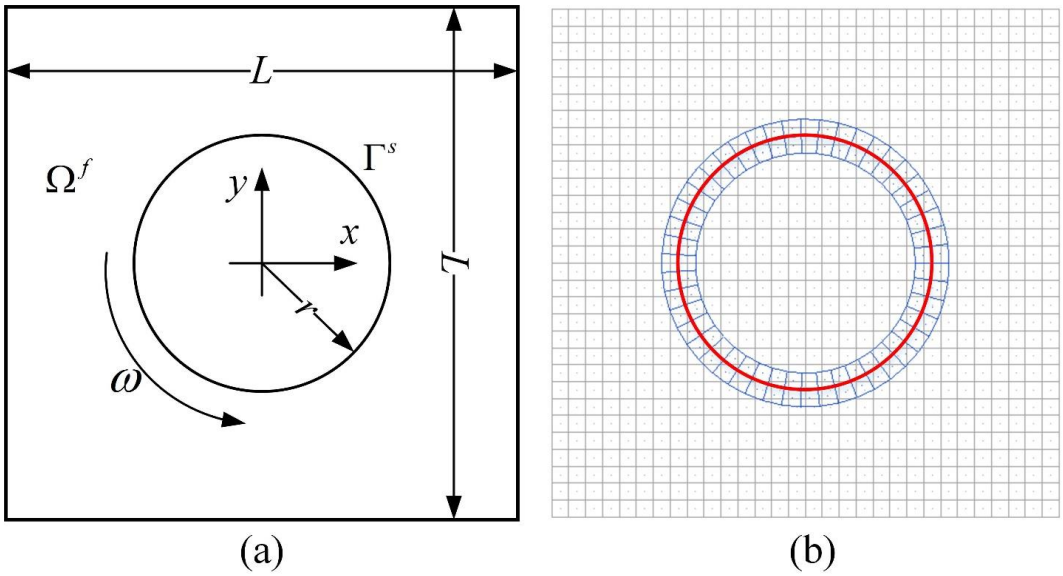

Figure 5.1: (a) Geometry and (b) meshing plan of the rotating thin ring in a square fluid domain.

In this example, we re-calculate the case of the rotating ring in section 4.1, but with zero thickness, as illustrated in Figure 5.1 (a). The radius of the ring is $r = 25\,\text{cm}$. All the other setups are the same as in example 4.1.

To implement the ELL method with a thin structure, we include a small portion of the fluid to wrap the ring. Two layers of the Lagrangian fluid mesh (one layer on each side) are generated, as shown in Figure 5.1 (b). The ratio of the Eulerian and Lagrangian fluid mesh size is $h^{Ef}/h^{Lf} \cong 1$. Four sets of the Eulerian and Lagrangian fluid meshes are employed in terms of the size of Eulerian fluid mesh: MS (1), $h^{Ef} = 1/30\,\mathrm{m}$; MS (2), $h^{Ef} = 1/60\,\mathrm{m}$; MS (3), $h^{Ef} = 1/120\,\mathrm{m}$; MS (4), $h^{Ef} = 1/240\,\mathrm{m}$. Figure 5.2 (a) and Figure 5.2 (b) show the contour of fluid velocity and streamlines of the fluid flow for mesh MS (3) when the system reaches the steady-state. The velocity vector field of the fluid domain for mesh MS (1) is shown in Figure 5.2 (c). Laminar fluid flow can be observed inside the ring from these plots. The spatial convergence property is illustrated in Figure 5.2 (d). The spatial convergence rate is 1.7665, which is also close to the theoretical convergence rate of 2.0.

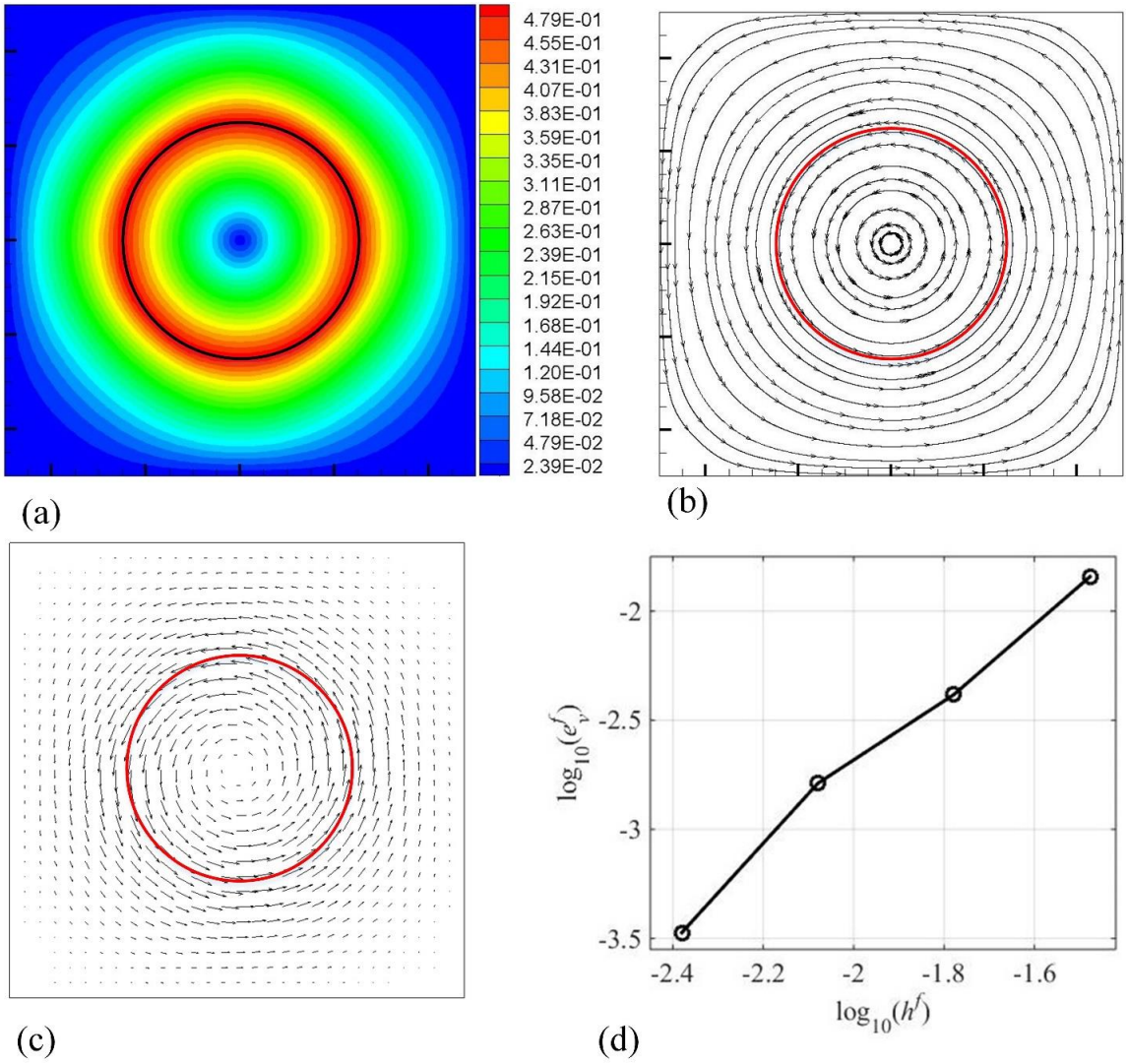

Figure 5.2: (a) The contour plot of the amplitude of the fluid velocity solved using MS (3); (b) streamlines of the fluid domain solved by MS (3); (c) velocity vector field of the fluid domain by MS (1); (d) spatial convergence properties of the fluid velocity.

5.1.2 Flow over a hollow cylinder

Laminar flow over a hollow cylinder with no thickness placed asymmetrically inside a tunnel is studied here. The diameter of the cylinder is $D = 0.15\,\mathrm{m}$, and the distances from the center of the cylinder to the upper and lower walls are 2.1D and 2.0D, respectively, as shown in Figure 5.3 (a). A total number of 15,995 nodes and 15,698

elements are used for the fluid domain. In order to implement the ELL method, we need to include a small portion of the Lagrangian fluid to wrap the circle. Figure 5.3 (b) shows a close-up image of a ring with an inner radius of 0.06 m and an outer radius of 0.09 m. The red circle in the middle represents the cylinder. The total number of nodes and elements for the Lagrangian fluid are 760 and 658, respectively.

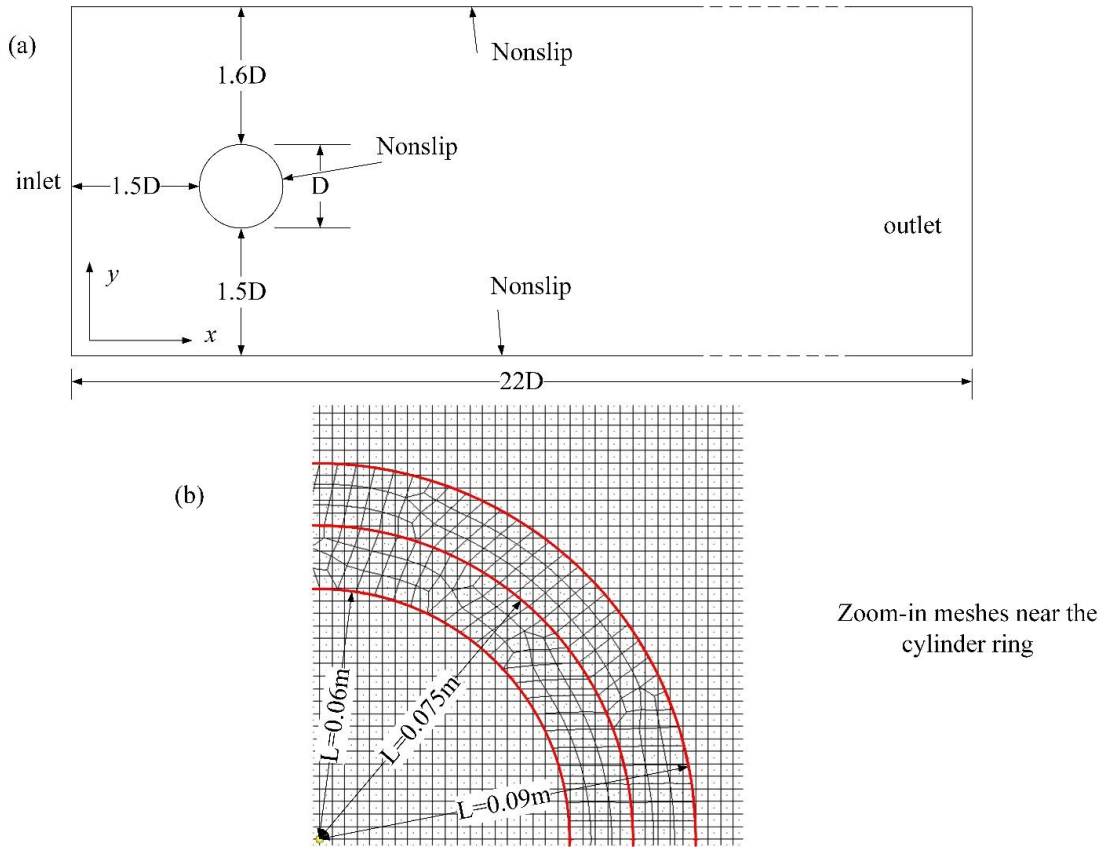

Figure 5.3: (a) Model of 2D flow over asymmetrically-placed cylinder; (b) zoom-in Lagrangian fluid meshes warp the thin structure.

A parabolic velocity profile of maximum speed $v_x^{\max} = 1\text{m/s}$ in the *x*-direction is assigned to the inlet. The upper and lower walls are assumed as nonslip boundaries where $v_x = 0, v_y = 0$. The pressure condition $p = 0$ is enforced on the outlet. In this case, since the

cylinder is static, the nonslip velocity boundary condition is also applied to the nodes of the middle circle.

The density of the fluid is ρ=1 kg/m^3 , and the dynamic viscosity is μ=0.001 Ns/m^2 . The Reynolds number, based on the average inlet velocity, is defined as $\mathrm{Re} = \rho v_x^{avg} D/\mu$, with $v_x^{avg} = 2/3\, v_x^{\max}$, i.e., Re = 100 in this case. The flow becomes unsteady at Re = 100, and a periodic vortex shedding can be observed. Figure 5.4 shows the vorticity and velocity of a single instant time, which are similar to in [41].

The drag and lift coefficients are defined as

$$C_D = \frac{F_D}{\frac{1}{2}\rho\left(v_x^{avg}\right)^2 D} \tag{5.1}$$

$$C_L = \frac{F_L}{\frac{1}{2}\rho\left(v_x^{avg}\right)^2 D} \tag{5.2}$$

where F_D and F_L are the sum of the applied external force in the *x* and *y*-direction, respectively. The variations of lift and drag coefficients are presented in the Figure 5.5. The effects of the slightly asymmetric geometry can be captured by the slightly non-symmetric drag coefficient in this method. The same results are in [41]. The maximum lift coefficient $C_{L,\max}$ in this method is 0.95, which is 4.04%~5.91% below the results from references [41, 102], and the maximum drag coefficient $C_{D,\max}$ is 3.248 that has negligible error compared with the references' 3.22~3.255. The Strouhal number (defined as $St = Df_q/v_{avg}$, where f_q is shedding frequency) is 0.295, which agrees well with Strouhal number (0.295~0.305) in references. The inclusion of the Lagrangian fluid meshes and the

transfer of FSI conditions also require additional computational effort. To evaluate this effort, this case is simulated by using only FEM with the same amount of Eulerian meshes. In one time step, the average CPU times for the ELL and FEM are 0.255 s and 0.221 s. The additional CPU cost is 0.034 s, due to the wrapping Lagrangian fluid to transfer FSI conditions. That only accounts for approximately 15% extra computational work.

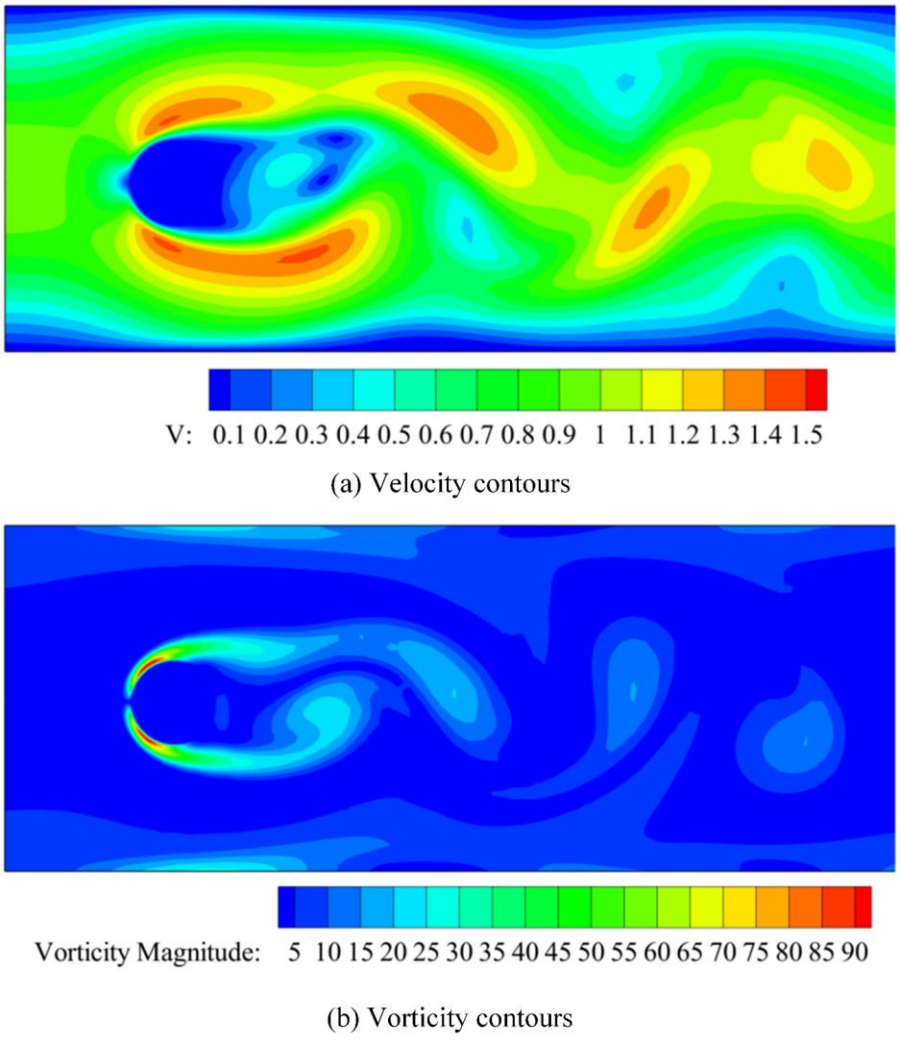

Figure 5.4: Instantaneous (a) velocity and (b) vorticity contours of flow over a cylinder.

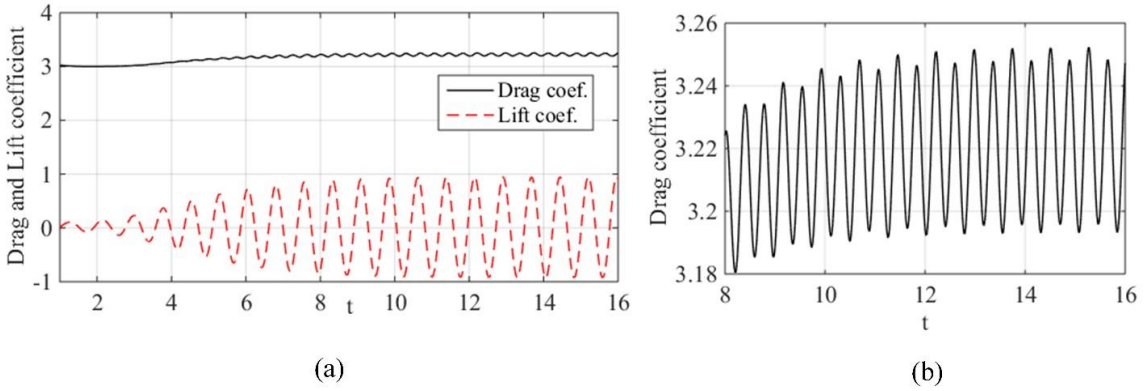

Figure 5.5: Time evolution of (a) drag and lift coefficients and (b) zoom-in drag coefficient for Re = 100.

5.1.3 2D flapping wing

To further explore the capability of the ELL method for computing a thin rigid body moving in the fluid, the flow over a flapping wing is calculated in this numerical example. This example has been thoroughly studied in example 4.2. Instead of using an elliptical wing, we can also use a rod with no thickness to represent the 2D wing, as shown in Figure 5.6 (a). The length of the rod is *c*.

The total number of the elements is 144,404 for the Eulerian domain and 640 for the wrapping Lagrangian fluid. The size of the element for the Lagrangian fluid and the interaction zone of the Eulerian fluid are refined as $h^{Lf} = h^{Ef} = c/80$, as in Figure 5.6 (b).

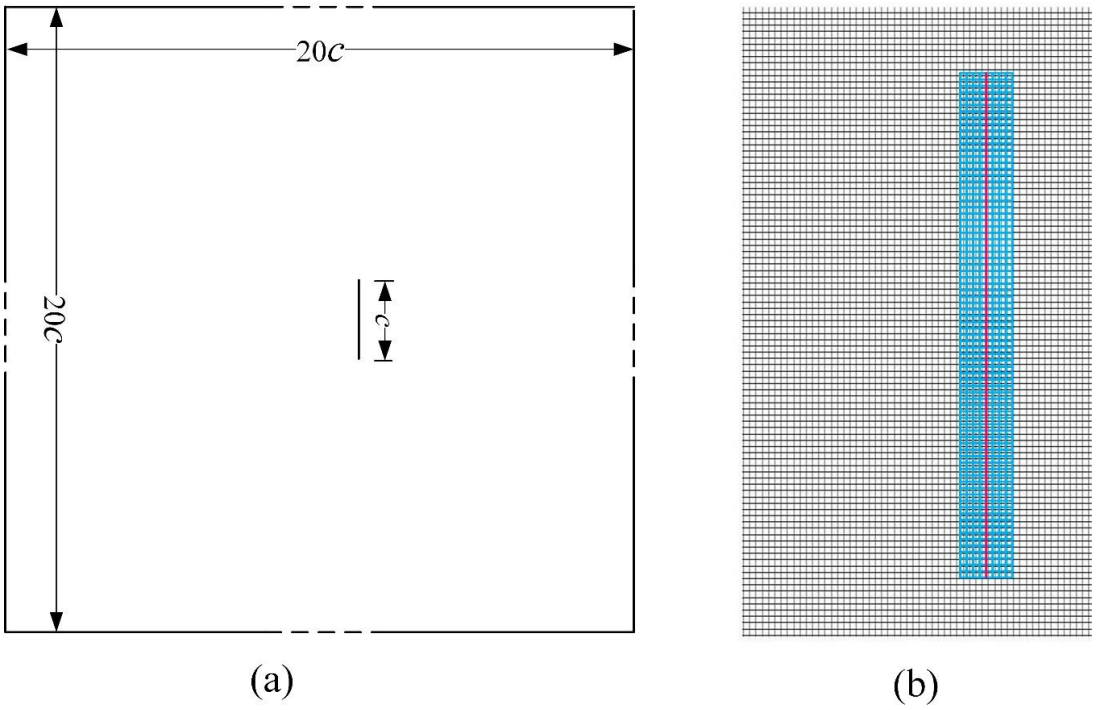

Figure 5.6: (a) Model of the 2D flapping thin wing at the initial stage; (b) zoom-in plot of the Lagrangian fluid meshes (blue) warp the thin structure (red) immersed in the background Eulerian fluid meshes (black).

Figure 5.7 shows the comparison between the lift/drag force coefficients obtained by the rod model using ELL thin, rigid body, and results from reference [99, 100] using the elliptical wing. There are small differences as expected due to the different geometries of the models. The vorticity contours at different time instants are shown in Figure 5.8, and those figures are quite identical with the results in [100]. The proposed method can deal with the FSI problem of a thin, rigid body moving in the fluid, and the results show an excellent agreement with those in references.

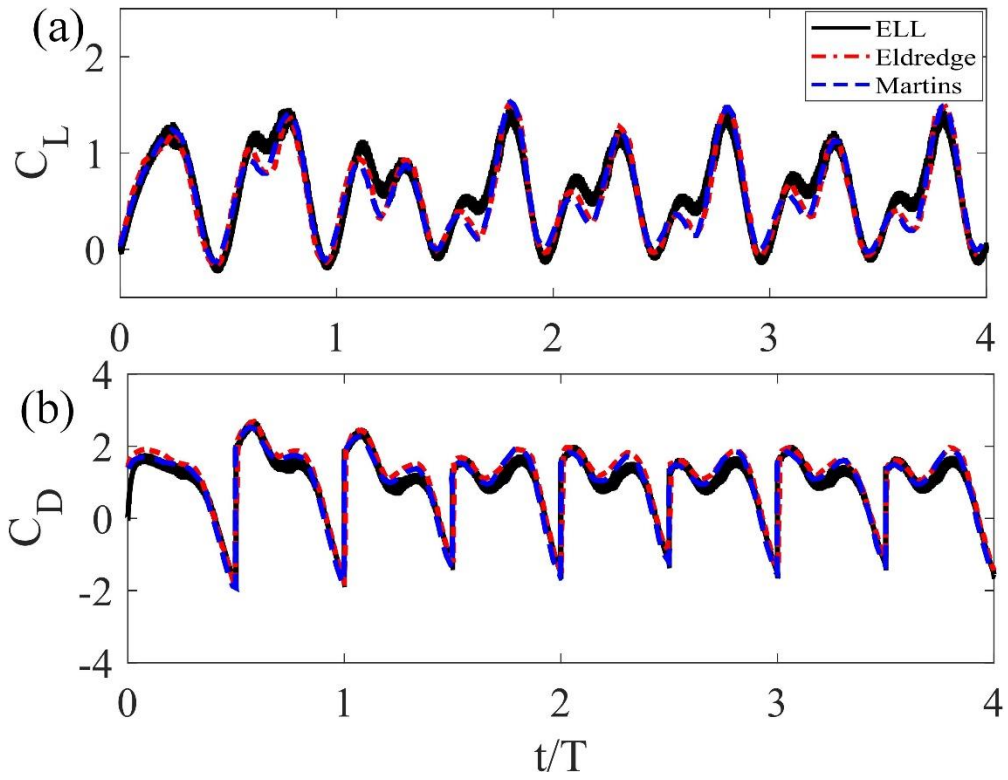

Figure 5.7: Time history of (a) lift and (b) drag force coefficients for the flapping wing. (ELL method uses rod model, Eldredge and Martins use elliptical wing with a thickness ratio of 10)

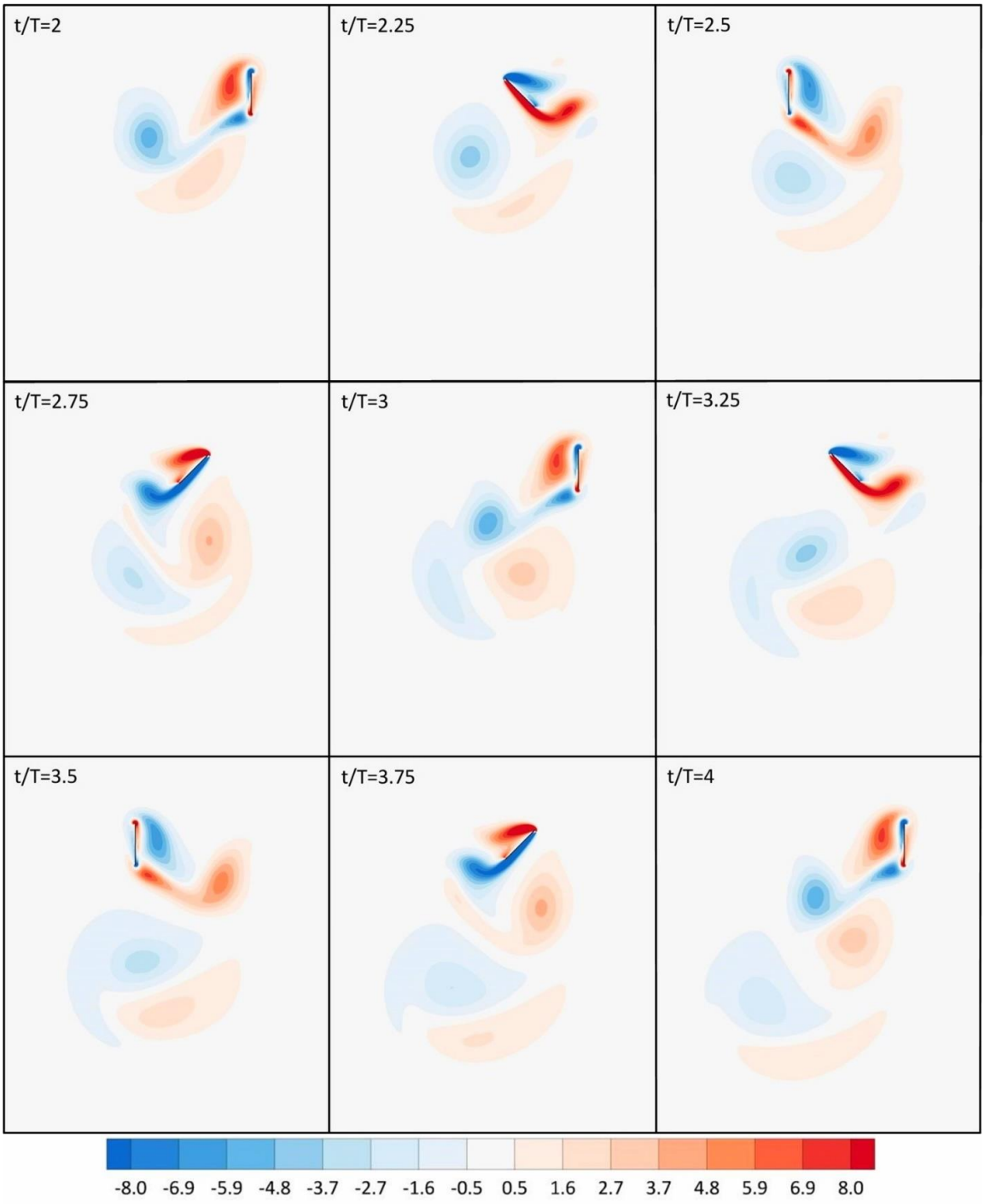

Figure 5.8: Vorticity field contours for different instants for the flapping wing movement

5.2 2D flexible

5.2.1 Vertical beam in a fluid tunnel

The vertical beam in the fluid tunnel, in example 4.3, is re-calculated based on the ELL incorporates CB beam element. The detailed model and geometry are shown in Figure 5.9 (a). All the setups are the same as in the previous case.

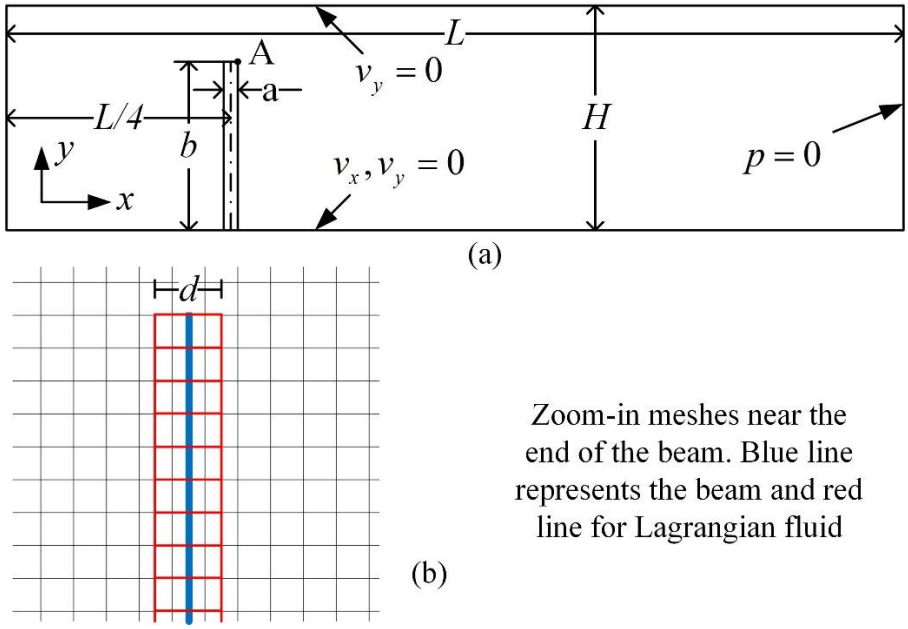

Figure 5.9: (a) Geometry and Model of the fluid and beam. (b) Zoom-in plot of the meshes near the free end of the beam and illustration of the beam and Lagrangian fluid element (MS1).

5.2.1.1 Thick beam and validation

First, a 'relative' thick beam, the same as in example 4.3, where $a = 0.04$ cm and the ratio between length and thickness is $b/a = 20$, is analyzed. The beam loses its thickness when applying a CB beam theory, and small layers of the Lagrangian fluid with the thickness $d = 0.04$ cm are intentionally designed to wrap the beam in every time step, as illustrated in Figure 5.9 (b).

Three sets of the meshes are employed as follows: MS(1), 4,894 nodes for the Eulerian fluid and 41 nodes for the beam and 123 nodes for the Lagrangian fluid so that the element size near the beam is $\Delta h^{Ef} = \Delta h^{Lf} = \Delta h^{s} = a/2$; MS(2) 16,354 nodes for the Eulerian fluid, 81 nodes for the beam, and 405 nodes for the Lagrangian fluid, element size near the beam is $\Delta h^{Ef} = \Delta h^{Lf} = \Delta h^{s} = a/4$; MS(3) 38,596 nodes for the Eulerian fluid, 161 nodes for the beam, and 1,449 nodes for the Lagrangian fluid, element size near the beam is $\Delta h^{Ef} = \Delta h^{Lf} = \Delta h^{s} = a/8$.

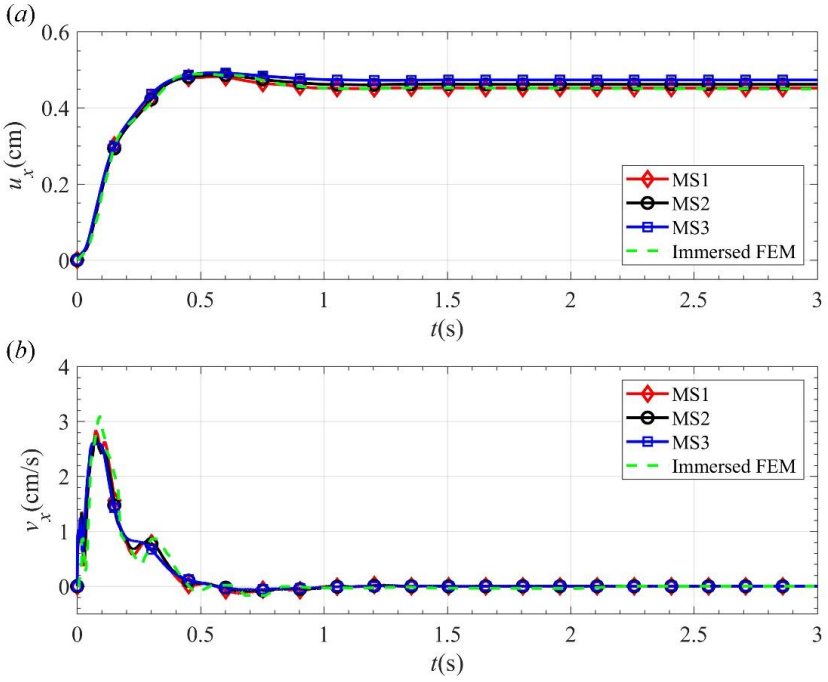

Figure 5.10: Time history of the (a) horizontal displacement and (b) horizontal velocity of the tip "A".

The histories of the velocity component v_x^s and the displacement u_x^s measured at the tip 'A' of the beam are displayed in Figure 5.10. These results match well in [61]. The relative error of the bending deformation after reaching a steady-state is below 5%. The CB beam deforms a bit larger than the continuum beam in reference due to the third

assumption of CB beam theory that ignores the transverse normal stress; therefore, it releases some internal energy and makes the beam a little softer.

The contour plots of the horizontal velocity field and pressure at different time steps are illustrated in Figure 5.11, and the close-up images of these plots in the vicinity of the free end of the beam are also shown on the right side of each plot. The pressure oscillation is also observed using the ELL method near the sharp corner of the free end due to the singularity in the velocity gradient. However, this singularity does not affect the smoothness of the velocity field itself; hence the distribution of the velocity field matches well with the reference as well as the pressure field reaches the steady-state. The streamlines at steady state are shown in Figure 5.12, and a stable vortex is formed in the downwind side of the beam.

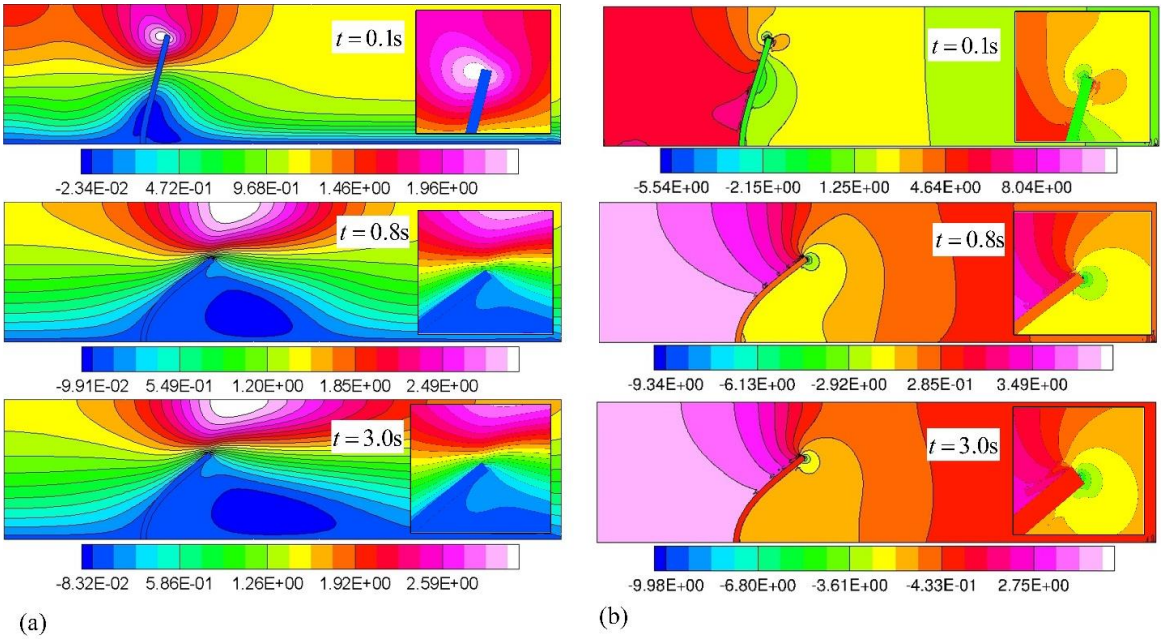

Figure 5.11: The snapshot of the contours: (a) horizontal velocity; (b) pressure. (Solved by MS3)

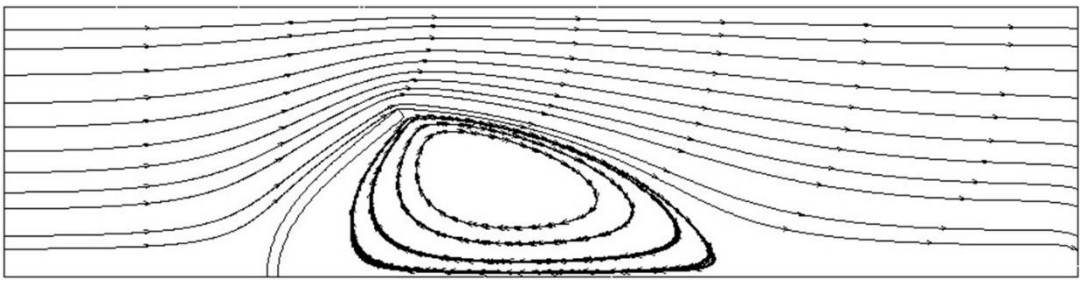

Figure 5.12: The streamline of at the steady-state. (Thick beam).

5.2.1.2 Thin beam

A thin beam with thickness $a = 0.01\,\text{cm}$, so $b/a = 80$, is computed in this subsection. Two cases with different Young's modules Case (1) $E = 10^5\,\text{g}/\left(\text{cm}\cdot\text{s}^2\right)$ and Case (2) $E = 10^7\,\text{g}/\left(\text{cm}\cdot\text{s}^2\right)$ are computed to extend the capability of the ELL method. Other parameters are set to be the same as the previous case.

A total number of 80 elements and 81 master nodes of the CB beam are used to model the beam, and a total of 405 nodes and 320 Q4 elements are used for Lagrangian fluid (thickness of the Lagrangian fluid is $d = 0.04\,\text{cm}$). A total number of 13,664 nodes and 13,442 elements are used for Eulerian fluid. The histories of the velocity components v_x^s and displacement u_x^s at the top of the beam are shown in Figure 5.13. It illustrates the contour plot of the horizontal velocity for both cases at different time steps, and the close-up image of the velocity field in the vicinity of the free end of the beam is also shown in the figures. It is interesting to find that, for the softer beam, the deformation begins from the bottom of the beam. While for the stiffer one, the deformation begins from the top of the beam, thus leading to the substantial velocity change for the stiffer one at the beginning

(shown in Figure 5.14 (a) and Figure 5.14 (b) around $t = 0.1\text{s}$). After both two cases reach a steady-state, it is reasonable to observe that the deformation of the softer beam is larger than the stiffer beam.

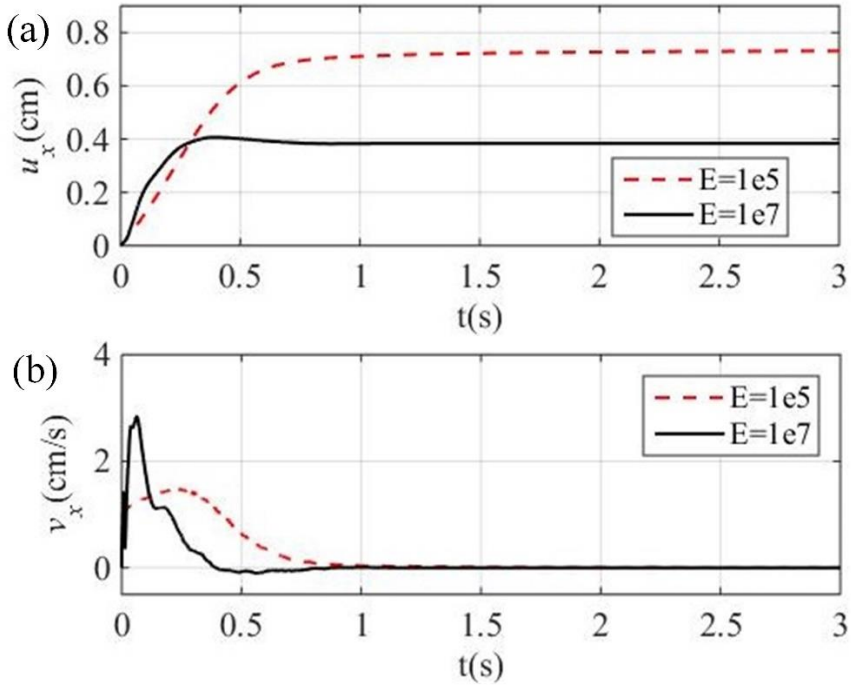

Figure 5.13: Time history of (a) the horizontal velocity v_x and (b) the horizontal displacement u_x at the top of the beam.

The streamlines at the steady-state for both cases are illustrated in Figure 5.15. For the stiffer beam, a stable vortex is produced similarly to the case in the previous subsection. The softer beam with smaller thickness differs from the stiffer beam or beam with the larger thickness (previous example) in the fact that the softer beam bends largely and forms a long narrow gap between the beam and the boundary, therefore excites no vortex in between.

When the ratio of length and thickness *b/a* becomes large, it will be a challenge to utilize the IMD method. The difficulty is due to the minimum requirement of at least five

elements across the beam thickness, if the continuum element is used, to avoid shear locking. The usage of the continuum element would lead to the extremely small size of the element, thus requiring a large number of meshes for both solid and fluid in the FSI zone. Figure 5.16 shows the comparison of the zoom-in mesh scheme in the FSI zone using conventional IFEM and ELL. Finer Eulerian fluid meshes are generated due to the small solid meshes in IFEM with a total number of 114,147 nodes. It has approximately sixteen times more degrees of freedom (DOFs) than in the ELL approach and thus computationally much more expensive.

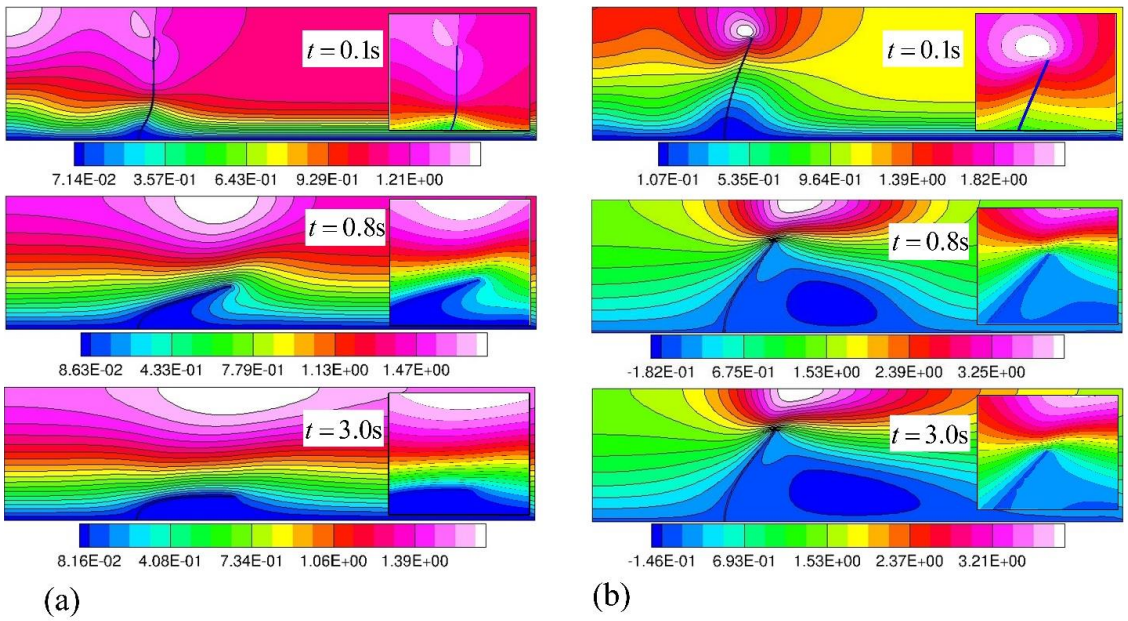

Figure 5.14: Snapshots of the contours of horizontal velocity v_x with Young's modulus: (a) $E = 10^5\ \mathrm{g}/\left(\mathrm{cm}\cdot\mathrm{s}^2\right)$ and (b) $E = 10^7\ \mathrm{g}/\left(\mathrm{cm}\cdot\mathrm{s}^2\right)$.

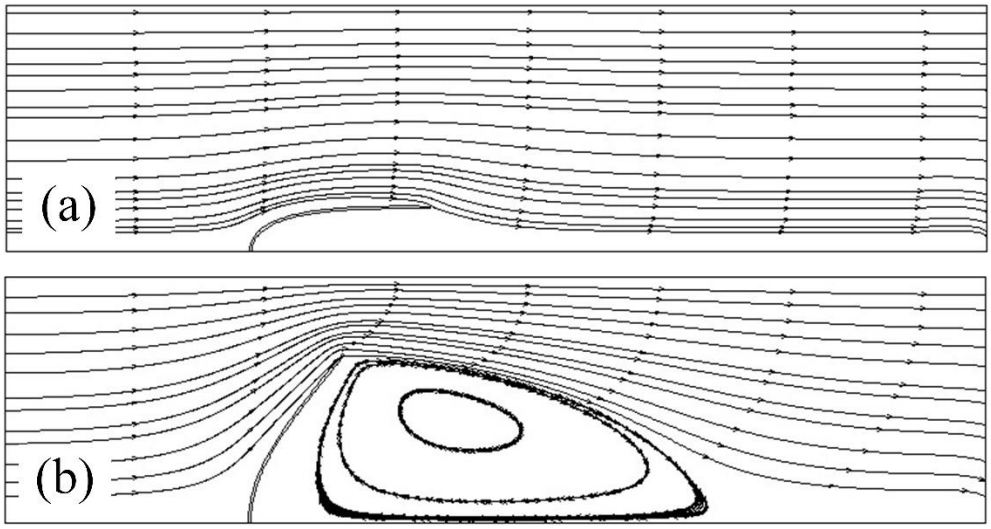

Figure 5.15: Streamlines at the steady-state of (a) Case 1 and (b) Case 2.(Thin beam)

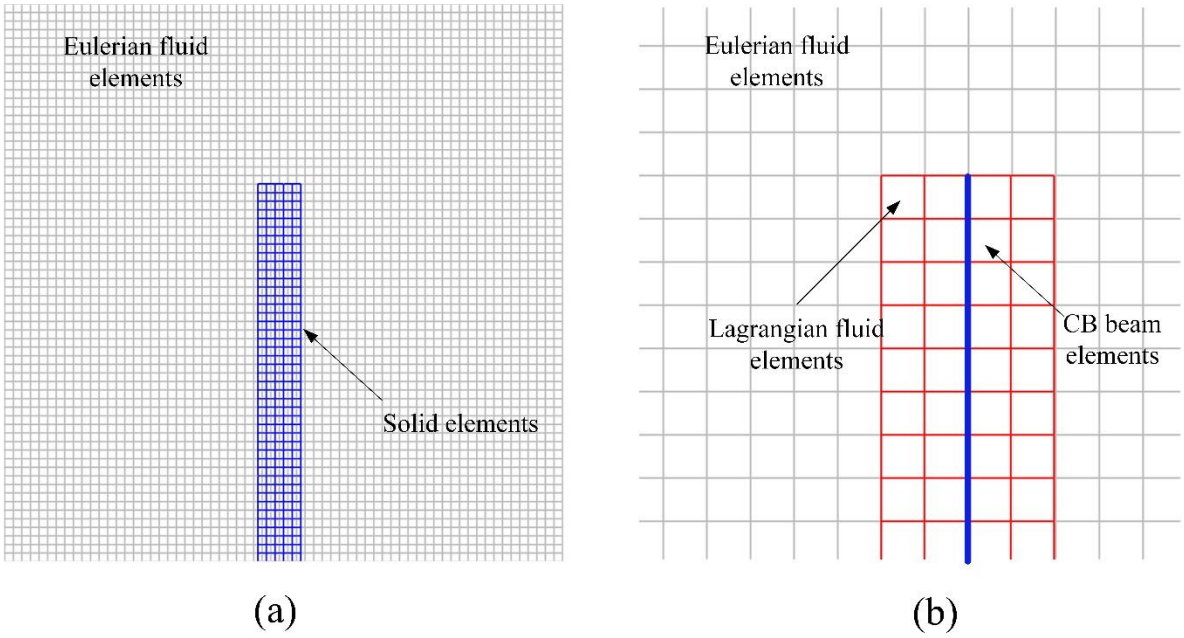

Figure 5.16: Zoom-in plot of meshing schemes for (a) IFEM and (b) ELL.

5.2.2 Flow passing a flexible beam attached to a cylinder

The 2D benchmark problem of a flexible beam attached to a rigid cylinder in the downstream flow is simulated [103-105]. This problem has been used widely to validate

the FSI solver involving a large displacement of the solid model. The detailed geometry of the problem is illustrated in Figure 5.17. The nonslip boundary condition is applied on the top and bottom walls. The fluid inlet is placed on the left side and has a parabolic velocity profile with mean inlet velocity $\bar{U}$. The pressure outlet is set on the right side. The diameter of the cylinder is *D*. The length of the beam is *L=3.5D*, and the thickness is *h=0.2D*. The Reynolds number is defined as $\mathrm{Re} = \rho^f \bar{U} D / \mu$. Two cases are computed,

Case (1). $\rho^s / \rho^f = 10$, Re=100;

Case (2). $\rho^s / \rho^f = 1$, Re=200.

The other material property parameters of the beam are chosen $E^* = E / \rho^f \bar{U}^2$. *E* is Young's modulus, and Passion's ratio is $\upsilon = 0.4$. A total number of 35,451 nodes and 35,084 Q4 elements are used for the background Eulerian fluid for both cases. The meshes are refined in the FSI zone around the cylinder and beam system, and the size of the finest mesh is $\Delta h^{Ef} = 0.025D$. In order to implement the ELL method, a small portion of the Lagrangian fluid is generated to wrap the beam. In case (1), we discretized the beam with the same size of the Eulerian fluid mesh in the FSI zone, i.e. $\Delta h^s = \Delta h^{Lf} = \Delta h^{Ef}$. A total number of 140 CB elements are thus used to model the beam. Four layers of the Lagrangian fluid with a total number of 705 nodes and 560 elements are generated and used for this case. In case (2), we used a double-sized element, i.e. $\Delta h^s = \Delta h^{Lf} = 2\Delta h^{Ef}$, for the beam and wrapping Lagrangian fluid.

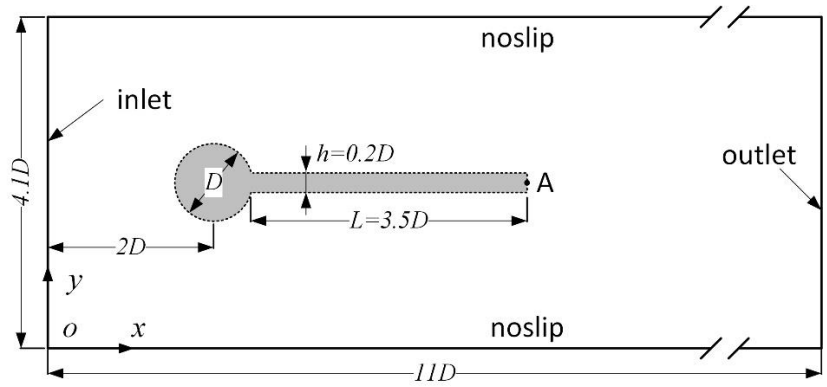

Figure 5.17: The geometry of the fluid flow passing a flexible beam attached to a rigid cylinder

The flexible beam will settle into a large amplitude self-induced periodic oscillation, and reach a stable-state vibration eventually. The time-varying displacement of the free end (point marked with 'A' in Figure 5.17) in *x*- and *y*-direction for case (1) is shown in Figure 5.18. The results from Turek & Hron [103] are also plotted in the figure as reference. The snapshots of the pressure contour, streamlines, deformation of the beam at four-time instances in one cycle of oscillation are shown in Figure 5.19 for case (1). The Strouhal number is defined by $St = fD/\bar{U}$, where f is the vibrating frequency of the beam reaches a stable-state oscillation. Table 5.1 shows the displacement amplitude *Am* of free end in the *y*-direction along with Stouhal number *St* for both cases. Data of several references are also collected and provided in the table. From the results in these figures and data in the table, the present ELL method shows an excellent agreement with results in the references.

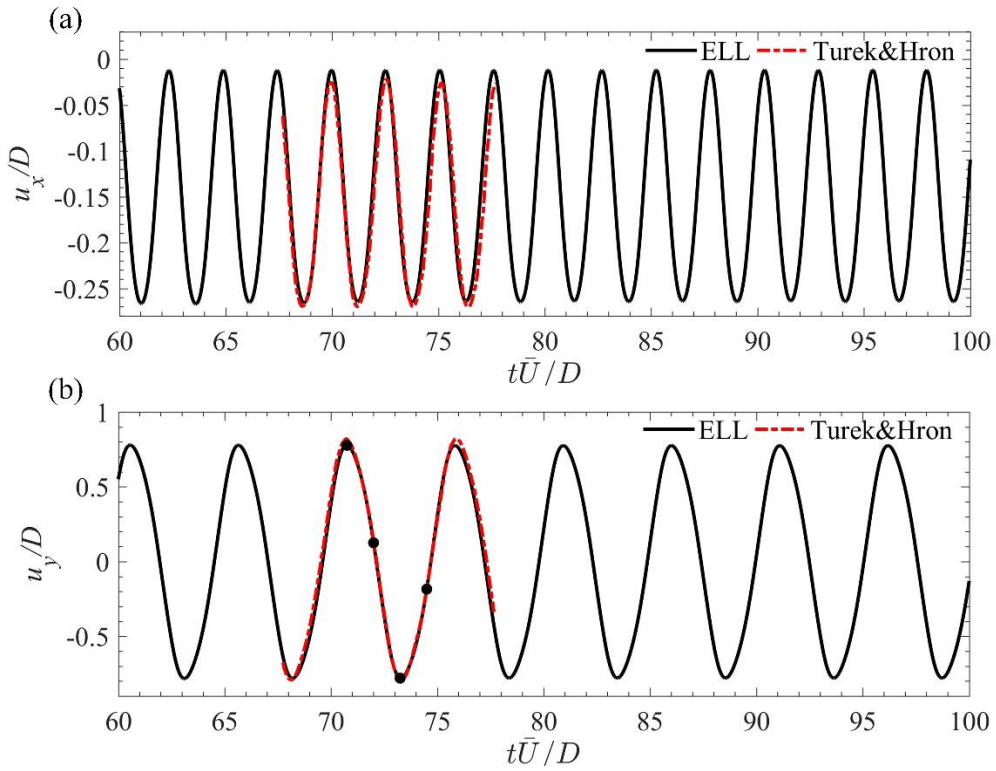

Figure 5.18: History of the displacement of the free end of the beam for case (1).

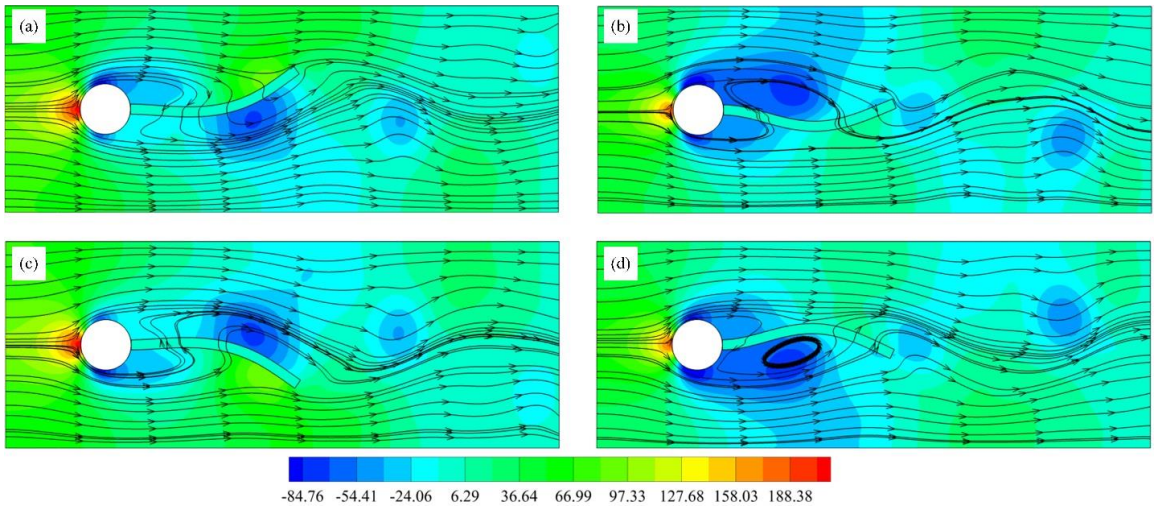

Figure 5.19: A snapshot of fluid pressure contours and streamlines at four instances labeled in Figure 5.18 (b).

Table 5.1. 2D flow over a flexible beam attached to a cylinder. The amplitude of the displacement in the *y*-direction of the free end along with the Strouhal number.

Sources	Case (1)		Case (2)	
	Am/D	*St*	*Am/D*	*St*
ELL	0.78	0.19	0.39	0.28
Turek & Hron [103]	0.83	0.19	0.36	0.26
Tian et al [104]	0.78	0.19	0.32	0.29
Bhardwaj & Mittal [105]	0.92	0.19	0.41	0.28

5.2.3 Flapping flag in the uniform flow

There have been many studies of the unsteady phenomenon [106-115] of the flapping flag in the uniform flow since Zhang et al. addressed it experimentally [116]. Since the problem has been studied using many different algorithms, we solve this problem to validate the ELL method in solving the FSI problem with a very thin structure. A beam (flag) is placed in the middle of a tunnel pinned (not clamped) at the left end, and the right end is free. The detailed geometry of the model is shown in Figure 5.20 (a). The beam is placed in an initial orientation angle $\theta = 0.1\pi$ with respect to the constant incoming flow and constant gravity *g* in the *x*-direction. The length of the beam is *L*. The thickness of the beam is $h = 0.01L$, so the ratio of length and thickness is $L/h = 100$ in this case. The computational domain for the Eulerian fluid is $[-5L, 50L] \times [-10L, 10L]$. Uniform flow $v_x^f = U$, $v_y^f = 0$ is prescribed at the inlet, as well as on the upper and bottom sides. The right side wall is defined as an outlet.

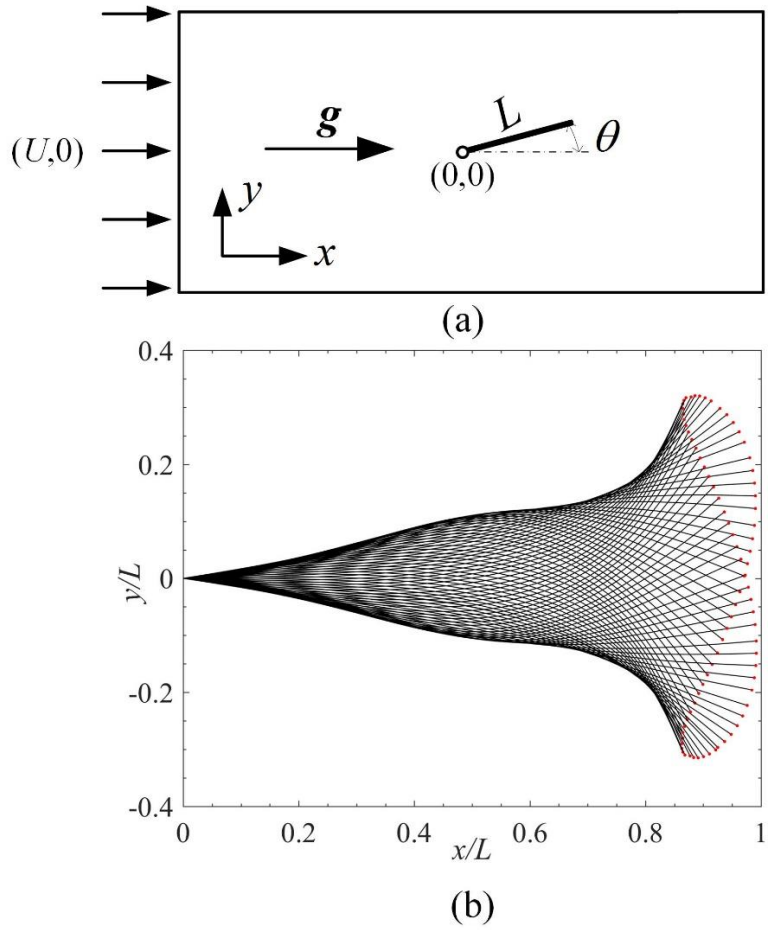

Figure 5.20: (a) Problem setup of the flapping flag (beam) in uniform flow. (b) Flapping flag configuration at several time steps at stable-state oscillation. The free end of the flag is labeled in red dots and shows the "figure of eight" trajectory.

A total number of 65,170 nodes and 64,696 elements are used for the Eulerian fluid with the finest mesh $\Delta h^{Ef} = 0.02L$ near the beam $[-0.5L, 2L]\times[-L, L]$. A total number of 60 elements and 61 nodes are used for the CB beam. Four layers of the Lagrangian fluid meshes with the same size of the finest Eulerian fluid mesh are included in this simulation. The number of nodes and elements for the Lagrangian fluid is 305 and 240, respectively.

The beam would be excited to oscillate if proper parameters are chosen. The first dimensionless parameter that would affect the system is the Reynolds number, which is

defined as $\mathrm{Re} = \rho^f UL/\mu$. The other three dimensionless parameters that govern the system are a structure-to-fluid mass ratio, non-dimensional bending rigidity and the Froude number given respectively as,

$$\lambda = \frac{\rho^s h}{\rho^f L}, \quad K_B = \frac{EI}{\rho^f U^2 L^3}, \quad Fr = \frac{U}{\sqrt{gL}} \tag{5.3}$$

where $I = h^3/12\left(1-\upsilon^2\right)$ is the second moment of area. To validate the proposed ELL algorithm, we replicate the test delivered by Huang et al. [106] and Lee and Choi [112]. The dimensionless parameters are chosen as $\mathrm{Re} = 200$, $\lambda = 1.5$, $K_B = 0.0015$ and $Fr = 1.4$.

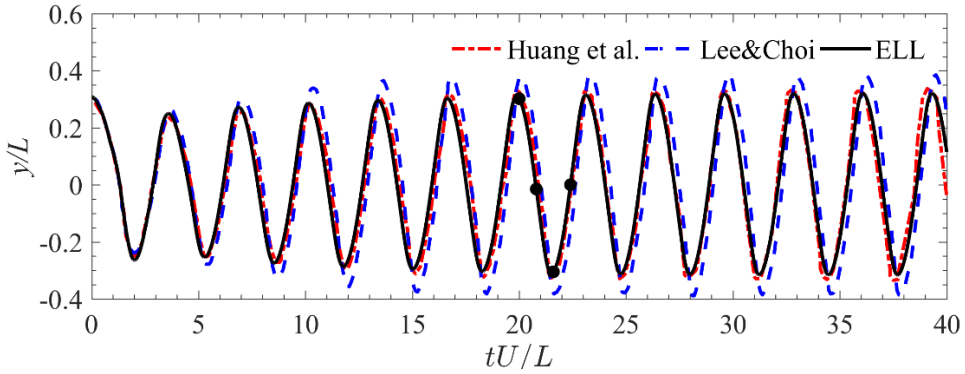

Figure 5.21: Time history of the vertical location at trailing-edge (free end) in comparison with the reference.

Figure 5.21 shows the time history of the vertical location at trailing-edge (the free end) of the beam along with the results from Huang et al. and Lee and Choi. From the figure, we note that the flexible beam reaches a stable-state periodic oscillation after an approximately dimensionless time of 20. The configurations of the flag at several time steps during stable-state oscillating are shown in Figure 5.20 (b). The free end of the flag is labeled in red dots and shows the "figure of eight" that has been observed in [116].

Strouhal number is calculated by $St = fL/\bar{U}$, where f is the frequency during stable-state vibration. The qualitative comparison of the y-component displacement amplitude Am/L and Strouhal number St between present ELL method and several references are also listed and shown in Table 5.2. Figure 5.22 shows the instantaneous vorticity contours at four-time instants with releasing vortex structure along the downstream of the flag. These results are all in good agreement with results in references, which shows the novel capability and feasibility of ELL in solving FSI problems with the thin structures.

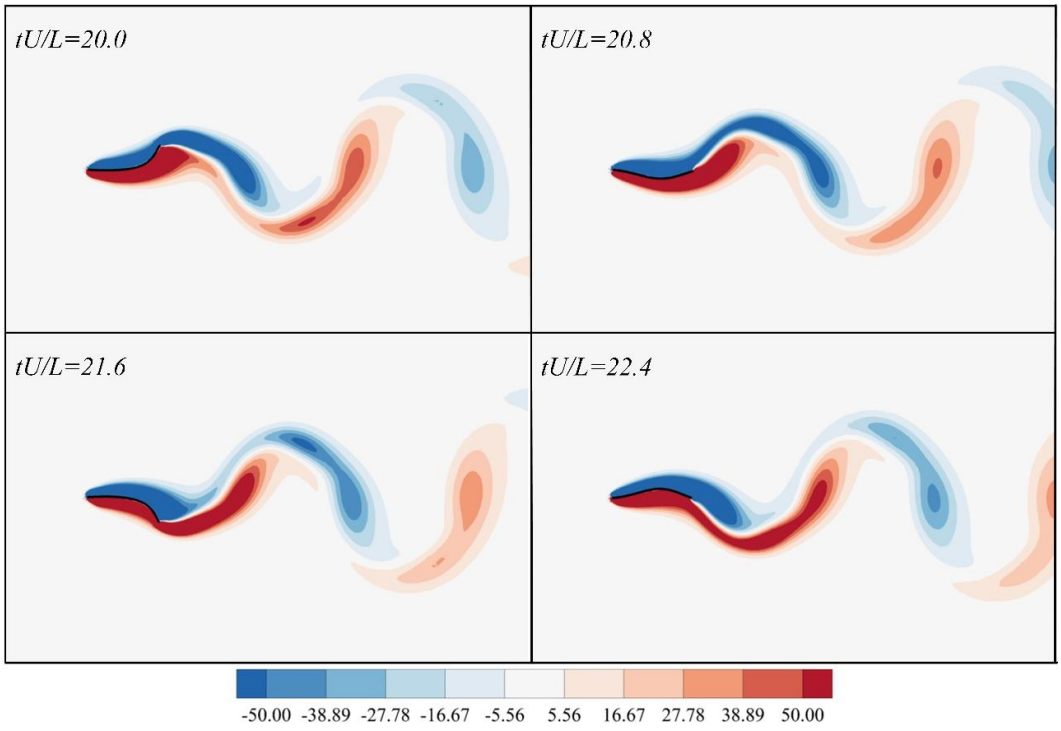

Figure 5.22: Instantaneous plots of the vorticity contours for fully developed flow at dimensionless time step *tU/L* = 20.0, 20.8, 21.6 and 22.4 (labeled in solid circles in Figure 15).

Table 5.2. 2D flapping flag in the uniform flow. The amplitude of the displacement in the *y*-direction of the free end along with the Strouhal number.

Sources	Amplitude *Am/L*	Strouhal number *St*
ELL	0.32	0.31
Huang et al. [106]	0.35	0.30
Lee & Choi [112]	0.38	0.31
Wang & Eldredge [114]	0.35	0.31
Goza & Colonius [115]	0.38	0.32

CHAPTER 6. 3D NUMERICAL EXAMPLE FOR ELL WITH THIN STRUCTURES

In this chapter, numerical examples of ELL for solving 3D FSI problems with thin solid bodies are studied. FSI problems with rigid bodies moving in the fluid are first calculated and validated. Then, the CB shell element is employed in ELL to solve 3D FSI problems with thin flexible structures.

6.1 3D rigid

6.1.1 Plate piston in a fluid tunnel

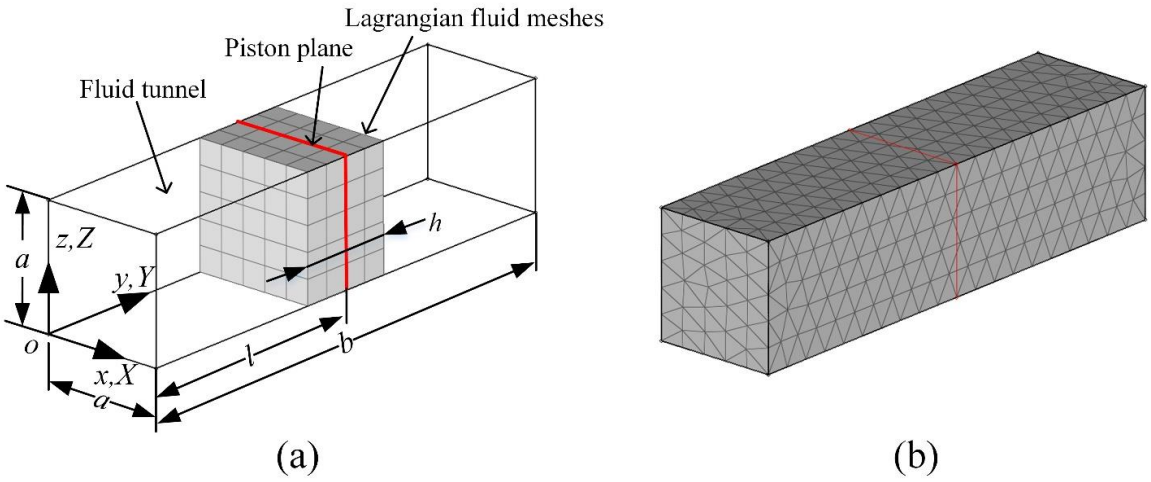

Figure 6.1: (a) The 3D geometry of the moving plate piston (represented by the red line) in the tunnel, and the illustration of H8 meshes for the Lagrangian fluid. (b) The T4 meshes for Eulerian fluid for the fluid tunnel.

In this example, we calculate a plate piston moving inside the tunnel with an incompressible viscous fluid, as illustrated in Figure 6.1. The plate piston, represented by the red line in Figure, is thin enough that it has no thickness. The detailed geometry parameters of the problem are given as a = 0.5 m, and b = 2 m, the piston moves from the

initial position as $l = 0.3$ m. A small portion of the Lagrangian fluid with a thickness of h is used to wrap the piston. The incompressible fluid has a density of $\rho^f = 1 \text{ kg}/\text{m}^3$ and viscosity $\mu^f = 0.5 \text{ Pa} \cdot \text{s}$.

To show the versatile property of the ELL method in solving the 3D problem, two different thicknesses of the Lagrangian fluid is used in this example (a) $h = 0.1$ m and $h = 0.4$ m with total 363 nodes (element size 0.05 m) and 180 nodes (element size 0.1 m) for each thickness respectively. A total of 4,436 nodes with element size 0.05 m is obtained for the Lagrangian fluid. The Eulerian fluid element is a four-node tetrahedron (T4), and the Lagrangian fluid element is an eight-node hexahedron (H8). The initial and boundary conditions of the Eulerian fluid are given as (i) symmetric velocity boundary condition on surfaces $x = 0$, $x = a$; $z = 0$ and $z = a$; (ii) pressure boundary $p^f = 0$ on $y = 0$ and $y = b$; (iii) initial velocity ${}^0v_i^f = 0, (i = 1,2,3)$ and initial pressure ${}^0p^f = 0$. The Lagrangian fluid has the same velocity boundary and initial conditions. Additionally, a constant moving velocity $v_y^s = 2.0 \text{ m/s}$ is applied to the shared nodes of the plate piston and Lagrangian fluid.

The motion of the piston along the y-direction would induce a laminar fluid flow inside the tunnel. The analytical velocity solution of the fluid flow is $v_x^f = v_z^f = 0$ and $v_y^f = 2.0 \text{ m/s}$. The system is quick to reach the steady-state defined as $ef < 1\text{e}-6$, therefore, we set a certain length of time $t = 0.2 \text{ s}$ to stop the simulation. The time interval for each step is 1e-5s. Figure 6.2 shows the contour plots of the velocity component v_y^f and pressure p^f with the streamlines on the slice surfaces $x = a/2$ and $z = a/2$ at the terminal time $t = 0.2 \text{ s}$. The stable laminar flow is shown in terms of streamlines and velocity

contour plots. These results show that ELL can handle different thicknesses of the wrapping Lagrangian fluid and different combinations of the mesh size of Lagrangian fluid and Eulerian.

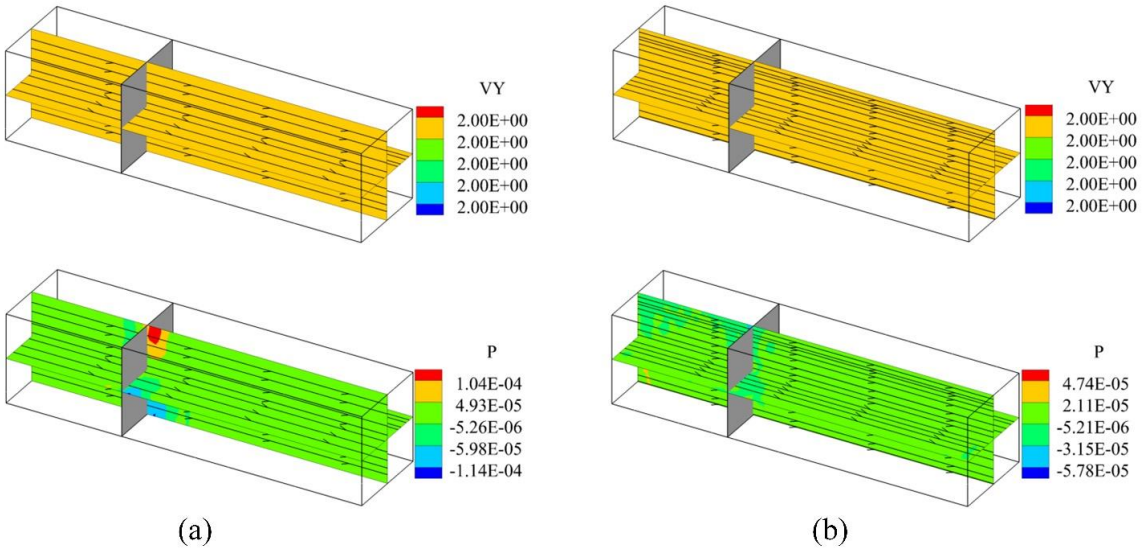

Figure 6.2: The contour plots of the velocity component v_y^f and pressure p^f with the streamlines with the wrapping Lagrangian fluid with total thickness (a) h = 0.4 m and (b) h = 0.1 m.

6.1.2 3D rotating ring in a cuboid fluid

The rotating ring immersed in a square fluid is examined to be an excellent numerical example to verify the ELL method in 2D previously. The model is extended in 3D to check the performance of ELL for solving the 3D FSI problem with a thin moving rigid body. The geometry and mesh schemes of the problem are illustrated in Figure 6.3, with the thickness of the fluid domain is $d = 0.1\text{m}$. Other parameters are the same as in the 2D case.

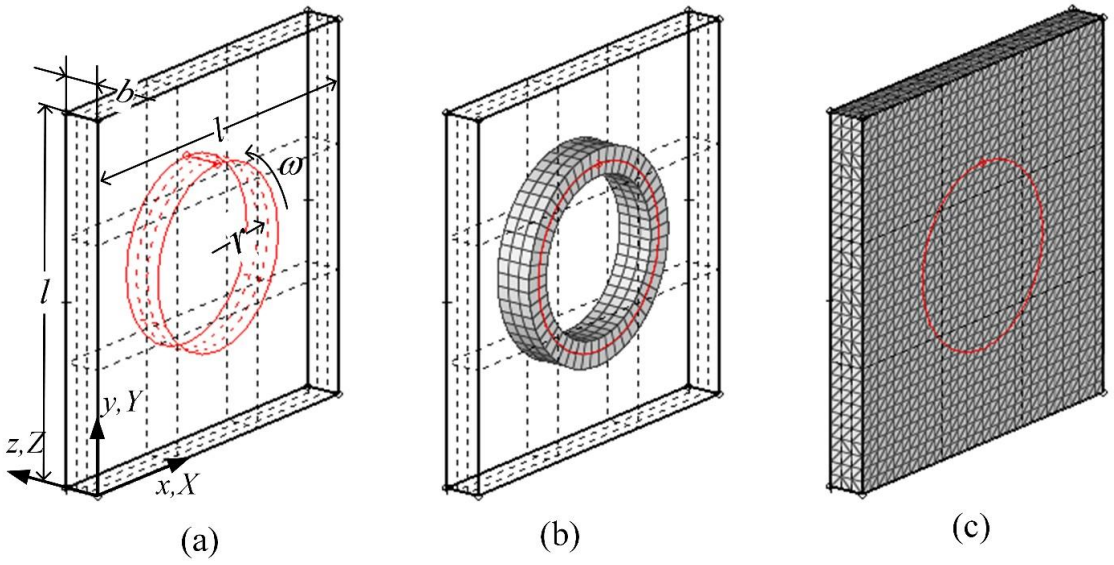

Figure 6.3: (a) 3D Geometry and model of the rotating ring in the fluid; (b) Lagrangian fluid meshes; (c) Eulerian fluid meshes.

The 3D solution of the *x*-*y* plane would be comparable to the 2D solution under the following boundary conditions:

V.B.C for the Eulerian fluid: (a) Non-slip conditions, i.e. $v_i^f = 0, i = 1,2,3$, are enforced on the four surfaces $x = 0$, $x = l$, $y = 0$, and $y = l$, (b) Symmetric boundary conditions for surfaces where $z = 0$ and $z = b$.

P.B.C for the Eulerian fluid: Zero pressure $p^f = 0$ on the line $(l/2, l/2, z)$.

The system is initially at rest where velocity and the pressure are all set to zero that is ${}^0v_i^f = 0, i = 1,2,3$ and ${}^0p^f = 0$. The ring rotates when the simulation begins. A small portion of the Lagrangian fluid is required to warp the moving boundary. The rotational velocity of the ring can then be prescribed on the nodes of the Lagrangian fluid meshes as

the velocity boundary condition when solving Lagrangian fluid. H8 elements are for the Lagrangian fluid, and T4 elements are for the Eulerian fluid.

Several sets of the Eulerian fluid meshes are investigated, i.e., (a) $h^{Ef} = 1/30$; (b) $h^{Ef} = 1/44$; (c) $h^{Ef} = 1/60$; (d) $h^{Ef} = 1/80$ and (e) $h^{Ef} = 1/160$. In this example, we confine two layers of the Lagrangian fluid meshes to warp the ring and its element size changes with respect to the Eulerian mesh, i.e. $h^{Lf} \cong h^{Ef}$.

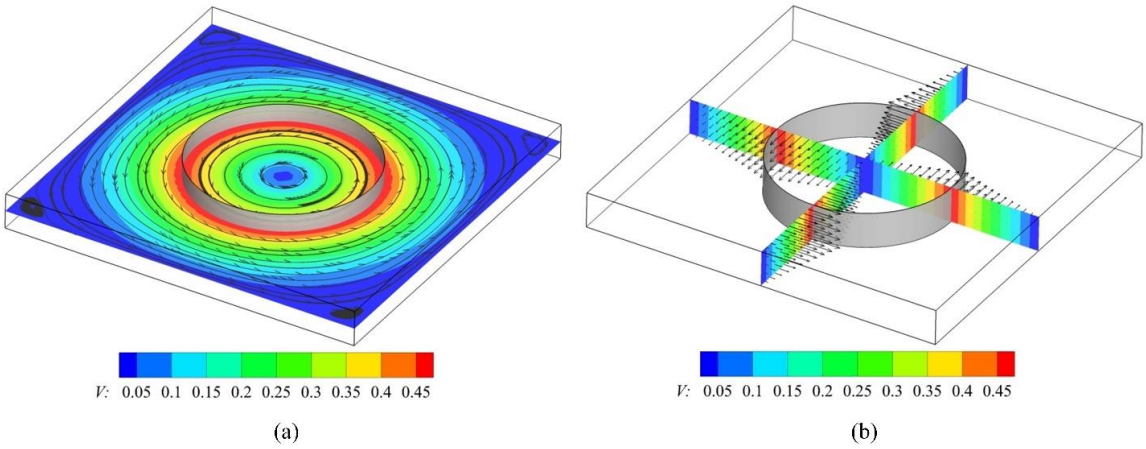

Figure 6.4: (a) The velocity and the streamline on the surface $z = d/2$. (b) The velocity vectors on surfaces $x = l/2$ and $y = l/2$ of the 3D rotating ring.

The rotating ring induces fluid flow in the fluid domain. The flow inside the ring would perform a solid body rotation after reaching a steady-state if the flow remains laminar; thus, the exact solution can be obtained. Figure 6.4 (a) shows the velocity and the streamline of the fluid domain on the slice surface $z = d/2$, and Figure 6.4 (b) shows the velocity vectors on the slice surface $x = l/2$ and $y = l/2$. These plots show the fluid flow inside the ring is rotating like a solid. The maximum velocity $v^f = 5.0\,\text{m/s}$ is attained at nodes nearest to the ring, as proved in the 2D solution. Figure 6.5 shows the spatial

convergence corresponding to the size of the Eulerian fluid size. The spatial convergence rate for the fluid velocity is 1.65.

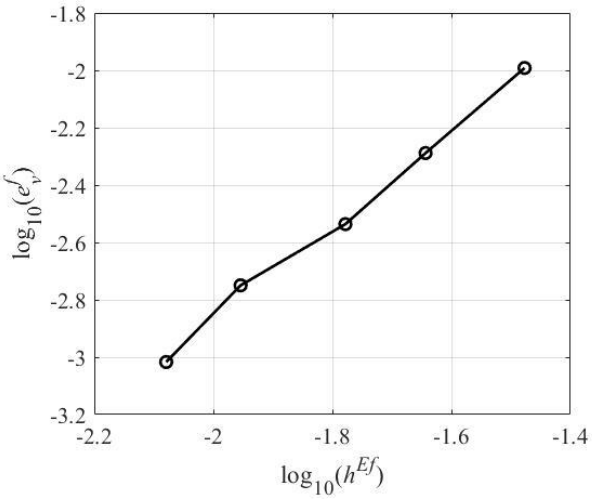

Figure 6.5: The spatial convergence rate in the example 6.1.2.

6.1.3 Symmetric flapping wings of a butterfly

This example is a simulation of the symmetric flapping wings of a butterfly using the ELL method. In this case, the geometry of the model is more complex, which includes a combination of a bulk body and thin wings. Therefore, we use a combination of IFEM for the body and ELL for the wings. The actual kinematics of the butterfly is more complicated involving rolling amplitude, pitch angles, and frequency change of the flapping wing, and so on for different purposes of flight. In this simulation, a simplified motion of symmetric flapping is considered.

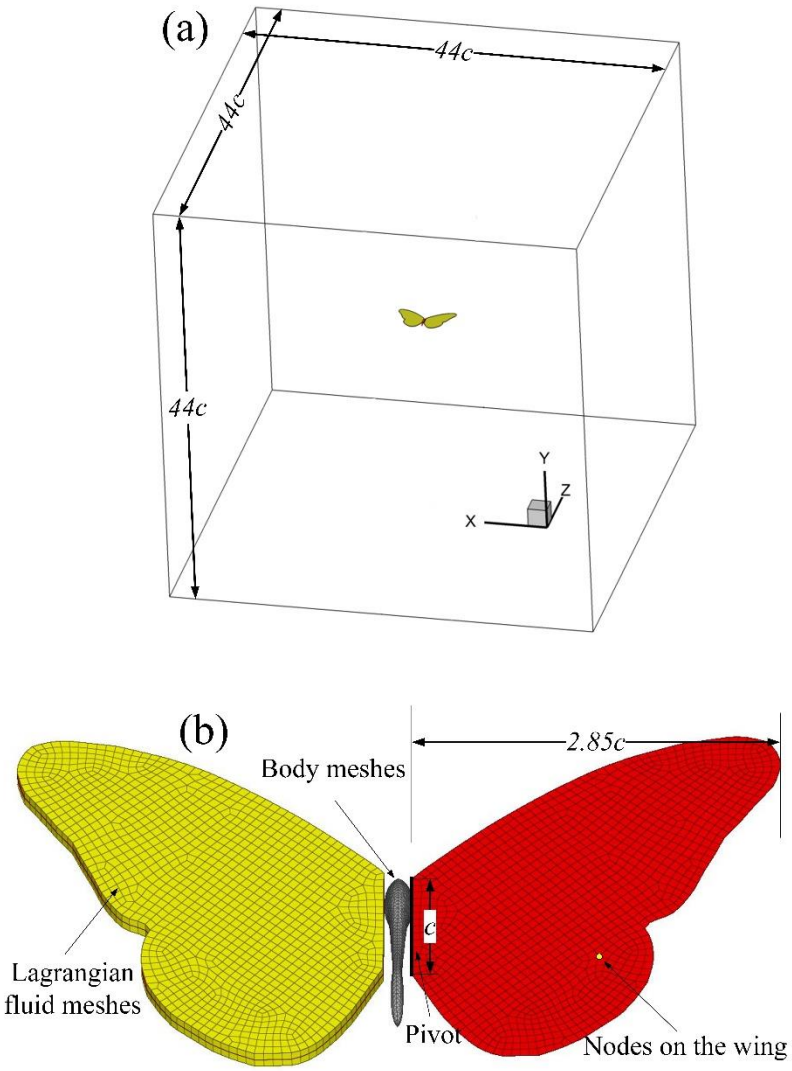

Figure 6.6: (a) 3D geometry of the flapping butterfly (b) meshes of the butterfly

The detailed geometry and meshing are illustrated in Figure 6.6. A total of 1,054 nodes and 3,856 T4 elements are used for the body, and two layers of H8 elements with a total number of 2,327 are included for the Lagrangian fluid. The size of the computation domain for the Eulerian fluid is $44c \times 44c \times 44c$, where c is the root chord length of the wing, and the maximum length of the single wingspan is $2.85c$. The total numbers of nodes and elements for the Eulerian fluid are 956,397 and 5,500,300, and we refine the elements in the fluid-structure interaction region. Initially, the wing plate of the butterfly is parallel

to the *x*-*y* plane. The root chord of the butterfly, parallel to the *z*-direction, services as the pivot, and each wing undergoes a symmetric sinusoidal up-stroke and down-stroke flapping motion about the chord during the simulation. The angle of the flapping wing is prescribed as

$$\theta = \alpha \sin(\omega t) \tag{6.1}$$

where α is the amplitude of the stroking angle, and two cases of (i) $\alpha = \pi/6$ and (ii) $\alpha = \pi/4$. The angular frequency is $\omega = 100\pi$. The butterfly begins up-stoke in simulation at the time $t = 0$. The Reynolds number of flapping wings is defined as $\mathrm{Re} = \bar{U}_\infty c/\mu$, where $\bar{U}_\infty$ is the average velocity and μ is the dynamic viscosity of the fluid [42, 46]. Reynolds number is $\mathrm{Re} = 224$ for case (i) and $\mathrm{Re} = 336$ for case (ii).

Figure 6.7 shows the flow structure of the symmetric flapping butterfly at three different stages in the flapping cycles. These figures show the iso-surfaces of the vorticity magnitude. In Figure 6.7 (a) and (d), the flapping angle of the wings is increasing to a peak value, while velocity is decreasing to zero. At this stage, vortices of the tip and wake are forming on the lower surfaces. The wings reach the center position of a cycle down-stoking with maximum velocity in Figure 6.7 (b) and (e). The magnitude of the vorticities is larger because the wings have the highest velocity in this stage. The vortices dominate on the upper surface of the wings, and some remnant vortex can also be observed at the edge of the lower wingtips. Figure 6.7 (c) and (f) show the wings up-strokes accelerate from the lowest position. At the stage, the vortex on the surface has shifted to the lower wing surfaces while a large portion of the wake vortices remains on the upper wing surfaces. Vortex is also observed on the body of the butterfly, although it is set at rest during the

simulation. It oscillates around the body to the wing's motion. Case (ii) has larger vorticity than case (i) because it has a larger flapping angle.

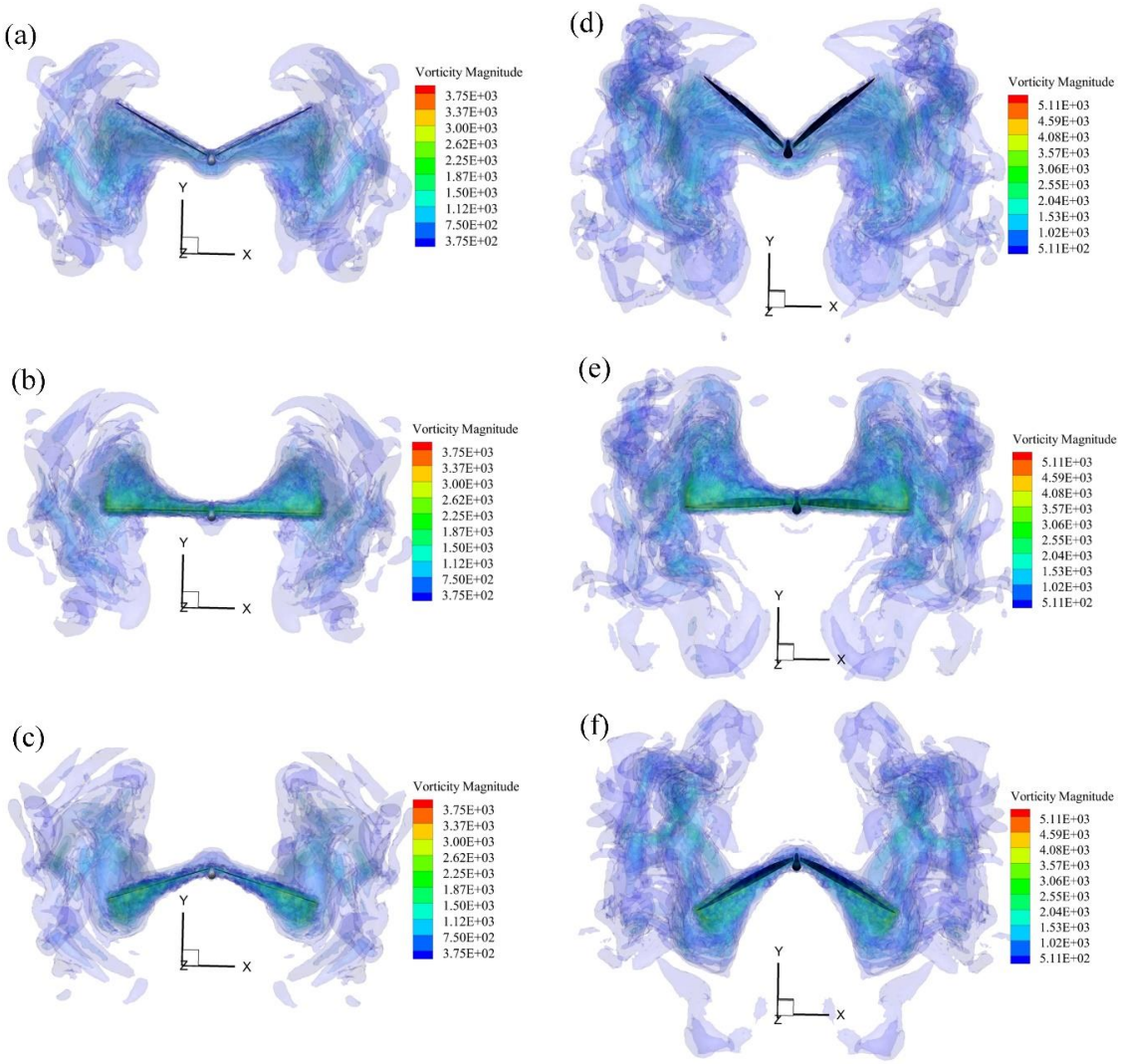

Figure 6.7: Vortex structures at three different stages in a flapping cycle with different magnitude of the flapping angle. (a), (b) and (c) are for case (i) and (d), (e) and (f) are for case (ii). The timestamps are $t = 3.2T$ for (a) and (d), $t = 3.5T$ for (b) and (e) and $t = 3.9T$ for (c) and (f). *T* is the period of a full cycle.

Figure 6.8 shows the time-varying force coefficients for a single wing during the first five cycles. The force coefficients are defined as C_x, C_y and C_z. They are obtained by adding the external nodal force in each direction and normalizing them by $0.5\rho\bar{U}_\infty^2 c^2$.

From the plots, C_z is nearly zero since the wings are flapping symmetrically about the pivot, which is parallel to the *z*-axis; no significant resistant force is obtained. The vertical force C_y decreases dramatically at the beginning of the simulation, which can be attributed to the up-stroking of the wing from a stationary state. It is symmetric during the simulation, which has a good match that the butterfly is undergoing a symmetric flapping motion. The horizontal force C_x also changes periodically synchronizing with the sinusoidal flapping wings. However, it is not necessary to be symmetric as the Reynolds number is bigger than 200, as reported in [117].

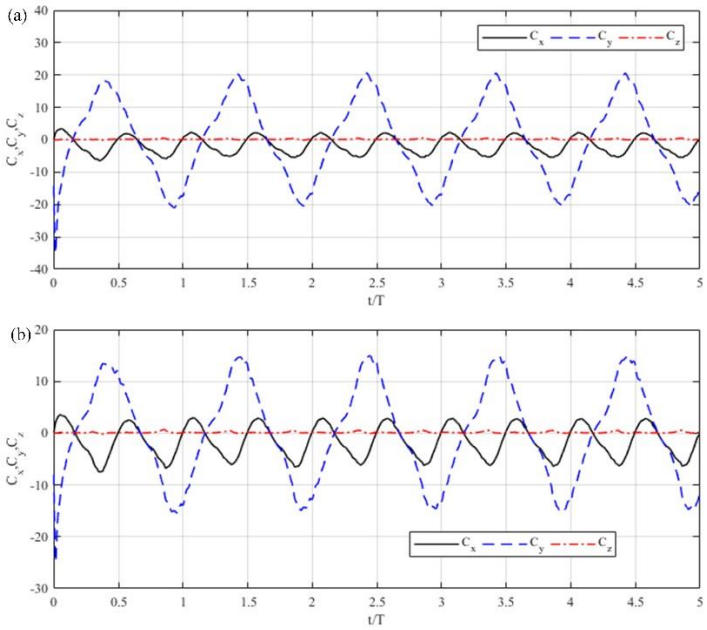

Figure 6.8: Time histories of the normalized force components C_x, C_y and C_z (a) for case (i) and (b) for case (ii) in the first five flapping cycles.

6.2 3D flexible

6.2.1 Vertical beam in a fluid tunnel

This example extends the 2D vertical beam in a fluid tunnel to 3D, as illustrated in Figure 6.9 (a) with a thickness in-depth *d*. The inlet is defined at the left surface of the fluid domain. The symmetric velocity condition is assumed at the top surface along with the front and rear surfaces.

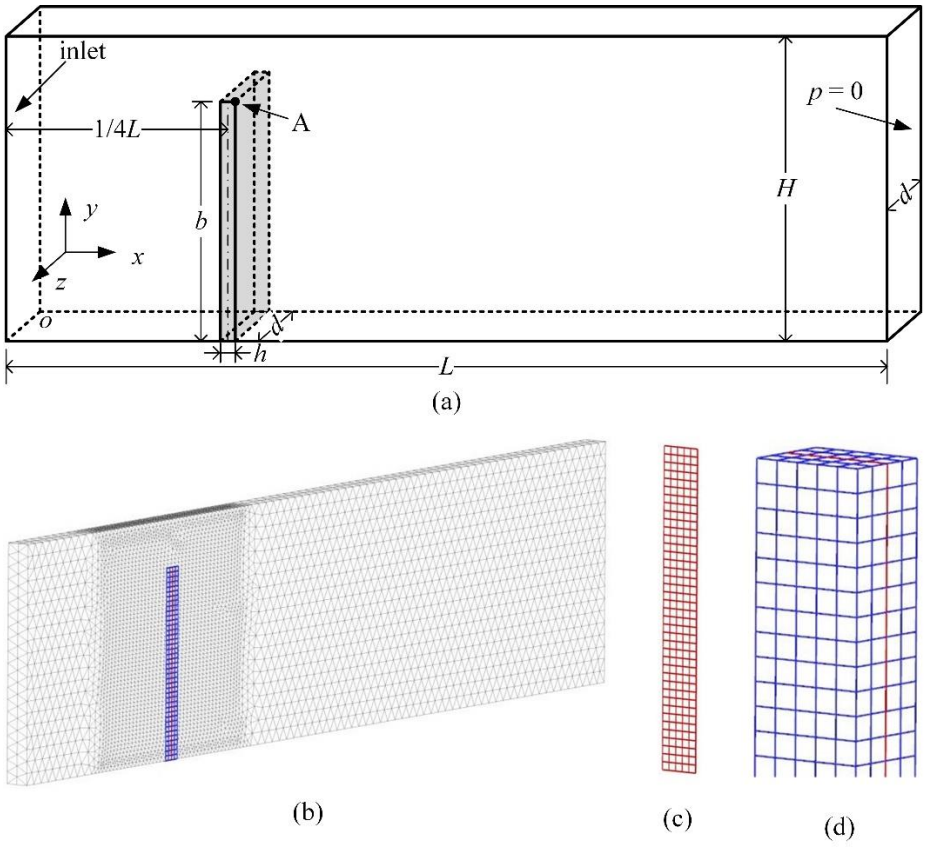

Figure 6.9: (a) Geometry of the flow over a vertical beam. (b) The meshes of the problem. (c) The meshes of the CB shell element. (d) The zoom-in plot of the Lagrangian fluid meshes and the shell element on the top.

Figure 6.9 (b) illustrates the meshing scheme of the problem with the finest mesh around the FSI interaction zone. The beam is modeled as a 3D plate discretized by CB shell elements shown in Figure 6.9 (c). Several layers of the Lagrangian fluid mesh wrap the shell in every time step, as shown in Figure 6.9 (d). In terms of the finest fluid mesh, three

sets of the meshes are employed as follows: MS(1), $\Delta h^{Ef} = \Delta h^{Lf} = \Delta h^{s} = h/2$; MS(2), $\Delta h^{Ef} = \Delta h^{Lf} = \Delta h^{s} = h/4$; MS(3), $\Delta h^{Ef} = \Delta h^{Lf} = \Delta h^{s} = h/8$.

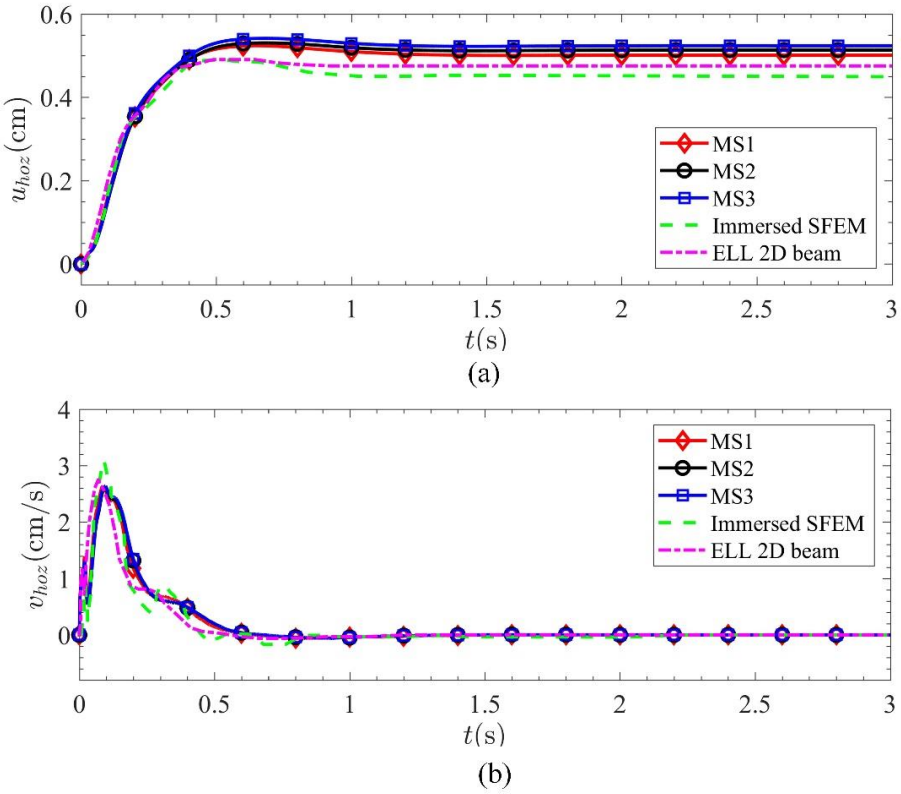

Figure 6.10: Time history of the (a) horizontal displacement and (b) horizontal velocity of the tip 'A'.

The histories of the velocity component v_x^s and the displacement u_x^s measured at the tip 'A' of the beam are shown in Figure 6.10. The results are compared with results from the references, and they match well. The contour plots of the horizontal velocity field and pressure at three different time steps are illustrated in Figure 6.11. The pressure oscillation is observed due to the singularity in the velocity gradient. Nevertheless, it does not affect the smoothness of the velocity field. The distribution of the velocity field matches

well with the reference at a steady state. The streamlines at steady state are shown in Figure 6.12, and a stable vortex is formed in the downwind side of the beam.

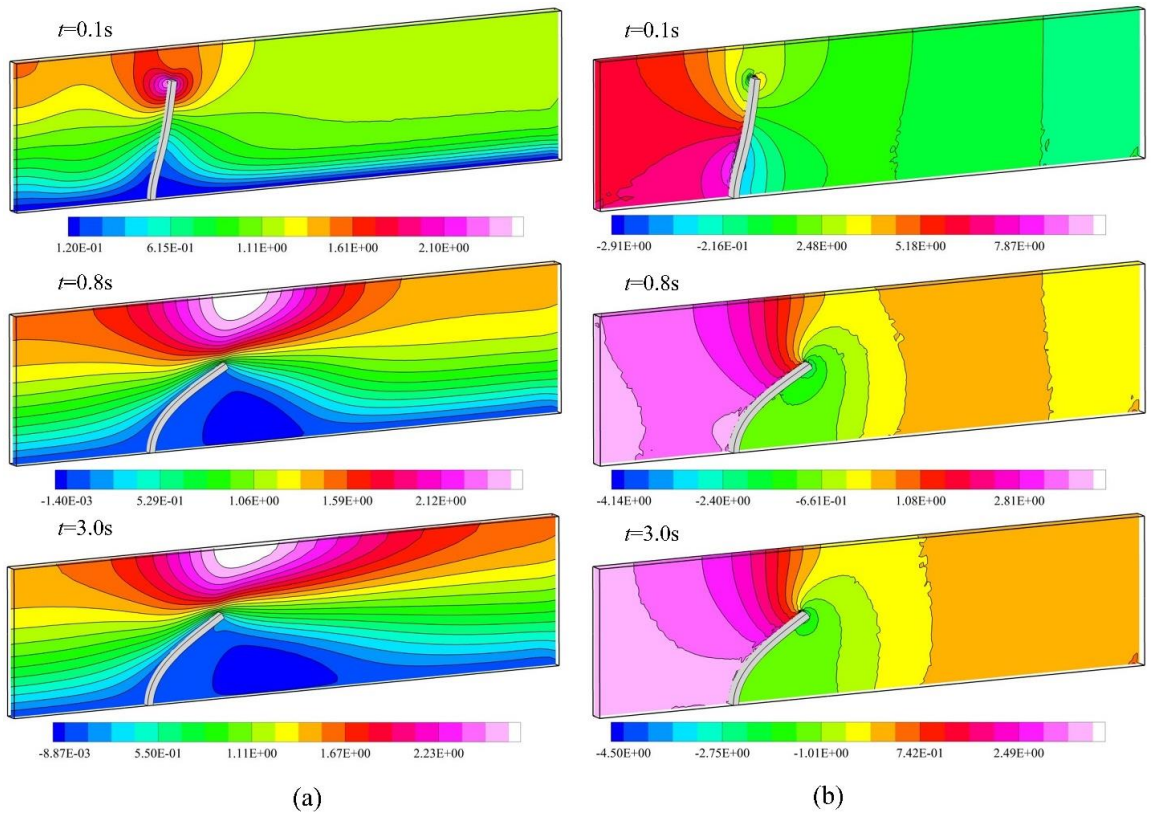

Figure 6.11: The snapshot of the contours: (a) horizontal velocity; (b) pressure. (Solved by MS3).

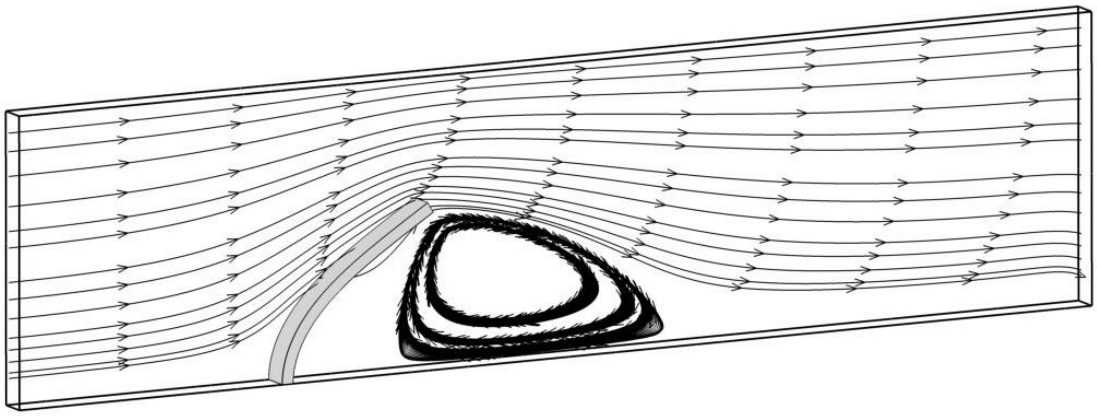

Figure 6.12: The streamline of at the steady-state.

6.2.2 Flow passing a beam attached to a cylinder

The benchmark problem of a flexible beam attached to a rigid cylinder in the downstream in 2D is solved by the 3D ELL method with CB shell modeling the flexible beam. The detailed geometry of the problem is illustrated in Figure 6.13. The 2D model is extended in 3D with a width of *W* in the third dimension. Two cases are computed,

Case (1). $\rho^s / \rho^f = 10$, Re = 100;

Case (2). $\rho^s / \rho^f = 1$, Re = 200.

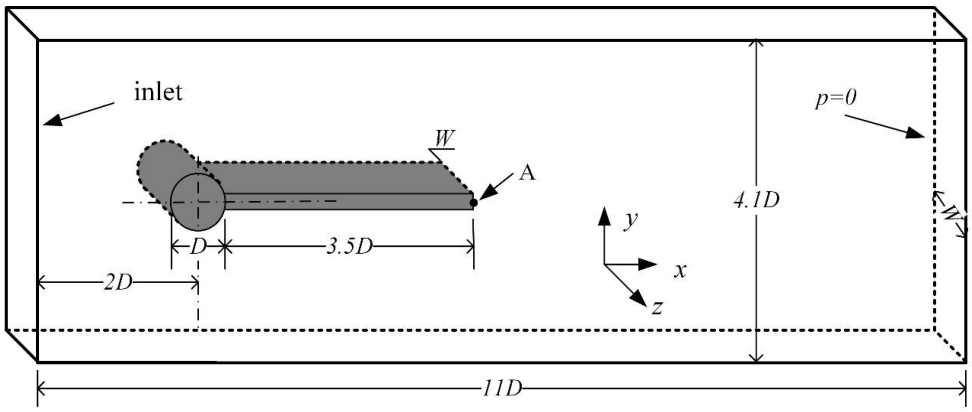

Figure 6.13: 3D geometry of the fluid flow passing a flexible beam attached to a rigid cylinder.

The other parameters of the beam are the same as in the 2D case. In Case (1), we discretized the shell, the Lagrangian fluid, and the finest Eulerian fluid mesh in the FSI zone with the size of $\Delta h^s = \Delta h^{Lf} = \Delta h^{Ef} = 0.25h$. In Case (2), we used double-sized elements, i.e. $\Delta h^s = \Delta h^{Lf} = \Delta h^{Ef} = 0.5h$, for the beam and wrapping Lagrangian fluid and the finest Eulerian fluid meshes. Both cases use four layers of the Lagrangian fluid meshes to wrapping the beam.

The time-varying displacement of the free end (point marked with 'A' in Figure 6.13) in *x*- and *y*-direction for case (1) is shown in Figure 6.14. The results from Turek & Hron [103] are also plotted in the figure as reference. The snapshots of the pressure contour, streamlines, deformation of the beam at four-time instances in one cycle of oscillation are shown in Figure 6.15 for Case (1) along with the distribution of the dominated Cauchy stress σ_{xx} in the beam. Table 6.1 records the displacement amplitude *Am* of free end in the *y*-direction along with Strouhal number *St* for both cases in comparison to the results from references. From the results in these figures and data in the table, the present ELL method shows an excellent agreement with results in the references.

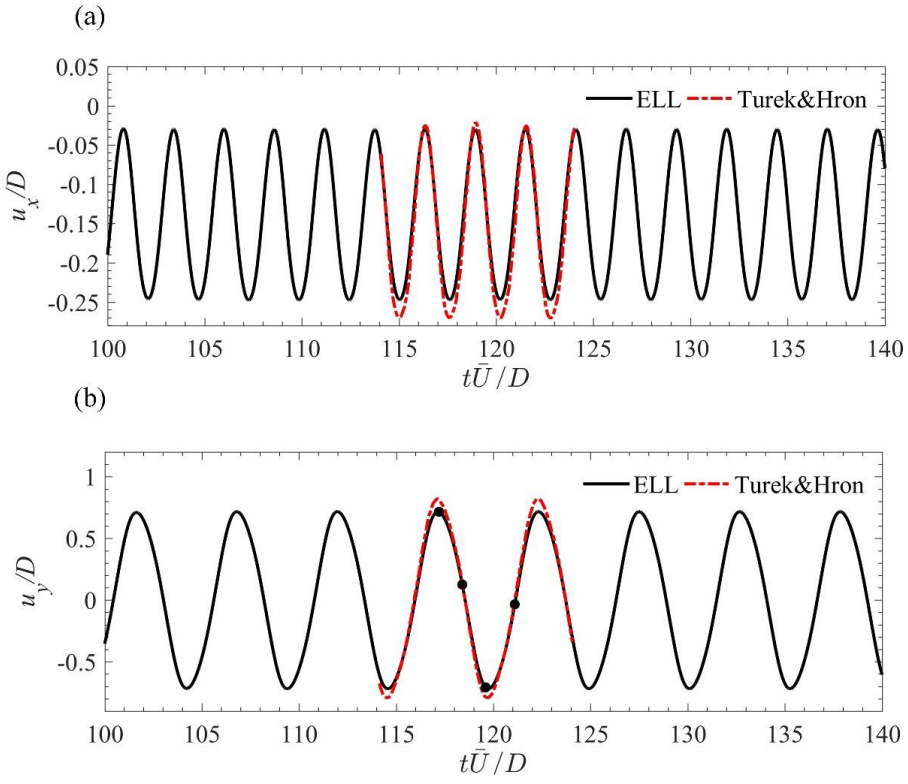

Figure 6.14: History of the displacement of the free end of the beam for case (1).

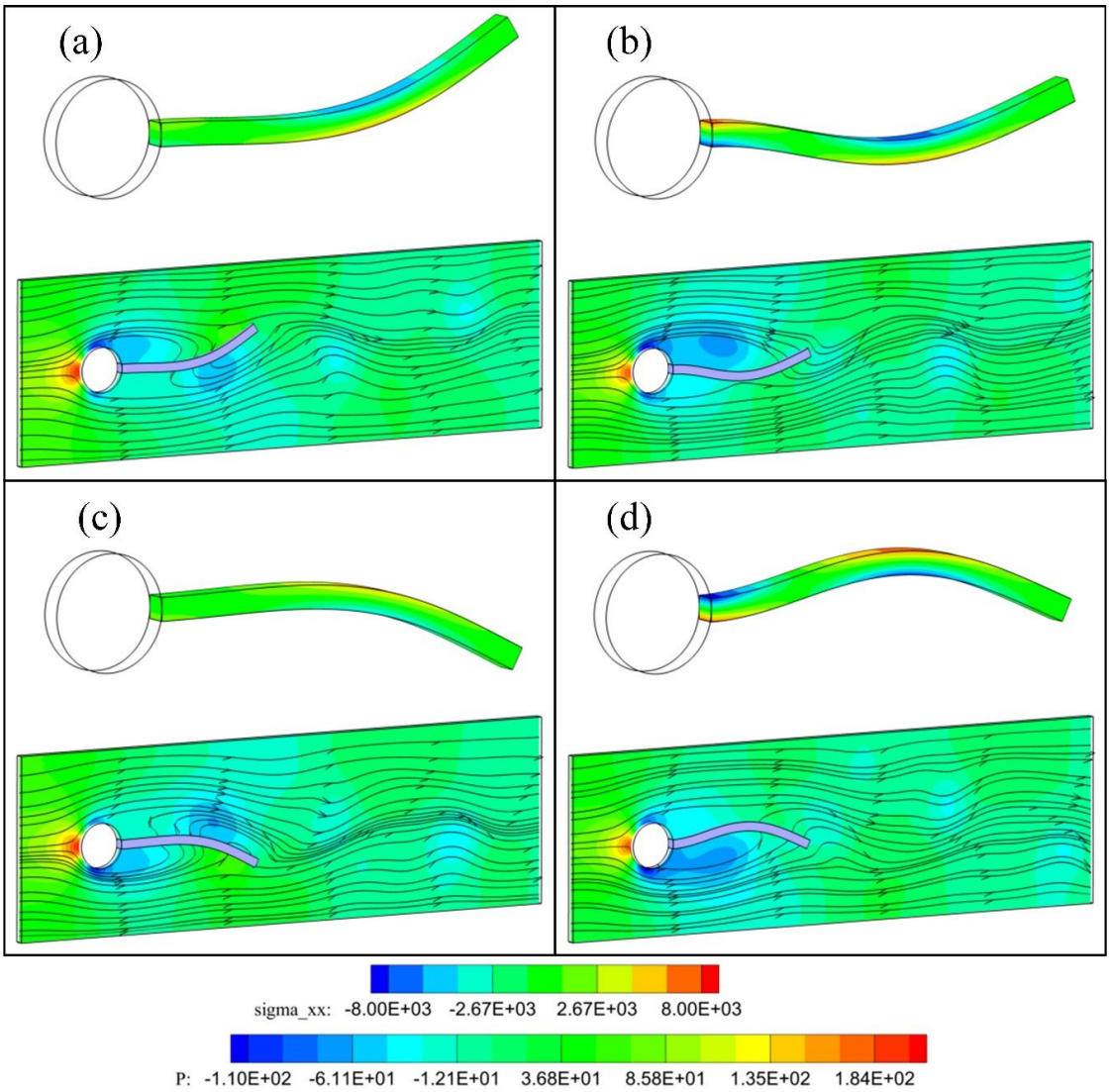

Figure 6.15: A snapshot of fluid pressure contours and streamlines along with the stress distribution (σ_{xx}) on the beam at four instances labeled in Figure 6.14.

Table 6.1. 3D flow over a flexible beam attached to a cylinder. The amplitude of the displacement in the *y*-direction of the free end along with the Strouhal number.

Sources	Case (1)		Case (2)	
	Am/D	*St*	*Am/D*	*St*

ELL 3D	0.72	0.19	0.41	0.27
ELL 2D	0.78	0.19	0.39	0.28
Turek & Hron [103]	0.83	0.19	0.36	0.26
Tian et al [104]	0.78	0.19	0.32	0.29
Bhardwaj & Mittal [105]	0.92	0.19	0.41	0.28

6.2.3 3D Flapping flag in the uniform flow

In this example, a 3D flapping flag in the uniform flow is investigated. This example has only been solved by a few references using IBM. Herein we solve this problem to validate our ELL method in solving 3D FSI problems with a very thin structure. The detailed schematic of the problem is illustrated in Figure 6.16; a square flag is placed in the middle of a tunnel pinned (not clamped) at the left edge with the other three edges free. The flag is placed in an initial orientation angle of $\theta_0 = 0.1\pi$ with respect to the constant incoming flow. The length of the flag is *L*. The thickness of the flag is $h = 0.01L$, i.e., the ratio of length and thickness is $L/h = 100$. The computational domain for the Eulerian fluid is $[-2L, 8L]\times[-4L, 4L]\times[-2L, 2L]$ with a uniform flow ($v_x^f = U$, $v_y^f = 0$ and $v_z^f = 0$).

A total number of 1,387,200 nodes and 8,220,008 T4 elements are used for the Eulerian fluid with the finest mesh $\Delta h^{Ef} = 0.02L$ near the beam and in the near field wake. A total number of 2,500 CB shell elements with the same size of the finest Eulerian fluid

mesh to model the flag. Four layers of the Lagrangian fluid meshes are included to employ the ELL implementation.

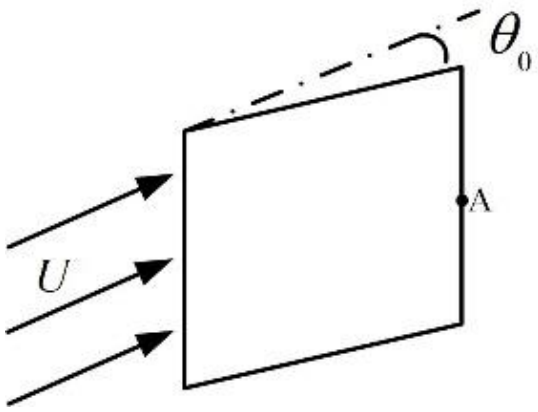

Figure 6.16: Schematic of the 3D flapping flag problem

To validate the proposed ELL algorithm with the adoption of the CB shell theory, we replicate the test presented by Huang et al. [118]. Reynolds number is defined as $\mathrm{Re} = \rho^f UL/\mu$. Without the consideration of the gravity, the other two dimensionless parameters that affect the system are the structure-to-fluid mass ratio, non-dimensional bending rigidity respectively as,

$$\lambda = \frac{\rho^s h}{\rho^f L}, \quad K_B = \frac{B}{\rho^f U^2 L^3} \tag{6.2}$$

where B is the flexural rigidity of the flag, they are set as $\mathrm{Re} = 200$, $\lambda = 1$ and $K_B = 0.0001$.

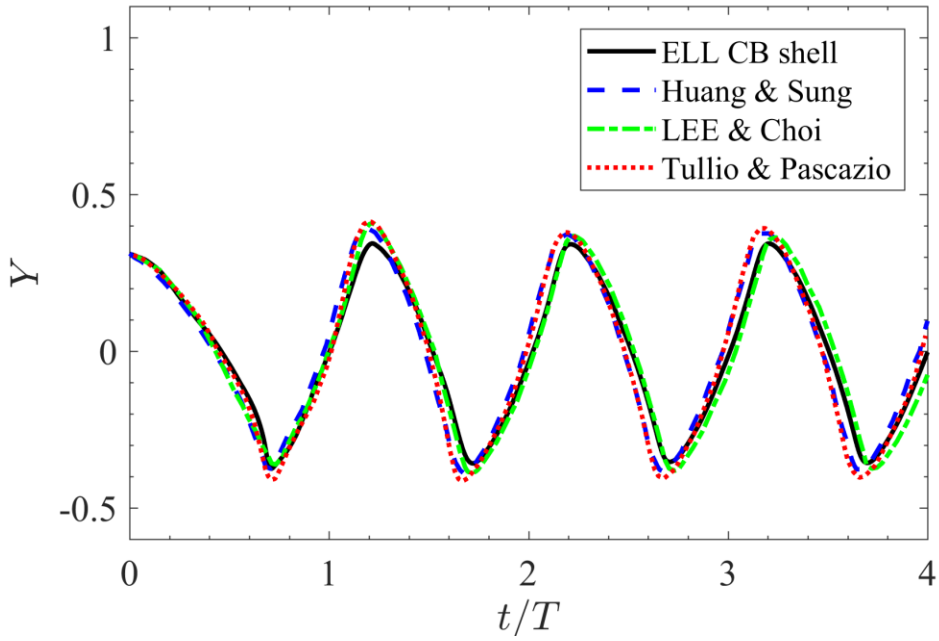

Figure 6.17: Time history of the transverse displacement of the flag in point A (marked in Figure 6.16).

Figure 6.17 shows the time history of the transverse location at the middle point of the trailing-edge (point labeled 'A' in Figure 6.16) along with the results from several results in the literature. The amplitude of the peak-to-peak oscillation *Am* and the Strouhal number defined as $St = fL/U$, where f is the frequency during stable-state oscillation measured in point A, are provided in Table 6.2 with some references in comparison. A good agreement is obtained. The time traces of the forces coefficients (drag and lift), normalized by $0.5\rho^f U^2 L^2$, are plotted in

Figure 6.18, compared with the results in [104, 112, 118, 119]. The agreement is satisfactory. Figure 6.19 plots a snapshot of the vertical structures for the flag identified by *Q*-criterion and showing the characteristic hairpin-like structure flow pattern.

Table 6.2. 3D flapping flag in the uniform flow. The transversal amplitude of the peak-to-peak displacement of the free end along with Strouhal number.

Sources	Amplitude *Am/L*	Strouhal number *St*
ELL	0.708	0.270
Huang & Sung [118]	0.780	0.260
Lee & Choi [112]	0.752	0.265
Tian et al [109] Flag 1	0.812	0.263
de Tullio & Pascazio [119]	0.795	0.265

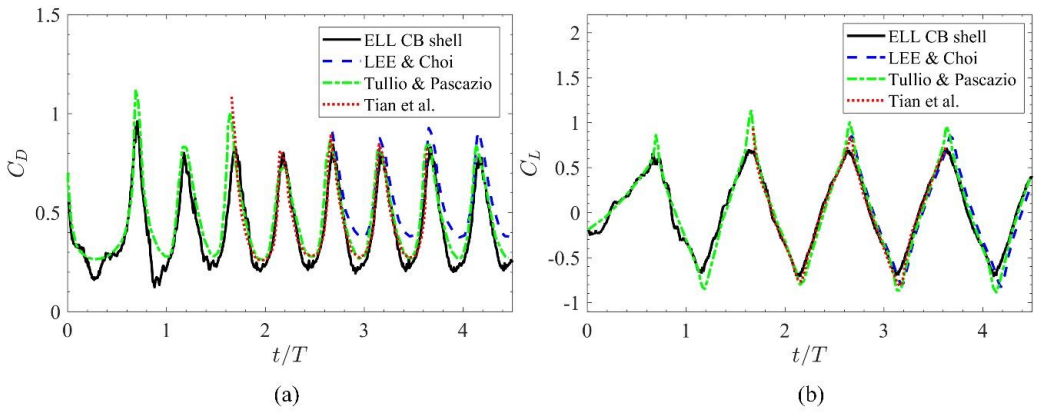

Figure 6.18: Time history of (a) the drag coefficient and (b) the lift coefficient.

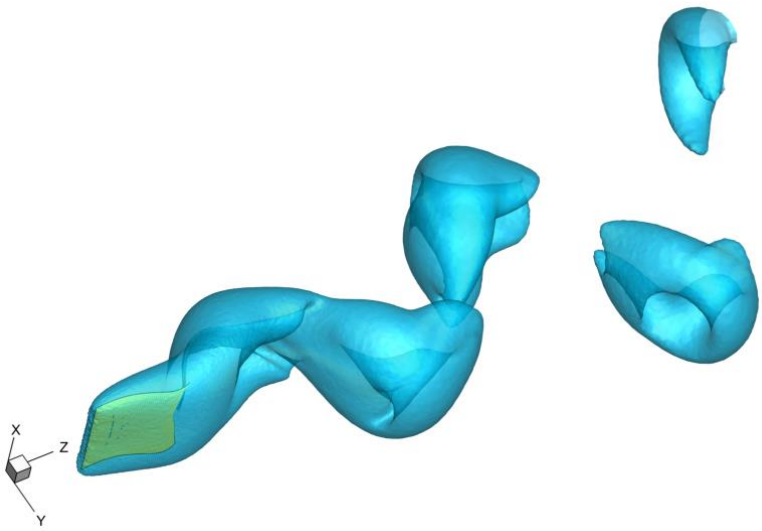

Figure 6.19: Snapshot of the vortical structures of the flapping flag in the uniform flow.

6.2.4 Symmetric flapping flexible wings of a butterfly

To explore the capacity of the ELL method with CB shell modeling the thin structure in solving real engineering 3D FSI problems, the symmetric flapping wing of a butterfly in section 6.1.3 is studied with the CB beam for the flexible wings.

The butterfly begins up-stoke in simulation at the time $t = 0$, with the Reynolds number $\mathrm{Re} = 200$. A soft material is used for the thin wings.

Four complete cycles of the flapping wings of the butterfly are computed. Figure 6.20 shows the flow structure of the symmetric flapping butterfly at three different stages in flapping cycles. These figures show the iso-surfaces of the vorticity along with the von Mises stress (VMS) distribution on the wings. The flapping angle of the wings is increasing to a peak with the velocity reaching zero, as shown in Figure 6.20 (a). At this stage, vortices of the tip and wake are mainly forming on the lower surfaces. Since the sum of the forces

is close to zero, the value of VMS is relatively small. The wings reach the center position of a cycle down-stoking with maximum velocity in Figure 6.20 (b). The vortices dominate on the upper surface of the wings, and some remnant vortexes having small magnitudes can also be observed at the edge of the lower wingtips. The wing shows an arched structure as the movement of the wing lags behind the movement of the leading rims. Figure 6.20 (c) shows the wings up-strokes accelerate from the lowest position. At the stage, the vortex begins to shift to the lower wing surfaces while a large portion of the vortex remains on the upper wing surfaces. The VMS on the wing at the last two stages have a larger magnitude due to the more significant external force from the fluid.

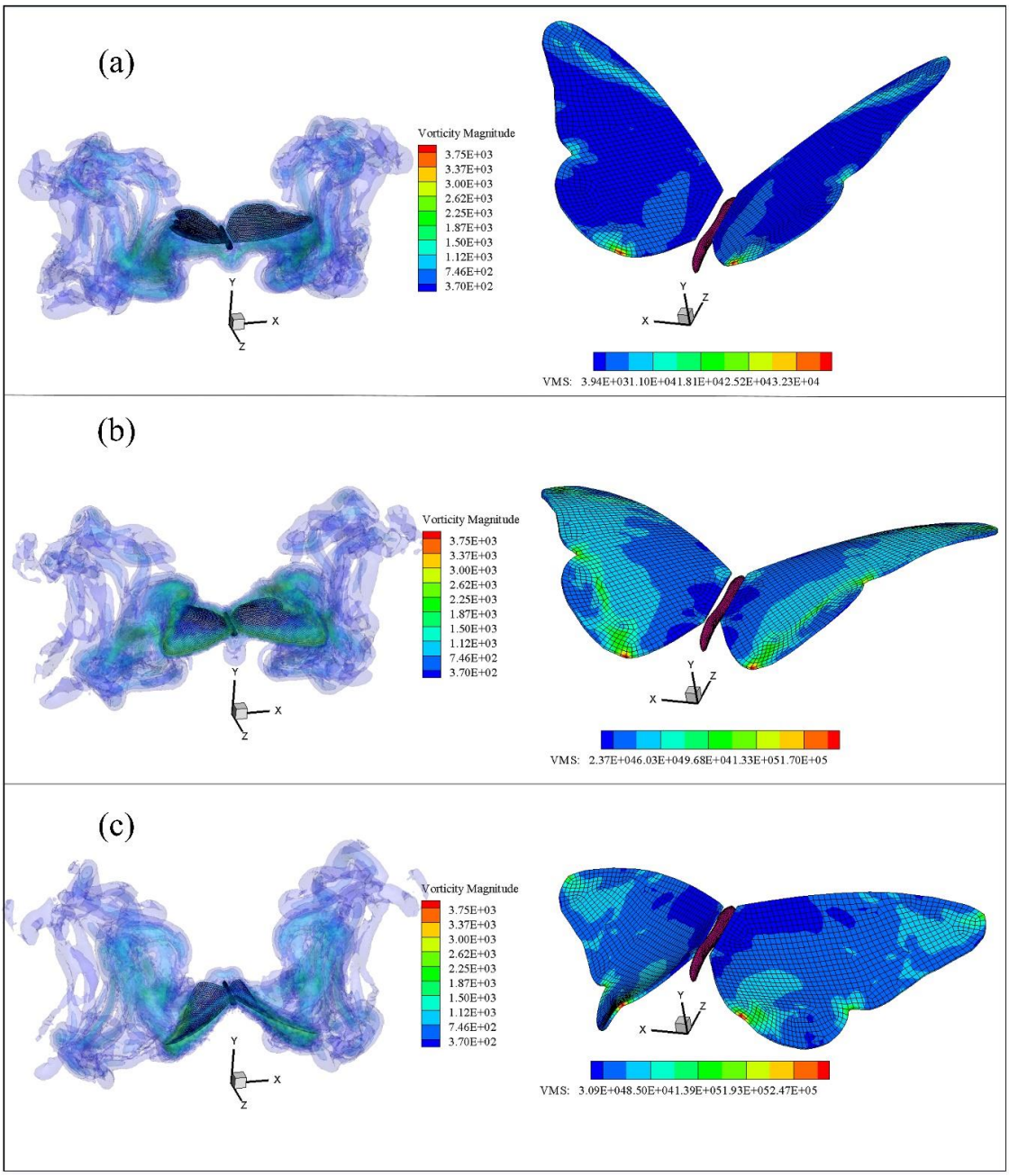

Figure 6.20: Vortical structures and von Mises stress distributions of the symmetric flapping wings of the butterfly in three different instants.

Figure 6.21 shows the time-varying force coefficients for a single wing during the first five cycles. C_z is nearly zero since the wings are flapping symmetrically about the pivot, which is parallel to the *z*-axis thus no significant resistant force. The vertical force

C_y decreases dramatically at the beginning of the simulation, which can be attributed to the up-stroking of the wing from a stationary state. C_y is symmetric during the simulation, which is a good match for the fact that the butterfly is undergoing a symmetric flapping motion. The horizontal force C_x also changes periodically synchronizing with the sinusoidal flapping wings.

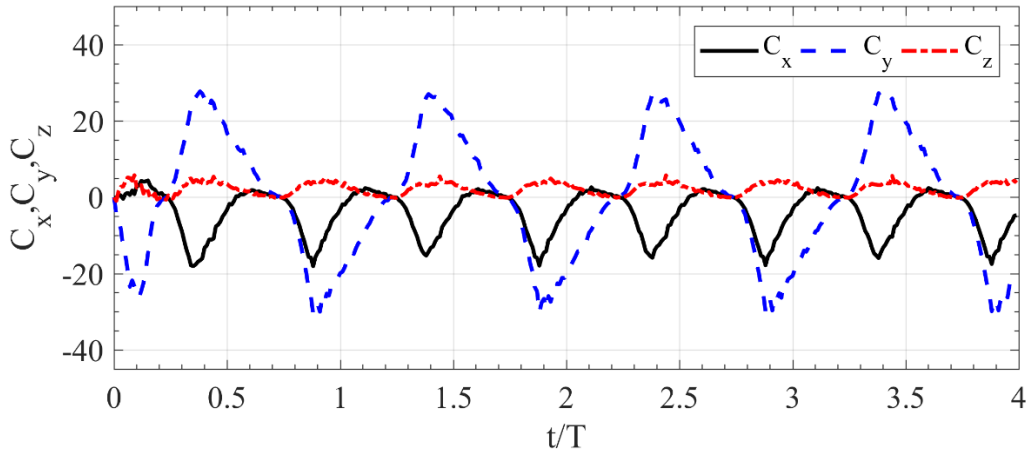

Figure 6.21: Time history of the force coefficient in *x*, *y*, and *z*-direction of a single wing in four complete cycles.

CHAPTER 7. CONCLUSION

This dissertation, a novel method, the Eulerian-Lagrangian-Lagrangian method, is presented for solving FSI problems with an improvement in the accuracy of the solution. The derivation of the ELL presents the mathematical and physical basis aiming at (1) developing a promising approach that unifies the two categories of the FSI algorithms, i.e., the conforming and non-conforming mesh methods, into one configuration; (2) explaining the physical meaning behind the usage of added wrapping fluid.

In ELL, a small portion of the fluid is used to enlarge the volume of the solid, such that they can be treated as one "composite solid" within the Lagrangian frame. The interface velocity is smoothly transferred from the solid to the fluid nodes with the help of the fictitious fluid, thus making the FSI interface being resolved more accurately in the ELL as compared to the existing IFEM approach. The superior accuracy of ELL is demonstrated by solving different FSI problems.

It also resolves the issue in IDM when dealing with a thin solid moving in the fluid. The CB beam element and CB shell element are successfully adopted to solve the FSI problems with thin structures, in which the realistic solid modeling is employed.

Some advantages of the proposed ELL method are concluded as follows.

- With the help of a wrapping fluid, the moving FSI interface is accurately imposed on the Lagrangian fluid meshes.

- It inherits the most significant advantage of the immersed type method, which has a fixed Eulerian fluid.

- With the adoption of FEM interpolation, the widely used discretized Dirac delta function in the IBM method is thus removed. Thus, it enables the use of non-uniform grids when the geometry or boundary of fluid is complex.

- Due to the flexibility in the inclusion of the wrapping fluid, the re-meshing process for the "composite solid" becomes independent of the geometry of the bulk Eulerian fluid domain.

- With the extension of the solid, ELL for a thin body moving in the fluid is available for incorporating reduced elements, thus primarily improve the efficiency of the computation.

The ELL provides an ideal framework to combine the conforming meshes methods and the non-conforming meshes method. It is believed that the new configuration may open the door to coding FSI algorithms with both high accuracy and efficiency.

REFERENCES

1 H. J. Bungartz, M. Schäfer, (Eds.), Fluid-structure interaction: modelling, simulation, optimisation (Vol. 53), Springer Science & Business Media, 2006.

2 M. P. Paidoussis, Fluid-structure interactions: slender structures and axial flow (Vol. 1), Academic Press, 1998.

3 T. Nakata, H. Liu, A fluid-structure interaction model of insect flight with flexible wings, J. Comput. Phys. 231 (2012) 1822–1847.

4 M. Hamamoto, Y. Ohta, K. Hara, T. Hisada, Application of fluid-structure interaction analysis to flapping flight of insects with deformable wings, Adv. Robot. 21 (2007) 1–21.

5 Y. Lian, W. Shyy, Three-Dimensional Fluid-Structure Interactions of a Membrane Wing for Micro Air Vehicle Applications, (2003).

6 R. Nathan, G.G. Katul, G. Bohrer, A. Kuparinen, M.B. Soons, S.E. Thompson, A. Trakhtenbrot, H.S. Horn, Mechanistic models of seed dispersal by wind, Theor. Ecol. 4 (2011) 113–132.

7 K. Suzuki, I. Okada, M. Yoshino, Effect of wing mass on the free flight of a butterfly-like model using immersed boundary-lattice Boltzmann simulations, J. Fluid Mech. 877 (2019) 614–647.

8 J. Janela, A. Moura, A. Sequeira, A 3D non-Newtonian fluid-structure interaction model for blood flow in arteries, in: J. Comput. Appl. Math., North-Holland, 2010: pp. 2783–2791.

9 M. Feistauer, P. Sváček, J. Horáček, Numerical Simulation of Fluid–Structure Interaction Problems with Applications to Flow in Vocal Folds, in: Birkhäuser, Basel, 2014: pp. 321–393.

10 R. van Loon, P.D. Anderson, F.N. van de Vosse, A fluid-structure interaction method with solid-rigid contact for heart valve dynamics, J. Comput. Phys. 217 (2006) 806–823.

11 J.H. Spühler, J. Jansson, N. Jansson, J. Hoffman, 3D Fluid-Structure Interaction Simulation of Aortic Valves Using a Unified Continuum ALE FEM Model, Front. Physiol. 9 (2018) 363.

12 R. J. Bomphrey, T. Nakata, N. Phillips, S. M. Walker, Smart wing rotation and trailing-edge vortices enable high frequency mosquito flight, Nature. 544 (2017) 92–95.

13 D. D. Chin, D. Lentink, Flapping wing aerodynamics: from insects to vertebrates, J. Exp. Biol. 219 (2016) 920-932.

14 G. Huber, Swimming in flatsea, Nature 408 (2000) 777-778.

15 W.X. Huang, S. Alben, Fluid-structure interactions with applications to biology, Acta Mech. Sin. Xuebao. 32 (2016) 977–979.

16 J.H. Ferziger, M. Peric, Computational Methods for Fluid Dynamics, Third Edition, 2012.

17 G.N. Hou, J. Wang, A. Layton, Numerical Methods for Fluid-Structure Interaction - A Review, Commun. Comput. Phys. 12 (2012) 337–377.

18 A.M. Bavo, G. Rocatello, F. Iannaccone, J. Degroote, J. Vierendeels, P. Segers, Fluid-Structure Interaction Simulation of Prosthetic Aortic Valves: Comparison between Immersed Boundary and Arbitrary Lagrangian-Eulerian Techniques for the Mesh Representation, PLoS One. 11, (2016).

19 T. Nomura, T, J. R. Hughes, An arbitrary Lagrangian-Eulerian finite element method for interaction of fluid and a rigid body, Comput. Methods Appl. Mech. Eng. 95 (1992) 115–138

20 J. Donea, S. Guiliani, J.P. Halleux, An arbitrary Lagrangian-Eulerian finite-element method for transient dynamic fluid structure interactions, Comput. Methods Appl. Mech. Eng. 33 (1982) 689–723.

21 W.K. Liu, H. Chang, J.S. Chen, T. Belytschko, Arbitrary Lagrangian-Eulerian Petrov-Galerkin finite elements for nonlinear continua. Comput Methods Appl Mech Eng 68 (1988) 259–310.

22 H.H. Hu, N.A. Patankar, M.Y. Zhu, Direct numerical simulations of fluid-solid systems using the arbitrary Lagrangian-Eulerian technique. J. Comput. Phys. 169 (2001) 427–462.

23 T.E. Tezduyar, S. Sathe, R. Keedy, K. Stein, Space-time finite element techniques for computation of fluid-structure interactions, Comput. Methods Appl. Mech. Engrg. 195 (2006) 2002-2027.

24 T.E. Tezduyar, S. Sathe, Modelling of fluid-structure interaction with the space-time finite elements: solution techniques, Int. J. Numer. Meth. Fluids, 54 (2007) 855-900.

25 K. Takizawa, T.E. Tezduyar, Multiscale space-time fluid-structure interaction techniques, Comput. Mech. 48 (2011) 247-267.

26 C.S. Peskin, The immersed boundary method, Acta. Numer. (2002) 479-517.

27 R. Mittal, G. Iaccarino, Immersed boundary methods. Ann. Rev. Fluid Mech. 37 (2005) 239–61.

28 L. T. Zhang, M. Gay, Immersed finite element method for fluid-structure interactions, J. Fluids Struct. 23 (2007) 839–857.

29 D.C. Sternel, M. Schäfer, M. Heck, S. Yigit, Efficiency and accuracy of fluid-structure interaction simulations using an implicit partitioned approach, Comput. Mech. 43 (2008) 103–113.

30 W.A. Wall, S. Genkinger, E. Ramm, A strong coupling partitioned approach for fluid-structure interaction with free surfaces, Comput. Fluids. 36 (2007) 169–183.

31 H.G. Matthies, J. Steindorf, Partitioned strong coupling algorithms for fluid-structure interaction, Comput. Struct. 81 (2003) 805–812.

32 M. Heil, A.L. Hazel, J. Boyle, Solvers for large-displacement fluid-structure interaction problems: Segregated versus monolithic approaches, Comput. Mech. 43 (2008) 91–101.

33 J. Degroote, K.J. Bathe, J. Vierendeels, Performance of a new partitioned procedure versus a monolithic procedure in fluid-structure interaction, Comput. Struct. 87 (2009) 793–801.

34 C. Michler, S.J. Hulshoff, E.H. van Brummelen, R. de Borst, A monolithic approach to fluid-structure interaction, Comput. Fluids. 33 (2004) 839–848.

35 B. Hübner, E. Walhorn, D. Dinkler, A monolithic approach to fluid-structure interaction using space-time finite elements, Comput. Methods Appl. Mech. Eng. 193 (2004) 2087–2104.

36 C.S. Peskin, Flow patterns around heart valves: a numerical method, J. Comput. Phys. 10 (1972) 252–271.

37 C.S. Peskin, Numerical analysis of blood flow in the heart, J. Comput. Phys. 25 (1977) 220-252.

38 D. Boffi, L. Gastaldi, L. Heltai, C.S. Peskin, On the hyper-elastic formulation of the immersed boundary method, Comput. Methods Appl. Mech. Eng. 197 (2008) 2210–2231.

39 B.E. Griffith, C.S. Peskin, On the order of accuracy of the immersed boundary method: Higher order convergence rates for sufficiently smooth problems, J. Comput. Phys. 208 (2005) 75–105.

40 M.C. Lai, C.S. Peskin, An immersed boundary method with formal second-order accuracy and reduced numerical viscosity, J. Comput. Phys. 160 (2000) 705–719.

41 C. Liao, Y. Chang, C. Lin, J.M. McDonough, Simulating flows with moving rigid boundary using immersed-boundary method, Comput. Fluids 39 (2010) 152-167.

42 H. Luo, H. Dai, P. Ferreira de Sousa, B. Yin, On the numerical oscillation of the direct-forcing immersed-boundary method for moving boundaries. Comput. Fluids 56 (2012) 61–76.

43 C. Liu, C. Hu, An efficient immersed boundary treatment for complex moving object. J. Comput. Phys. 274 (2014) 654-680.

44 A. Gronskis, G. Artana, A simple and efficient direct forcing immersed boundary method combined with a high order compact scheme for simulating flows with moving rigid boundaries. Comput. Fluids 124 (2016) 86–104.

45 R.J. LeVeque, Z. Li, Immersed Interface Methods for Stokes Flow with Elastic Boundaries or Surface Tension, SIAM J. Sci. Comput. 18 (1997) 709–735.

46 R. Mittal, H. Dong, M. Bozkurttas, F.M. Najjar, A. Vargas, A. von Loebbecke, A versatile sharp interface immersed boundary method for incompressible flows with complex boundaries, J. Comput. Phys. 227 (2008) 4825–4852.

47 R. Glowinski, T.-W. Pan, T.I. Hesla, D.D. Joseph, A distributed Lagrange multiplier/fictitious domain method for particulate flows, Int. J. Multiph. Flow. 25 (1999) 755–794.

48 R. Glowinski, T.W. Pan, T.I. Hesla, D.D. Joseph, J. Périaux, A Fictitious Domain Approach to the Direct Numerical Simulation of Incompressible Viscous Flow past Moving Rigid Bodies: Application to Particulate Flow, J. Comput. Phys. 169 (2001) 363–426.

49 R. Glowinski, T.W. Pan, T.I. Hesla, D.D. Joseph, J. Periaux, A distributed Lagrange multiplier/fictitious domain method for the simulation of flow around moving rigid bodies: Application to particulate flow, Comput. Methods Appl. Mech. Eng. 184 (2000) 241–267.

50 N.A. Patankar, P. Singh, D.D. Joseph, R. Glowinski, T.-W. Pan, A new formulation of the distributed Lagrange multiplier/fictitious domain method for particulate flows, Int. J. Multiph. Flow. 26 (2000) 1509–1524.

51 S. Turek, D. Wan, L.S. Rivkind, The Fictitious Boundary Method for the Implicit Treatment of Dirichlet Boundary Conditions with Applications to Incompressible Flow Simulations, in: Springer, Berlin, Heidelberg, 2003: pp. 37–68.

52 D. Wan, S. Turek, Direct numerical simulation of particulate flow via multigrid FEM techniques and the fictitious boundary method, Int. J. Numer. Methods Fluids. 51 (2006) 531–566.

53 D. Wan, S. Turek, Fictitious boundary and moving mesh methods for the numerical simulation of rigid particulate flows, J. Comput. Phys. 222 (2007) 28–56.

54 D. Wan, S. Turek, An efficient multigrid-FEM method for the simulation of solid–liquid two phase flows, J. Comput. Appl. Math. 203 (2007) 561–580.17.

55 L. Zhang, A. Gerstenberger, X. Wang, W.K. Liu, Immersed Finite element method, Comput. Methods Appl. Mech. Engrg. 193 (2004) 2051-2067.

56 X. Wang, L. T. Zhang, Modified immersed finite element method for fully-coupled fluid-structure interactions, Comput. Methods Appl. Mech. Engrg. 267 (2013) 150-169.

57 L. T. Zhang, Modeling of soft tissues interacting with fluid (blood or air) using the immersed finite element method, J. Biomed. Sci. Eng. 7 (2014) 130-145.

58 W.K. Liu, D.W. Kim, S. Tang, Mathematical foundations of the immersed finite element method, Comput. Mech. 39 (2007) 211–222.

59 W.K. Liu, Y. Liu, D. Farrell, L. Zhang, X.S. Wang, Y. Fukui, N. Patankar, Y. Zhang, C. Bajaj, J. Lee, J. Hong, X. Chen, H. Hsu, Immersed finite element method and its applications to biological systems, Comput. Methods Appl. Mech. Eng. 195 (2006) 1722–1749.

60 Z.Q. Zhang, J. Yao, G.R. Liu, An immersed smoothed finite element method for fluid structure interaction problems, Int. J. Comput. Methods. 8 (2011) 747–757.

61 Z. Zhang, G.R. Liu, B.C. Khoo, Immersed smoothed finite element method for two dimensional fluid-structure interaction problems, Int. J. Numer. Meth. Engng. 90 (2012) 1292-1320.

62 Z. Zhang, G.R. Liu, B.C. Khoo, A three dimensional immersed smoothed finite element method (3D IS-FEM) for fluid-structure interaction problems, Comput. Mech. 51 (2013) 129-150.

63 J. Yao, G.R. Liu, D. A. Narmoneva, R. B. Hinton, Z. Zhang, Immersed smoothed finite element method for fluid-structure interaction simulation of aortic valves, Comput. Mech. 50 (2012) 789–804.

64 X. Sheldon Wang, Immersed boundary/continuum methods, in: Comput. Model. Biomech., Springer Netherlands, 2010: pp. 3–48.

65 X. Sheldon Wang, An iterative matrix-free method in implicit immersed boundary/continuum methods, Comput. Struct. 85 (2007) 739–748.

66 X.S. Wang, From immersed boundary method to immersed continuum methods, in: Int. J. Multiscale Comput. Eng., Begel House Inc., 2006: pp. 127–145.

67 X. Wang, L. T. Zhang, Interpolation functions in the immersed boundary and finite element methods, Comput. Mech. 45 (2010) 321–334.

68 G.R. Liu, Meshfree Methods : moving beyond the finite element method, second edition., CRC PRESS, 2018.

69 G.R. Liu, S.S. Quek, The Finite Element Method: A Practical Course: Second Edition, Elsevier Ltd., 2013.

70 R.W. Clough, Original formulation of the finite element method, Finite Elem. Anal. Des. 7 (1990) 89–101.

71 M.J. Turner, R.W. Clough, H.C. Martin, L.J. Topp, Stiffness and Deflection Analysis of Complex Structures, J. Aeronaut. Sci. 23 (1956) 805–823.

72 C. Jiang, J.-Y. Yao, Z.-Q. Zhang, G.-J. Gao, G.R. Liu, A sharp-interface immersed smoothed finite element method for interactions between incompressible flows and large deformation solids, Comput. Methods Appl. Mech. Eng. 340 (2018) 24–53.

73 D. Han, G.R. Liu, S. Abdallah, An Eulerian-Lagrangian-Lagrangian method for 2D fluid-structure interaction problem with a thin flexible structure immersed in fluids, Comput. Struct. 228 (2020) 106179.

74 D. Han, G.R. Liu, S. Abdallah, An Eulerian-Lagrangian-Lagrangian method for solving fluid-structure interaction problems with bulk solids, J. Comput. Phys. 405 (2020) 109164.

75 D. Han, G.R. Liu, S. Abdallah, An Eulerian-Lagrangian-Lagrangian method for solving thin moving rigid body immersed in the fluid, Comput. Fluids. 179 (2019) 687–701.

76 R. Radovitzky, M. Ortiz, Lagrangian finite element analysis of Newtonian fluid flows, Int. J. Numer. Meth. Engng. 43 (1998) 607-619.

77 B. Ramaswamy, M. Kawahara, Lagrangian finite element analysis applied to viscous free surface fluid flow, Int. J. Numer. Methods Fluids. 7 (1987) 953–984.

78 A. J. Chorin, A numerical method for solving incompressible viscous flow problems, J. Comput. Phys. 135 (1997) 118-125.

79 T. J. R. Hughes, W.K. Liu, A. Brooks, Finite element analysis of incompressible viscous flows by the penalty function formulation. J. Comput. Phys. 30 (1979) 1–60.

80 T. M. Shih, C. H. Tan, B. C. Hwang, Equivalence of artificial compressibility method and penalty-function method, Numerical Heat Transfer, part b: Fundamentals, 15 (1989) 127-130.

81 P. Nithiarasu, C.B. Liu, An artificial compressibility based characteristic based split (CBS) scheme for steady and unsteady turbulent incompressible flows. Comput. Methods Appl. Mech. Eng. 195 (2006):2961–2982.

82 C. Jiang, Z. Zhang, X. Han, GR Liu, G. Gao, T. Lin. A quasi-implicit Characteristic-based penalty finite element method for incompressible laminar viscous flows. Int. J. Numer. Meth. Eng., 114 (2018) 147-171.

83 T. Belytschko, W.K. Liu, B. Moran, Nonlinear Finite Elements for Continua and Structures, Hoboken, NJ: John Wiley & Sons; 2013.

84 T.J.R. Hughes, W.K. Liu, Nonlinear finite element analysis of shells-part II. two-dimensional shells, Comput. Methods Appl. Mech. Eng. 27 (1981) 167–181.

85 J. L. Curiel Sosa, A. J. Gil, Analysis of a continuum-based beam element in the framework of explicit-FEM, Finite Elem. Anal. Des. 45 (2009) 583-591.

86 K.-J. Bathe, E. Ramm, E.L. Wilson, Finite element formulations for large deformation dynamic analysis, Int. J. Numer. Methods Eng. 9 (1975) 353–386.

87 S. Ahmad, B.M. Irons, O.C. Zienkiewicz, Analysis of thick and thin shell structures by curved finite elements, Int. J. Numer. Methods Eng. 2 (1970) 419–451.

88 K.-J. Bathe, E.N. Dvorkin, A four-node plate bending element based on Mindlin/Reissner plate theory and a mixed interpolation, Int. J. Numer. Methods Eng. 21 (1985) 367–383.

89 K.-J. Bathe, E.N. Dvorkin, A formulation of general shell elements—the use of mixed interpolation of tensorial components, Int. J. Numer. Methods Eng. 22 (1986) 697–722.

90 E.N. Dvorkin, Nonlinear analysis of shells using the MITC formulation, Arch. Comput. Methods Eng. 2 (1995) 1–50.

91 T.J.R. Hughes, W.K. Liu, Nonlinear finite element analysis of shells: Part I. three-dimensional shells, Comput. Methods Appl. Mech. Eng. 26 (1981) 331–362.

92 M. Schwarze, S. Reese, A reduced integration solid-shell finite element based on the EAS and the ANS concept-Geometrically linear problems, Int. J. Numer. Methods Eng. 80 (2009) 1322–1355.

93 O.C. Zienkiewicz, R. Codina, A general algorithm for compressible and incompressible flow-Part I. the split, characteristic-based scheme. Int. J. Numer. Methods Fluids. 20 (1995) 869–85.

94 O.C. Zienkiewicz, P. Nithiarasu, R. Codina, M. Vazquez, P. Ortiz, The characteristic-based-split procedure: an efficient and accurate algorithm for fluid problems, Int. J. Numer. Meth. Fluids, 31 (1999) 359-392.

95 A.R. Koblitz, S. Lovett, N. Nikiforakis, W.D. Henshaw, Direct numerical simulation of particulate flows with an overset grid method, J. Comput. Phys. 343 (2017) 414–431.

96 W.D. Henshaw, D.W. Schwendeman, Parallel computation of three-dimensional flows using overlapping grids with adaptive mesh refinement, J. Comput. Phys. 227 (2008) 7469–7502.

97 S.E. Sherer, J.N. Scott, High-order compact finite-difference methods on general overset grids, J. Comput. Phys. 210 (2005) 459–496.

98 W. M. Chan, Overset grid technology development at NASA Ames Research Center. Comput. Fluids, 38 (2009) 496–503.

99 D. Martins, D. Albuquerque, J. Pereira, Continuity constrained least-squares interpolation for SFO suppression in immersed boundary methods, J. Comput. Phys. 336(2017) 608-626.

100 J. D. Eldredge. Numerical simulation of the fluid dynamics of 2d rigid body motion with the vortex particle method, J. Comput. Phys. 221(2007) 626-648.

101 Z. J. Wang, Two dimensional mechanism for insect hovering, Phys. Rev. Lett. 85 (2000) 2216.

102 M. Schäfer, S. Turek, Benchmark computations of laminar flow around a cylinder, In: Hirschel EH, editor. Flow simulation with high-performance computer II. Notes in numerical fluid mechanics, 52 (1996) 547-566.

103 S. Turek, J. Hron, Proposal for numerical benchmarking of fluid-structure interaction between an elastic object and laminar incompressible flow, in: H.J. Bungartz, M. Schäfer (Eds.), Fluid-Structure Interaction: Modelling, Simulation, Optimisation, Springer-Verlag, Berlin, Heidelberg, Netherlands, 2006, pp. 371-385.

104 F.-B. Tian, H. Dai, H. Luo, J.F. Doyle, B. Rousseau, Fluid-structure interaction involving large deformations: 3D simulations and applications to biological systems, J. Comput. Phys. 258 (2014) 451–469.

105 R. Bhardwaj, R. Mittal, Benchmarking a coupled immersed-boundary-finite-element solver for large-scale flow-induced deformation, AIAA J. 50 (2012) 1638-1642.

106 W. –X. Huang, S. J. Shin, H. J. Sung, Simulation of flexible filaments in a uniform flow by the immersed boundary method, J. Comput. Phys. 226 (2007) 2206-2228.

107 B. S. Connell, D. K. Yue, Flapping dynamics of a flag in a uniform stream, J. Fluid Mech. 581 (2007) 33-67.

108 M. J. Shelley, J. Zhang, Flapping and bending bodies interaction with fluid flows, Annu. Rev. Fluid Mech. 43 (2011) 449-465.

109 F.-B. Tian, H. Luo, L. Zhu, X.-Y Lu, Interaction between a flexible filament and downstream rigid body, Phys. Rev. E 82 (2010) 026301.

110 M. J. Shelley, J. Zhang, Flapping and bending bodies interaction with fluid flows, Annu. Rev. Fluid Mech. 43 (2011) 449-465.

111 L. Zhu, C. S. Peskin, Simulation of a flapping flexible filament in a flowing soap film by the immersed boundary method, J. Comput. Phys. 179 (2002) 452-468.

112 I. Lee, H. Choi, A discrete-forcing immersed boundary method for the fluid-structure interaction of an elastic slender body, J. Comput. Phys. 280 (2015) 529–546.

113 P. Gurugubelli, R. Jaiman, Self-induced flapping dynamics of a flexible inverted foil in a uniform flow, J. Fluid Mech. 781 (2015) 657–694.

114 C. Wang, J.D. Eldredge, Strongly coupled dynamics of fluids and rigid-body systems with the immersed boundary projection method, J. Comput. Phys. 295 (2015) 87–113.

115 A. Goza, T. Colonius, A strongly-coupled immersed-boundary formulation for thin elastic structures, J. Comput. Phys. 336 (2017) 401–411.

116 J. Zhang, S. Childress, A. Libchaber, M. Shelley, Flexible filaments in a flowing soap film as a model for one-dimensional flags in a two-dimensional wind, Nature 408 (2000) 835-839.

117 K. Ota, K. Suzuki, T. Inamuro, Lift generation by a two-dimensional symmetric flapping wing: immersed boundary-lattice Boltzmann simulations, Fluid Dyn. Res. 44 (2012) 045504

118 W.-X. Huang, H.J. Sung, Three-dimensional simulation of a flapping flag in a uniform flow, J. Fluid Mech. 653 (2010) 301–336.

119 M.D. de Tullio, G. Pascazio, A moving-least-squares immersed boundary method for simulating the fluid–structure interaction of elastic bodies with arbitrary thickness, J. Comput. Phys. 325 (2016) 201–225.